2D spin-orbit-coupled frustrated magnets

Dissertation

zur Erlangung des akademischen Grades

Dr. rer. nat.

eingereicht an der
Mathematisch-Naturwissenschaftlich-Technischen Fakultät
der Universität Augsburg

von

Vera Patricia Bader

Augsburg, Mai 2023

Universität
Augsburg
University

Erstgutachter:	Prof. Dr. Alexander A. Tsirlin
Zweitgutachter:	Prof. Dr. Philipp Gegenwart

Tag der mündlichen Prüfung: 12.07.2023

Acknowledgment

At the end of my journey I want to thank all my travel companions. On the way I met friendly and helpful people who maybe did not realize or even forgot how important their support was - but not the traveler.

I would like to thank my supervisor Alexander A. Tsirlin. His valuable tips for the optimization of the syntheses proofed always to be right and for every question he had a suitable paper ready. He introduced me into the world of synchrotron and neutron measurements. I highly appreciated the opportunity to carry out measurements at the ESRF and ILL and to participate in the Oxford Summer School on Neutron Scattering and the Jana workshop.

I thank Philipp Gegenwart for taking the task of second examiner and for the opportunity to work at his Chair and to carry out the syntheses and experiments in perfectly equipped labs. The labs were managed under the special direction of Anton Jesche.

Many conclusions could not have been drawn and many issues could not have been taken to an end without the help of many collaborators. A special thanks goes to the local contact Clemens Ritter who helped me with the neutron measurements and the analysis of the data. Andy Fitch, Catherine Dejoie, and Ola Grendal helped with the execution of the synchrotron measurements. I thank Ivo Heinmaa and Raivo Stern for the NMR measurements, Noah Winterhalter-Stocker for the measurements in the dilution fridge, Hakuto Suzuki, Bernhard Keimer, and Hlynur Gretarsson for the IRIXS measurements, Jan Langmann for the single-crystal x-ray diffraction measurements, and Alexander A. Tsirlin and Aleksandr Zubtsovskii for the synchrotron measurements at ALBA.

A big thanks to Klaus Wiedenmann and Alexander Herrnberger who dropped everything behind when there was need in the lab and to Christine Schäfer and Birgitta Eisenschmid who made everything else go. Theodor Grünwald facilitated my start by showing me how to deal with the whims of the horizontal furnace and the diffractometer.

If the road gets rocky a wanderer needs refreshment. Some new ideas emerged over a cup of coffee with Theodor Grünwald, Klaus Wiedenmann, and Prachi Telang. I am indebted to Franziska Grußler, Franziska Breitner, Robert Gruhl, Sebastian Erdmann, and Ina Pietsch for the fruitful discussions after lunch, and to Sebastian Bachus, Andreas Schneider, Andreas Wörl, Tanita Ballé, Johanna Oefele, Manuel Fix, Alexander Engel, Georg Bothmann, Christina Baumeister, Sven Esser, Aleksandr Zubtsovskii, Elias Lettl, Bin Shen, and Maximilian Uhl who embarked on a similar journey. I enjoyed the joint participation in conferences and the entertaining events outside working hours.

Every journey needs a preparatory phase and the selfless people I met before are equally part of this dissertation as the written pages and the cover. I thank Hagen Klauk and Ute Zschieschang from the Organic Electronics Group in Stuttgart who equipped me for this journey. I was well prepared. I also had the privilege to meet Prof. Gallus Rehm † during my scholarships. I made use of his wordly wisdom he shared with me so many times.

And last but definitely not least, I thank may parents, my sister, and my friends who supported me and understood that I was sometimes short in time or took parts of my work into my free time. Thank you.

Contents

List of Abbreviations

ADP atomic displacement parameter

BVS bond valence sum

DFT density functional theory

IRIXS intermediate x-ray energy RIXS

JJ Josephson junction

MAS magic angle spinning

NMR nuclear magnetic resonance

nn nearest neighbor

nnn next nearest neighbor

NPD neutron powder diffraction

XRPD x-ray powder diffraction

QSL quantum spin liquid

RIXS resonant inelastic x-ray scattering

SOC spin-orbit coupling

SQUID superconducting quantum interference device

TLAF triangular lattice antiferromagnet

1. Introduction

Solid-state physics rests upon the close link and fruitful interplay between theory and experiment. One task of experimentalists is finding crystalline materials that realize theoretical models, for example models of interacting spins. To this end, insulating magnets are studied in this experimental work.

The dissertation presents the complete way from the synthesis over the structural characterization to the thermodynamic properties of two compounds based on Ru, Na_2RuO_3 and Na_3RuO_4, and of two compounds based on Co, $Na_2BaCo(PO_4)_2$ and $Na_2SrCo(PO_4)_2$.

Concerning the first leg there is no general rule how a compound can be synthesized and sometimes trial and error processes are not uncommon. Additionally, due to different conditions in the lab the direct transfer of recipes found in the literature is not always possible but reactants, temperature, atmosphere or time need to be modified. Powder samples of the Ru-based compounds and single crystals of the Co-based compounds could be successfully synthesized.

The analysis of crystal structures makes up the second large part of this work. The crystallographic structures are described by symmetry elements and that is how the description with symmetry concepts first entered the field of physics. A crystal is built up from identical blocks which fill up the space completely. This can be compared to honeycombs in a beehive. Experts in packing space most effectively are bees. The honeycombs are halved rhombic dodecahedra filling the space without gaps and requiring the least possible amount of beeswax. The only about 0.15% better ratio of surface to volume given by the truncated octahedra does not outweigh the larger complexity. The concept of truncated octahedra as room filling units with the slightly improved ratio was figured out by Lord Kelvin after whom the temperature unit kelvin was named [1]. We will come across this unit quite often since the measured properties herein are investigated in dependence of the temperature. Without specific requirements on the surface to volume ratio the three-dimensional space can be filled by various polyhedra. In a crystal the smallest block builds up the whole crystal by translation. The translational symmetry is a crystallographic restriction which reduces the number of possible polyhedra and allows only 1, 2, 3, 4, and 6-fold rotations.

In Na_2RuO_3, the first compound investigated, the Ru ions form a honeycomb lattice and the honeycomb planes are stacked on top of each other. In contrast to the honeycombs in beehives the honeycomb cells in Na_2RuO_3 lack 6-fold symmetry and also defects in form of stacking faults are present. In the other three compounds

triangles tile up the plane. In Na_3RuO_4 triangular features are found on two different length scales and a secondary triangular lattice is formed. $Na_2BaCo(PO_4)_2$ and $Na_2SrCo(PO_4)_2$ have a simple triangular lattice.

The triangle is the simplest motif for geometrical frustration. If spins on the corners of the triangle are coupled antiferromagnetically the three spins can not be simultaneously aligned antiparallel. Frustration is the key ingredient for the realization of a quantum spin-liquid (QSL) state. A QSL is characterized by the absence of long-range magnetic order and persistent spin dynamics down to 0 K with long-range entangled spins. Theoretically, a QSL state is predicted in triangular lattice antiferromagnets (TLAFs) for specific balances of certain exchange interactions [2, 3]. Since real materials are more complex and differ from any idealized model the existence of a QSL state in any material remains heavily debated in the literature. An experimental report proposed $Na_2BaCo(PO_4)_2$ as QSL candidate and this compound is one of the topics of this study [4].

Given the fact that only the non-magnetic buffer ions between the magnetic slabs are exchanged, it is rather surprising that the structure of $Na_2SrCo(PO_4)_2$ shows significant differences leading to a lower monoclinic symmetry compared to the trigonal $Na_2BaCo(PO_4)_2$ compound. By comparing $Na_2BaCo(PO_4)_2$ and $Na_2SrCo(PO_4)_2$ the effect of structural details on the magnetic properties are studied.

Frustration often leads to spin arrangements which can be seen as compromise to satisfy all the competing exchange interactions. Na_3RuO_4 for example shows long-range magnetic order and the magnetic structure is incommensurate because the exchange interactions acting between the sites of the secondary triangular lattice are frustrated.

Na_2RuO_3 does not show long-range magnetic order but this can not be traced back to frustration but to the effect of spin-orbit coupling (SOC). Despite Ru^{4+} having both spin and orbital momenta SOC leads to a zero total momentum.

The characterization of the properties makes up the third large part of this thesis. Measurements and analyses of the thermodynamic properties such as heat capacity and magnetization in dependence of the temperature complete the investigation of the four compounds studied.

This thesis is structured as follows. In Chap. 2 the necessary crystallography and magnetism basics are given. Chap. 3 presents the experimental methods. Synthesis procedures and measurement setups are described. The results and discussion for each compound are given in Chap. 4 and $Na_2BaCo(PO_4)_2$ and $Na_2SrCo(PO_4)_2$ are compared before the summary is given.

2. Magnetism in Condensed Matter

Even before diffraction experiments were performed on crystals the regular habit of a crystal made clear that symmetric blocks build up the crystal leading to the regularities on a macroscopic scale. Until the discovery of aperiodic crystals the crystal was defined as periodic arrangement of atoms. Today a crystal is defined as material exhibiting a sharp diffraction pattern. In this work x-ray diffraction was the first method of choice to characterize the crystal structure. An introduction to diffraction is given in Sec. 2.3. In Sec. 2.1 the categorization of crystal structures into space groups according to their symmetries is described. The classification is not only made for the sake of organization. The exact determination of the symmetry elements is essential because the structure of a crystal is connected to its physical properties. The symmetry of the physical property must follow the symmetry elements of the point group of the crystal. This is the so called Neumann's principle.

Magnetism in compounds arises if magnetic atoms are placed on lattice sites of the crystal. Atoms with partially filled electron shells carry a magnetic moment. Since in this work Co^{2+}, Ru^{4+}, and Ru^{5+} compounds are investigated, d-transition metal compounds are described in Sec. 2.4. In this context SOC in an atom, the electrical field effect due to the local environment in a crystal, and Hund's rules dictating the way the orbitals are filled are addressed. Symmetry arguments lead to Kramers' theorem.

Experimentally, the magnetic properties are captured by measuring the macroscopic magnetization M as response to an external magnetic field H. The magnetic susceptibility χ connects $\vec{M}$ and $\vec{H}$ in the form $\chi = d\vec{M}/d\vec{H}$. In general, χ is a tensor. For a paramagnet an external magnetic field causes the magnetic moments to align parallel to the field and the magnetization is proportional to the external magnetic field. Hence, the susceptibility reduces to a scalar and $\chi = M/H$. This last definition of the susceptibility is often used, also throughout this thesis, even if M and H are not proportional. The description of the paramagnetic susceptibility is given by the Van Vleck formalism from which the Brillouin function and Curie's law can be derived (see Sec. 2.5). In paramagnets the magnetization is lost when the applied magnetic field is removed because the single magnetic moments are independent and do not interact.

Magnetic ions in a crystal can communicate via exchange interactions (see Sec. 2.6). Symmetry considerations will show that bonds with inversion symmetry forbid certain magnetic exchange interactions. At low temperatures, the exchange interactions will typically stabilize a long-range order of magnetic moments (see Sec. 2.5), the so-called magnetic structure. Neutron diffraction as tool to determine magnetic structures is presented in Sec. 2.3.

Competing exchange interactions can suppress magnetic ordering. The concept of frustration relevant for Na_3RuO_4, $Na_2BaCo(PO_4)_2$, and $Na_2SrCo(PO_4)_2$ and an introduction to QSLs in triangular lattice compounds relevant for $Na_2BaCo(PO_4)_2$ and $Na_2SrCo(PO_4)_2$ are given under the heading "Exotic Magnetism". In this Sec. 2.7 also the excitonic magnetism is discussed in the context of Na_2RuO_3.

2.1. Crystal Structures

The concept

translation lattice + motif = crystal structure

can be used to describe a crystal geometrically. To create the translation lattice in three dimensions three basis vectors or translation vectors are chosen. All the points obtained through linear combination of these basis vectors with integer coefficients form the translation lattice. The parallelepiped spanned by the three basis vectors is called the unit cell. Mostly the basis vectors are chosen such that the unit cell has the smallest possible volume. Larger unit cells which clearly display the symmetry elements of the crystal may be chosen. Translation of the unit cell must lead to a compact three-dimensional arrangement which fills the space completely. This condition restricts the number of translation lattices and the so-called Bravais translation lattices can be organized in seven lattice systems: cubic, hexagonal, rhombohedral, tetragonal, orthorhombic, monoclinic, and triclinic. The 14 Bravais lattices are shown in Fig. 2.1. Each category contains one primitive lattice. The other seven lattices are obtained if additional constraints are imposed on the lattice parameters of the primitive cells. For example, if the angles in the rhombohedral case are all restricted to 60 ° the resulting lattice can also be described with the

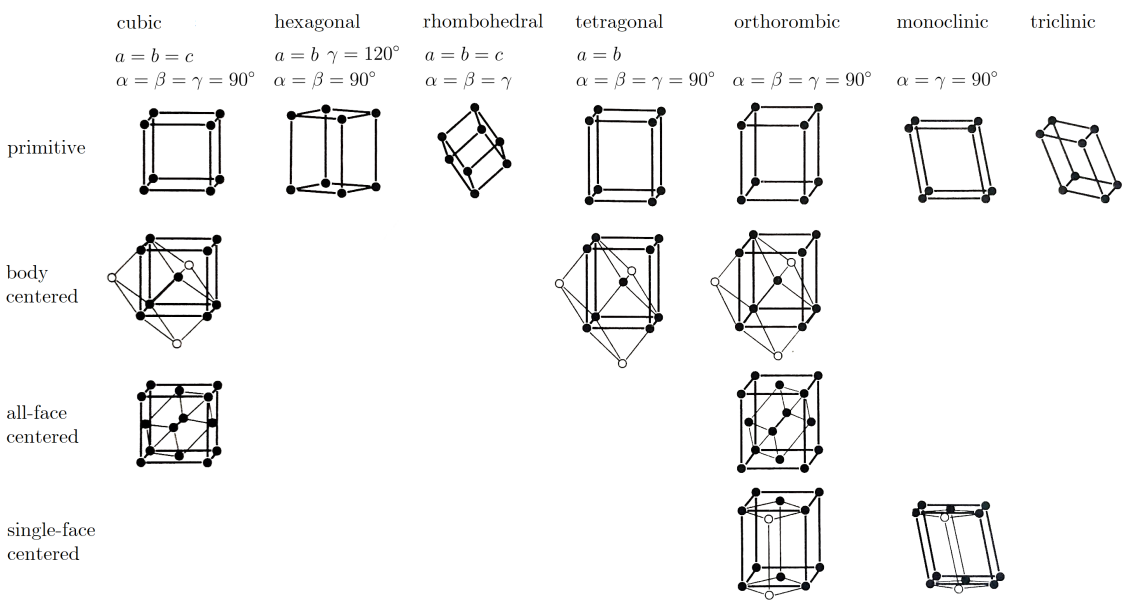

Figure 2.1.: The 14 Bravais translation lattices can be organized into seven categories. Seven primitive lattices exist. The additional seven lattices are obtained if further constraints are imposed on the lattice parameters of the primitive cells. The corresponding primitive cells are indicated by the open circles. The figure was adapted from Ref. [5].

face centered cubic lattice. Similar, if the angles are restricted to 109.5 ° the body centered cubic lattice results [5]. The primitive lattice points are indicated as well in Fig. 2.1.

The translation lattice is not yet the crystal structure. To completely describe a crystal a motif has to be added. The positions of the atoms forming the motif are given by dimensionless fractional coordinates. The basis vectors of the translation lattice defined earlier span also the coordinate system.

On the way to the description of the symmetry of the crystal structure the concept of point groups is necessary. A point group is a mathematical group of symmetry elements pertaining to a body which pass at least through one common point and leave this point fixed. The translational symmetry conditions in crystals allow only a limited number of symmetry elements because the image points of lattice points must fall again onto lattice points. Possible symmetry operators are the inversion i and $n = 1, 2, 3, 4, 6$-fold rotation axes. Combination of the rotation and inversion lead to the rotoinversion. With the restricted number of symmetry elements 32 crystallographic point groups can be formed in three dimensional space.

If now the 32 crystallographic point groups are brought together with the 14 translational Bravais lattices all possible combinations of symmetry elements are obtained. The combination of the translational and point group symmetries lead to two further symmetry elements, the glide plane and the screw axis. In total 230 space groups can be created. Since the motif is unconstrained an infinite number of crystal structures exists. Every possible crystal structure can be described in one of these space groups. The space groups can be assigned to one of the seven crystal systems:

(1) Cubic	$a = b = c,\ \alpha = \beta = \gamma = 90°$
(2) Tetragonal	$a = b,\ \alpha = \beta = \gamma = 90°$
(3) Orthorhombic	$\alpha = \beta = \gamma = 90°$
(4) Hexagonal	$a = b,\ \gamma = 120°$
(5) Trigonal	$a = b = c,\ \alpha = \beta = \gamma$
	or $a = b,\ \gamma = 120°$
(6) Monoclinic	$\alpha = \gamma = 90°$
(7) Triclinic	No restrictions

It is important to note that the translation lattice can have a higher symmetry than the crystal structure. The symmetry of the atomic arrangement causes the constraints on the lattice parameters and determines the assignment to one of the crystal systems.

2.2. Magnetic Structures

Instead of describing a magnetic structure as periodic arrangement of magnetic unit cells in analogy to the nuclear structure the description of the magnetic structure is based on the nuclear structure. Magnetic order creates an additional periodicity on top of the periodicity of the crystal lattice and additional reflections appear in the diffraction pattern. The satellite reflections are found at positions

$$\vec{G} = \vec{G}_0 \pm \vec{k} \tag{2.1}$$

with the reciprocal vector $\vec{G}_0$ of the lattice and the vector of the magnetic structure $\vec{k}$ called the propagation vector. The moment distribution $\vec{m}_\mathrm{j}$ for atom j is

$$\vec{m}_\mathrm{j} = \sum_{\vec{k}} \vec{\Psi}_\mathrm{j}^{(\vec{k})} e^{-2\pi i \vec{k}\vec{t}} \tag{2.2}$$

with the lattice translation vector $\vec{t}$ and $\vec{\Psi}_\mathrm{j}$ is the linear combination of the basis vectors $\vec{\psi}_\nu$ with the mixing coefficients C_ν: $\vec{\Psi}_\mathrm{j}^{(\vec{k})} = \sum_\nu C_\nu \vec{\psi}_\nu^{(\vec{k})}$ [6].

The magnetic structure is commensurate if the components of $\vec{k}$ are integer fractions and incommensurate if the components are irrational, i.e. the periodicity of the magnetic structure is not a simple fraction or integer multiple of the periodicity of the crystal lattice.

From equation 2.2 it is apparent that a magnetic structure is fully described if the $\vec{k}$ vectors, the basis vectors, and the mixing coefficients are known. The general procedure to determine the magnetic structure from experimental diffraction data is briefly introduced in the following.

The list of symmetry groups can be extended by introducing the operation $1'$. This leads to the Shubnikov groups which can be used to describe magnetic structures if the magnetic moments are treated as axial vectors and $1'$ is the time reversal symmetry operator flipping the spin. The description with the concept of magnetic space groups is suited for commensurate structures. In the case of Na_3RuO_4 presented in here we will encounter an incommensurate structure and the more general representation analysis is needed.

The crystallographic groups are groups in a mathematical sense. For finding possible descriptions for the magnetic structure the subgroup called the Little Group which contains all the symmetry elements which leave $\vec{k}$ invariant is considered [6]. The symmetry elements forming the group can be represented as matrices which have the same multiplication table. If there is a unitary transformation which transforms all matrices in the group into the same block-diagonal form the representation is called reducible. The reducible representation Γ_mag can be written as linear combination (coefficients $m_\mathrm{i} \in \mathbb{N}$) of irreducible representations Γ_i ($i = 1, 2, ..., n$), shortly irreps, which can not be reduced further [7]

$$\Gamma_\mathrm{mag} = m_1\Gamma_1 \oplus m_2\Gamma_2 \oplus ... \oplus m_\mathrm{n}\Gamma_\mathrm{n}. \tag{2.3}$$

The number of irreps n of a group equals the number of classes in that group. To deduce the irreps it is not necessary to find that unitary transformation. Unitary transformations leave the trace of the matrices invariant and hence irrespective of the basis vectors the traces of the matrices characterize the representation [8]. With the concept of character tables built up by the traces the irreps can be found. The procedure is explained elsewhere [7].

Landau theory states that for a second order phase transition the symmetry of the low-temperature phase is described by one of the irreps. In case of a first order transition more than one irrep or more than one propagation vector are involved [6, 9].

In the next step basis vectors $\vec{\Psi}_\nu$ for each irrep are introduced (see Ref. [6]) and the mixing coefficients C_ν are used as refinable parameters. To find the optimal set of basis vectors describing the magnetic structure (see equation 2.2) all the possible irreps need to be tested [6].

2.3. Diffraction

The periodic arrangement of the atoms in a crystal entails periodic quantities $n(\vec{r})$ such as the nuclear, electron, and spin densities. Diffraction captures that periodicity and the diffraction pattern is a Fourier transform of the direct lattice. The periodicity calls for a Fourier transform and $n(\vec{r})$ can be expressed as

$$n(\vec{r}) = \sum_{\vec{G}} n_{\vec{G}} \exp(i\vec{G}\vec{r}) \tag{2.4}$$

with the Fourier coefficients $n_{\vec{G}}$. Translational invariance demands that the vectors $\vec{G}$ are reciprocal lattice vectors of the structure.

The scattering amplitude F is

$$\begin{aligned} F &= \int dV n(\vec{r}) \exp\left[i\left(\vec{k}_{\text{inital}} - \vec{k}_{\text{final}}\right)\vec{r}\right] \\ &= \int dV n(\vec{r}) \exp\left(-i\Delta\vec{k}\vec{r}\right) \end{aligned} \tag{2.5}$$

with the scattering vector $\Delta\vec{k} = \vec{k}_{\text{final}} - \vec{k}_{\text{inital}}$. Combining equations 2.4 and 2.5 lead to

$$F = \sum_{\vec{G}} \int dV n_{\vec{G}} \exp\left[i\left(\vec{G} - \Delta\vec{k}\right)\vec{r}\right]. \tag{2.6}$$

The scattering amplitude is only non vanishing if the scattering vector is a reciprocal lattice vector

$$\Delta\vec{k} = \vec{G}. \tag{2.7}$$

When the diffraction condition holds, the scattering amplitude from equation 2.5 can be written as

$$F = N \int_{cell} dV n(\vec{r}) \exp\left(-i\vec{G}\vec{r}\right) \tag{2.8}$$

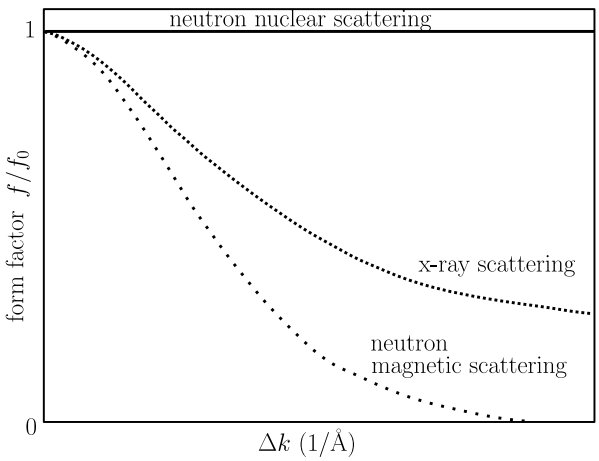

Figure 2.2.: In the case of neutron nuclear scattering the form factor is constant with Δk. The form factor in the case of magnetic scattering decreases even faster with Δk than the atomic form factor in the case of x-ray scattering.

The integral sums over all N cells of the crystal. The integral is the so-called structure factor S. The scattered intensity is proportional to $|S|^2$. For further considerations it is helpful to consider the contribution of each individual atom at position $\vec{r}_j$ in a cell to the total electron density. It follows for the structure factor

$$\begin{aligned} S &= \sum_j \int dV n_j\left(\vec{r}-\vec{r}_j\right) \exp\left(-i\vec{G}\vec{r}\right) \\ &= \sum_j \exp\left(-i\vec{G}\vec{r}_j\right) \int dV n_j\left(\vec{r}-\vec{r}_j\right) \exp\left(-i\vec{G}\left(\vec{r}-\vec{r}_j\right)\right) \\ &= \sum_j f_j \exp\left(-i\vec{G}\vec{r}_j\right). \end{aligned} \tag{2.9}$$

In the last step the integral is summarized in the form factor f_j which is an atomic property

$$f_j = \int dV n_j\left(\vec{\rho}\right) \exp\left(-i\vec{G}\vec{\rho}\right) \tag{2.10}$$

with $\vec{\rho} \equiv \vec{r} - \vec{r}_j$. Ref. [10] was used as reference.

The form factors for the cases of x-ray, neutron nuclear and magnetic scattering in dependence of Δk are shown in Fig. 2.2. In the case of neutron nuclear scattering $n_j(\vec{\rho})$ is the nuclear density and the neutral neutrons are scattered by the point like nuclei. The Fourier transform of a delta function is a constant. In the case of x-ray scattering $n_j(\vec{\rho})$ is the electron density and the photons are scattered by the electron clouds and the form factor decreases with increasing Δk. In the case of magnetic scattering $n_j(\vec{\rho})$ is the magnetization density. The magnetic form factor decreases even faster since only the electrons in the outer shell responsible for the magnetic moment are involved [11]. The magnetization density can by approximated by the spin density $n_{j,\mathrm{spin}}(\vec{\rho})$ times the local magnetic moment μ. In the case of magnetic

scattering it is important to note that the neutrons probe only the component of the magnetization perpendicular to the scattering vector. With the form factor

$$f_j = \mu_\perp \int dV n_{j,\text{spin}}(\vec{\rho}) \exp\left(-i\vec{G}\vec{\rho}\right) = \mu_\perp f_{\text{magn}} \tag{2.11}$$

the structure factor becomes

$$S = f_{\text{magn}} \sum_n \mu_\perp(\vec{\rho}_n) \exp\left(-i\vec{G}\vec{r}_n\right). \tag{2.12}$$

Here one atom per unit cell was assumed and the sum runs over the lattice sites n because the periodicity of the nuclear and magnetic structure may be different. The structure factor is the Fourier transform of the spin density distribution. The magnetic reflections mirror the periodicity of the magnetic structure and their intensity is proportional to $\mu_\perp^2$. The phase shifts between the magnetic components enter the structure factor in the form $e^{i\phi}$ and the phase information gets lost in the experiment which records the scattered intensity. For example, it is not possible with unpolarized neutrons to distinguish between collinear spin-density waves and helical structures with the phase shift as only distinctive feature. Refs. [11] and [9] were used as references.

2.4. Transition Metal Compounds

2.4.1. Crystal Field

In a crystal the magnetic atom is surrounded by neighboring atoms creating an electrical field which affects the energy levels of the atom. In the following only the octahedral environment is considered. In many transition metal compounds the magnetic atom is surrounded by oxygen and the electrons in the p orbitals create the electrical field. The five d orbitals of the central atom can be separated into two categories, the d_{xy}, d_{xz}, d_{yz} orbitals pointing between the x, y, and z axes and the d_{z^2}, $d_{x^2-y^2}$ orbitals pointing along the axes. As illustrated in Fig. 2.3 for one d orbital of each category the orbital overlap with the p orbitals oriented along the axes is different. The d orbitals pointing along the axes have a higher electrostatic energy and are raised in energy whereas the other three orbitals are lowered in energy. The threefold t_{2g} orbitals are separated by the crystal field splitting Δ_{cryst} from the twofold e_g orbitals.

2.4.2. Spin-orbit Coupling

The spin and orbital angular momenta couple through the spin-orbit interaction which is briefly introduced in the following. In the electron frame of reference the nucleus is orbiting the electron. The nuclear current creates a magnetic field with

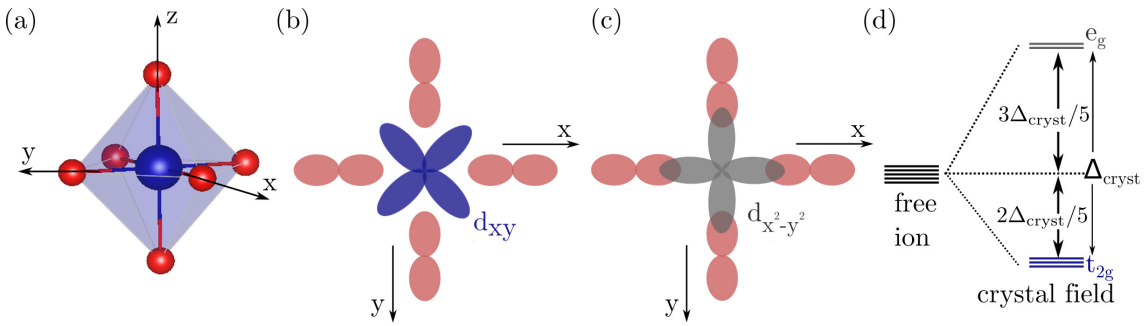

Figure 2.3.: Crystal field effect in an (a) octahedral environment. (b) The lobes of the d_{xy} orbital point between the p orbitals of the ligands. (c) The lobes of the $d_{x^2-y^2}$ orbital point in the direction of the ligands. (d) The three d orbitals with a lower overlap with the p orbitals are lowered in energy whereas the two orbitals with higher overlap are raised in energy. The figure was adapted from Ref. [12].

flux density $\vec{B}$ that interacts with the magnetic moment $\vec{\mu}$ which arises due to the spin of the electron and the Hamiltonian is given as

$$\hat{\mathcal{H}}_{\mathrm{SO}} = -\frac{1}{2}\vec{\mu}\cdot\vec{B}. \tag{2.13}$$

The factor 1/2 is a relativistic correction. The magnetic field arises from the electrical field $\vec{E}$ which is given through the spherical potential energy $V(r)$. With the velocity $\vec{v}_{\mathrm{n}}$ of the nucleus and the speed of light c

$$\vec{B} = \frac{\vec{E}\times\vec{v}_{\mathrm{n}}}{c^2} = -\frac{\mathrm{d}V(r)}{\mathrm{d}r}\frac{1}{rc^2}\vec{r}\times\vec{v}_{\mathrm{n}}. \tag{2.14}$$

With equation 2.14, the magnetic moment $\vec{\mu} = (ge\hbar/2m_{\mathrm{e}})\vec{S}$ with the electron-spin Landé factor $g \approx 2$, and $\hbar\vec{L} = m_{\mathrm{e}}\vec{r}\times\vec{v}$ equation 2.13 can be transformed into

$$\hat{\mathcal{H}}_{\mathrm{SO}} = \frac{e\hbar^2}{2m_{\mathrm{e}}^2c^2r}\frac{\mathrm{d}V(r)}{\mathrm{d}r}\vec{S}\cdot\vec{L} = \lambda\vec{S}\cdot\vec{L} \tag{2.15}$$

with the SOC constant λ. The total angular momentum $\vec{J} = \vec{L}+\vec{S}$ is conserved. The new quantum number J takes values from $|L-S|$ to $L+S$. With $\vec{J}^2 = \vec{L}^2+\vec{S}^2+2\vec{L}\cdot\vec{S}$ the expectation value of the energy is

$$\langle\lambda\vec{L}\cdot\vec{S}\rangle = \frac{\lambda}{2}[J(J+1) - L(L+1) - S(S+1)]. \tag{2.16}$$

The splitting energy of adjacent J levels is given by the Landé interval rule

$$\begin{aligned} E(J) - E(J-1) &= \frac{\lambda}{2}[J(J+1) - L(L+1) - S(S+1)] \\ &- \frac{\lambda}{2}[(J-1)J - L(L+1) - S(S+1)] \\ &= \lambda J. \end{aligned} \tag{2.17}$$

The SOC model considered here is the $L-S$ coupling or Russell-Saunders coupling and adequate for the magnetic ions of the compounds presented herein. Since the spin-orbit interaction energy increases with increasing atomic number the $j-j$ coupling scheme is used for heavier elements. Ref. [13] was used as reference.

2.4.3. Hund's Rules

The three Hund's rules are an empirical guide to determine the angular momentum quantum numbers of the ground state configuration [14].

1. Maximize S
   The Pauli exclusion principle forbids two electrons with parallel spins to occupy the same orbital and hence, by maximizing S the electron-electron Coulomb repulsion is reduced.

2. Maximize L
   Also this rule ensures the reduction of Coulomb repulsion between the electrons. Electrons orbiting in the same direction can avoid each other better.

3. $J = |L - S|$ for less than half filling
   $J = L + S$ for more than half filling
   This rule considers the minimization of the spin-orbit energy.

The higher the energy minimization the stronger the rule. The rules are listed in decreasing order of their importance and it is found that the last rule is sometimes violated for transition metal ions because effects such as crystal field splitting become significant. Also maximizing S is not favorable if the crystal field splitting exceeds the pairing energy. In the next section some examples relevant for this work will be given.

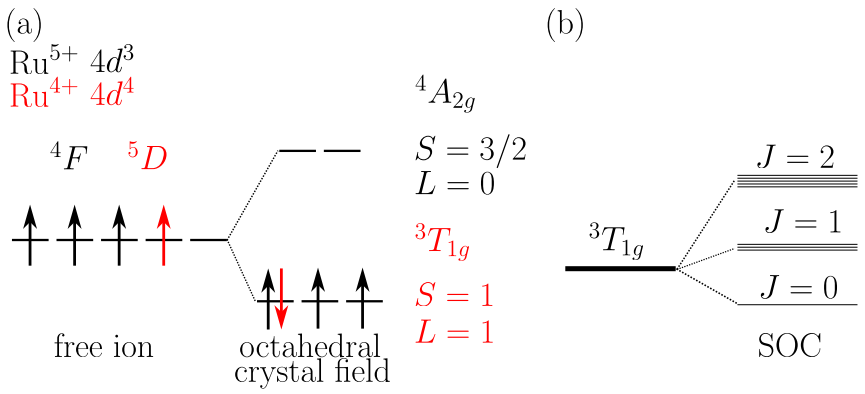

Figure 2.4.: Energy level schemes relevant for the Ru-based compounds. (a) Na_3RuO_4 has the electron configuration $4d^3$ and in the presence of an octahedral crystal field the lowest lying t_{2g} levels are single occupied and $S = 3/2$ and $L = 0$. The red arrow was added to illustrate the case of $4d^4$ as for Na_2RuO_3. If the crystal field energy exceeds the pairing energy a low-spin complex forms and $S = 1$ and $L = 1$. (b) The SOC leads to the splitting of the $^3T_{1g}$ levels and a $J = 0$ ground state emerges. (b) was adapted from Ref. [15].

2.4.4. Examples: Ru^{4+}, Ru^{5+}, and Co^{2+}

The crystal field effect, the SOC, and the Hund's rules will be illustrated for the electronic configurations relevant in this work. First, the compound with the lowest number of electrons in the d shell will be looked at. In Na_3RuO_4 Ru has an oxidation state of +5 and three electrons occupy the $4d$ orbitals. The octahedral crystal field splits the five degenerate d orbitals. The three t_{2g} levels are occupied each by one electron and the e_{2g} levels at a higher energy are empty [see Fig. 2.4(a)]. Therefore, $S = 3/2$ and for a half-filled sub-shell $L = 0$. Indeed, the spin-only character was shown experimentally (see Subsec. 4.2.2).

Adding a further electron to the d shell leads to a more complex situation. The additional electron is indicated in red in Fig. 2.4(a). The configuration $4d^4$ is realized in Na_2RuO_3 with Ru having the oxidation state +4. One of the lower lying t_{2g} orbitals is now double occupied and $S = 1$ and $L = 1$. In contrast to the case of Na_3RuO_4 an orbital momentum exists to which the spin momentum can couple. The SOC leads to the splitting of the $^3T_{1g}$ level into $J = 0$, $J = 1$, and $J = 2$ levels. The $J = 0$ ground state is still debated in the literature (see Introduction of Sec. 4.1) but the experimental results in this work suggest a $J = 0$ ground state.

In the latter case a low-spin configuration is realized because the spin-pairing energy is lower than the crystal field splitting. The size of the crystal field splitting depends on the central cation and the ligands. Often the trend can be observed that the field splitting is larger for cations with higher oxidation number.

Whereas for Ru^{4+} the formation of a low-spin complex is observed, a high-spin configuration forms in the case of $Na_2BaCo(PO_4)_2$ and $Na_2SrCo(PO_4)_2$ with Co^{2+} as central metal ion. The case of a $3d^7$ configuration is depicted in Fig. 2.5(a).

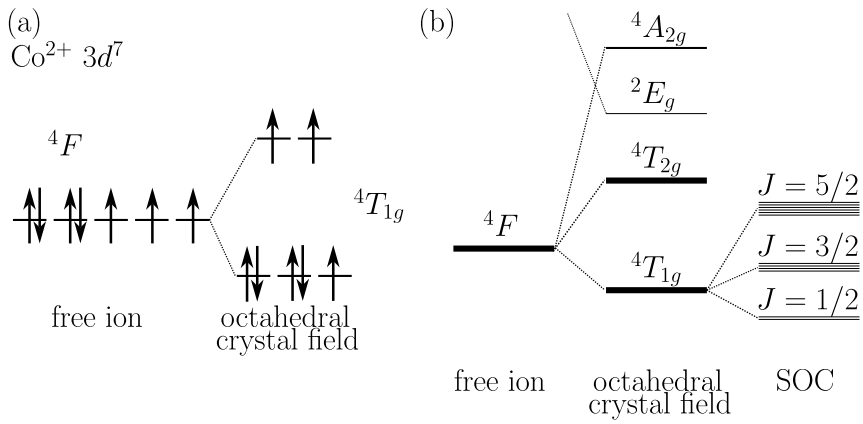

Figure 2.5.: Energy level schemes relevant for the Co-based compounds. (a) Co^{2+} compounds have the configuration $3d^7$. Following Hund's rules leads to t_{2g}^5 and e_g^2. (b) The $^4T_{1g}$ dodecet splits in the presence of SOC into levels with effective spin 1/2, 3/2, and 5/2. (b) was adapted from Ref. [16].

In this case, the Hund's rules can be strictly followed. The octahedral crystal field splitting leads to the configuration $t_{2g}^5\ e_g^2$. The $^4T_{1g}$ level with spin multiplicity 4 and triple degeneracy with respect to orbital state splits in the presence of SOC into a doublet with effective spin 1/2 and into the four-fold degenerate level with effective spin 3/2 and the six-fold degenerate level with effective spin 5/2 at higher energies [see Fig. 2.5(b)]. At low temperatures $Na_2BaCo(PO_4)_2$ and $Na_2SrCo(PO_4)_2$ can be treated as spin-1/2 systems (see Subsecs. 4.3.3 and 4.4.4).

2.4.5. Kramers' Theorem

Theorem. *If a system has half-integer total spin and its Hamiltonian is time-reversal invariant there is for every eigenstate at least one more eigenstate which has the same energy. In other words, in a time-reversal symmetric system all energy levels of an odd-number electron system are at least two-fold degenerate.*

This applies to the examples $4d^3$ and $3d^7$ with an odd number of electrons described previously (see Figs. 2.4 and 2.5). The proof is given in what follows.

If the Hamiltonian commutes with the time-reversal symmetry operator $[\hat{\mathcal{T}}, \hat{\mathcal{H}}] = 0$ and $|\psi\rangle$ is an eigenstate with energy E then $\hat{\mathcal{T}}\,|\psi\rangle$ is also an eigenstate with the same energy:

$$\begin{aligned} \hat{\mathcal{H}}\,|\psi\rangle &= E\,|\psi\rangle \\ \hat{\mathcal{H}}\hat{\mathcal{T}}\,|\psi\rangle &= E\hat{\mathcal{T}}\,|\psi\rangle\,. \end{aligned} \tag{2.18}$$

Now it remains to be shown that $|\psi\rangle$ and $\hat{\mathcal{T}}\,|\psi\rangle$ are two different states.

Usually the operator $\hat{\mathcal{T}}$ which reverses the direction of the spin is given as

$$\hat{\mathcal{T}} = e^{-i\pi\hat{S}^y}\hat{\mathcal{K}} = e^{-i\pi\sigma^y/2}\hat{\mathcal{K}} = \hat{\mathcal{U}}\hat{\mathcal{K}} \tag{2.19}$$

with the spin operator in y direction $\hat{S}^{\mathrm{y}}$, which can be represented for spin-1/2 particles by the Pauli matrix σ^{y}, and the complex conjugation $\hat{\mathcal{K}}$. The first factor is unitary and $\hat{\mathcal{K}}$ is antiunitary. Unitary operators preserve a scalar product and hence

$$\langle \hat{\mathcal{T}}\psi|\hat{\mathcal{T}}\phi\rangle = \langle \hat{\mathcal{U}}^{\dagger}\hat{\mathcal{K}}\psi|\hat{\mathcal{U}}\hat{\mathcal{K}}\phi\rangle = \langle \psi^{*}|\phi^{*}\rangle = \langle \phi|\psi\rangle\,. \tag{2.20}$$

This relation will become useful later on.

For an n electron system $\hat{\mathcal{T}}$ has the form

$$\hat{\mathcal{T}} = e^{-i\pi\sigma_1^{\mathrm{y}}/2}\cdot e^{-i\pi\sigma_2^{\mathrm{y}}/2}\cdot \ldots \cdot e^{-i\pi\sigma_n^{\mathrm{y}}/2}\hat{\mathcal{K}} \tag{2.21}$$

and

$$\hat{\mathcal{T}}^2 = (-1)^n. \tag{2.22}$$

This minus sign also appears if a spin state of a spin-1/2 particle is rotated by 2π.

Finally, the scalar product of the eigenstates $|\psi\rangle$ and $\hat{\mathcal{T}}\,|\psi\rangle$ can be written as

$$\langle \hat{\mathcal{T}}\psi|\psi\rangle = \langle \hat{\mathcal{T}}\psi|\hat{\mathcal{T}}^2\psi\rangle = (-1)^n\,\langle \hat{\mathcal{T}}\psi|\psi\rangle\,. \tag{2.23}$$

The first equals sign uses equation 2.20 and the second equals sign uses equation 2.22. For an odd number n

$$\langle \hat{\mathcal{T}}\psi|\psi\rangle = 0 \quad \square \tag{2.24}$$

and the two states with the same energy are orthogonal. Ref. [17] was used as reference.

2.5. Basic Forms of Magnetism

2.5.1. Van Vleck Formalism of Paramagnetism

The macroscopic magnetization arises from the magnetic moments of the atoms. The moment depends on the occupation of the levels n with energy E_n. In analogy to the macroscopic magnetization $M = -dE/dH$ the microscopic magnetization for an atom is given by $m_n = -dE_n/dH$. The magnetization is the sum of m_n weighed by the Boltzmann factor

$$M = \frac{N_{\mathrm{A}}\sum_n \left(-dE_n/dH\right) e^{-E_n/(k_{\mathrm{B}}T)}}{\sum_n e^{-E_n/(k_{\mathrm{B}}T)}}. \tag{2.25}$$

The energy values can be expressed as a power series

$$E_n = E_n^{(0)} + E_n^{(1)}H + E_n^{(2)}H^2 + \ldots \tag{2.26}$$

with the first and second order Zeeman coefficients $E_n^{(1)}$ and $E_n^{(2)}$. $E_n^{(0)}$ is the energy of level n when no magnetic field is applied. For small $H/\left(k_{\mathrm{B}}T\right)$

$$e^{-E_n/(k_{\mathrm{B}}T)} = e^{-E_n^{(0)}/(k_{\mathrm{B}}T)}\left(1 - E_n^{(1)}H/\left(k_{\mathrm{B}}T\right)\right) \tag{2.27}$$

and equation 2.25 becomes

$$M = \frac{N_\mathrm{A} \sum_n \left(-E_n^{(1)} - 2E_n^{(2)} H\right) \left(1 - E_n^{(1)} H/(k_\mathrm{B}T)\right) e^{-E_n^{(0)}/(k_\mathrm{B}T)}}{\sum_n \left(1 - E_n^{(1)} H/(k_\mathrm{B}T)\right) e^{-E_n^{(0)}/(k_\mathrm{B}T)}}. \tag{2.28}$$

For a paramagnet the magnetization is zero if no magnetic field is applied $M(H = 0) = 0$ and hence $\sum_n E_n^{(1)} e^{-E_n^{(0)}/(k_\mathrm{B}T)} = 0$, which can be used to simplify equation 2.28 and the final form of the susceptibility is obtained

$$\chi = \frac{N_\mathrm{A} \sum_n \left(E_n^{(1)2}/\left(k_\mathrm{B}T\right) - 2E_n^{(2)}\right) e^{-E_n^{(0)}/(k_\mathrm{B}T)}}{\sum_n e^{-E_n^{(0)}/(k_\mathrm{B}T)}}. \tag{2.29}$$

This is the Van Vleck formalism of the magnetic susceptibility named after John H. Van Vleck who as first considered second order perturbation terms. The Zeeman coefficients are obtained through perturbation theory

$$\begin{aligned} E_n^{(1)} &= \langle n|\hat{\mathcal{H}}_\mathrm{Zeeman}|n\rangle \\ E_n^{(2)} &= \sum_{m\neq n} \frac{\langle n|\hat{\mathcal{H}}_\mathrm{Zeeman}|m\rangle^2}{E_n^{(0)} - E_m^{(0)}}. \end{aligned} \tag{2.30}$$

First, the case of the total spin being zero $J = 0$ is considered. Intuitively, $\chi = 0$ is expected. The energy of the unperturbed ground level $E_0^{(0)}$ is set as energy origin and $E_0^{(1)}$ is zero. However, the second order Zeeman coefficient is non-zero and the susceptibility obtained is

$$\chi = -2N_\mathrm{A} \sum_{m\neq 0} \frac{\langle 0|\hat{\mathcal{H}}_\mathrm{Zeeman}|m\rangle^2}{E_n^{(0)} - E_m^{(0)}}. \tag{2.31}$$

The ground state mixes with the higher energy levels and the ground state features a finite magnetic moment despite J being zero. Note that the Van Vleck susceptibility given by equation 2.31 is often said to be temperature independent. This is only true if $E_n^{(0)} - E_m^{(0)} >> k_\mathrm{B}T$. There is no simple dependence on the temperature if the energy difference $E_n^{(0)} - E_m^{(0)}$ is comparable to the thermal energy $k_\mathrm{B}T$. Refs. [18] and [19] were used as references.

For the calculation of the susceptibility only the eigenenergies $E_n^{(0)}$ and the eigenstates $|n\rangle$ in zero magnetic field are necessary. The magnetic susceptibilities for the d-transition metal compounds were calculated by Kotani [15]. Kotani took the Hamiltonian for the central magnetic ion

$$\hat{\mathcal{H}} = \hat{\mathcal{H}}_0 + V_\mathrm{cubic} + \hat{\mathcal{H}}_\mathrm{SOC} + \hat{\mathcal{H}}_\mathrm{Zeeman} \tag{2.32}$$

in which the $\hat{\mathcal{H}}_0 + \hat{\mathcal{H}}_\mathrm{SOC}$ is the Hamiltonian of the free ion and $\hat{\mathcal{H}}_\mathrm{SOC}$ considers SOC. The crystalline electric field due to six surrounding ligands is assumed to have cubic

symmetry and the electrostatic energy is considered with V_{cubic}. Moreover, the large splitting is expected to favor low-spin complexes. The d^4 case treated by Kotani up to the second order of the magnetic field perfectly applies to Na_2RuO_3 with $J = 0$ (see Fig. 2.4) and equation (12) from Ref. [15] was used to describe the susceptibility (see Subsec. 4.1.2) of Na_2RuO_3. The SOC constant is the only free parameter.

2.5.2. Brillouin Function and Curie's Law

If the ground state carries a magnetic moment the resulting paramagnetism is stronger than the Van Vleck paramagnetism and second order perturbation terms can be neglected. $E_0^{(0)}$ is again set to zero. A magnetic field leads to the splitting of the degenerate J level and the energy of the split levels with the magnetic quantum numbers m_{J} ($m_{\text{J}} = -J, -J+1, ..., J-1, J$) is $E_{m_{\text{J}}} = -g\mu_{\text{B}} m_{\text{J}} H$ with the magnetic moment $\mu = g\mu_{\text{B}} m_{\text{J}}$. g is the Landé factor. When inserting the energy in equation 2.25 the sum runs over m_{J}. Equation 2.25 can be simplified and the magnetization is given by the Brillouin function $\mathcal{B}_{\text{J}}(y)$

$$M = M_{\text{S}} \mathcal{B}_{\text{J}}(y) \tag{2.33}$$

with the saturation magnetization $M_{\text{S}} = N_{\text{A}} g \mu_{\text{B}} J$. The Brillouin function is given by

$$\mathcal{B}_{\text{J}}(y) = \frac{2J+1}{2J} \coth\left(\frac{2J+1}{2J} y\right) - \frac{1}{2J} \coth \frac{y}{2J} \tag{2.34}$$

with $y = g\mu_{\text{B}} JB/k_{\text{B}}T$. The derivation can be found elsewhere [20]. The variable y sets two competing energies in relation. The Zeeman energy which tends to align the moments and the thermal energy which tends to disorder the moments. For high temperatures and low magnetic fields $y \ll 1$. With the Taylor expansion at 0 $\coth(x) = 1/x + x/3 + O(x^3)$ the magnetic susceptibility simplifies to

$$\chi = \frac{M}{H} \approx \frac{\mu_0 M}{B} = \frac{N_{\text{A}} \mu_0 g^2 \mu_{\text{B}}^2 J(J+1)}{3k_{\text{B}}T} = \frac{N_{\text{A}} \mu_0 \mu_{\text{eff}}^2}{3k_{\text{B}}T} = \frac{C}{T}. \tag{2.35}$$

This is Curie's law with the Curie constant C. Curie's law was already discovered experimentally and allows to determine the effective moment $\mu_{\text{eff}} = g\mu_{\text{B}}\sqrt{J(J+1)}$ from the temperature dependence of the magnetic susceptibility. This law is only valid if the magnetic moments do not interact.

2.5.3. Antiferromagnetism

If the magnetic moments interact the Weiss temperature θ_{CW} must be added to Curie's law to account for the exchange interactions and the Curie-Weiss law is obtained:

$$\chi = \chi_0 + \frac{C}{T - \theta_{\text{CW}}}. \tag{2.36}$$

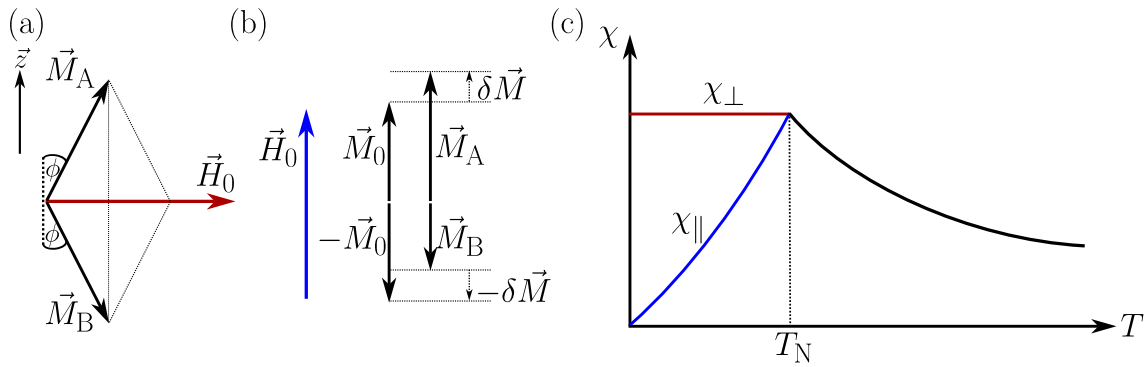

Figure 2.6.: Direction dependence of the magnetic susceptibility in antiferromagnets. (a) Application of the magnetic field perpendicular to the sublattice magnetization. (b) Application of the magnetic field parallel to the sublattice magnetization. (c) The perpendicular susceptibility stays constant below T_N whereas the parallel susceptibility decreases to zero.

χ_0 accounts for temperature independent contributions to the susceptibility such as diamagnetism or Van Vleck paramagnetism. θ_{CW} is a measure for the exchange interactions and positive for a ferromagnet and negative for an antiferromagnet. As only relevant in this work antiferromagnetism will be discussed in the following.

An antiferromagnet can be seen as two interpenetrating sublattices. The magnetic moments on one sublattice (A) point up and the magnetic moments on the other sublattice (B) point down. The magnetization of each sublattice creates a molecular or mean field acting on the other sublattice

$$\begin{aligned} \vec{H}_A &= -|\alpha|\vec{M}_B \\ \vec{H}_B &= -|\alpha|\vec{M}_A \end{aligned} \tag{2.37}$$

with the negative molecular field constant α. $|\vec{M}_A| = |\vec{M}_B|$, and the net magnetization is zero. Above the Néel temperature the magnetic order is destroyed and the material becomes paramagnetic and the susceptibility follows equation 2.36.

If a magnetic field is applied the susceptibility depends on the direction of the external field H_0. First, the susceptibility for small magnetic fields perpendicular to the axis of spontaneous magnetization, here the z axis, is considered. The scenario is illustrated in Fig. 2.6(a). The magnetization of both sublattices tilts leading to a magnetization along H_0. The susceptibility is

$$\chi_\perp = \frac{M}{H_0} = \frac{2M_A\phi}{H_0} \tag{2.38}$$

with the angle ϕ between the z axis and the direction of magnetization. Next, ϕ leading to a minimum in the total energy has to be determined. The three contributions to E_{tot} are

1. the mean field energy E_{mf} trying to align the sublattice magnetization antiparallel

$$\begin{aligned} E_{\mathrm{mf}} &= -\mu_0 \vec{M}_{\mathrm{A}} |\alpha| \vec{M}_{\mathrm{B}} \\ &= -\mu_0 |\alpha| M_{\mathrm{A}}^2 \cos(2\phi) \\ &\approx -\mu_0 |\alpha| M_{\mathrm{A}}^2 (1 - 2\phi^2) \end{aligned} \tag{2.39}$$

2. the Zeeman energy E_{H_0} trying to align the moments parallel to the external magnetic field

$$\begin{aligned} E_{\mathrm{H}_0} &= -\mu_0 (\vec{M}_{\mathrm{A}} \cdot \vec{H}_0 + \vec{M}_{\mathrm{B}} \cdot \vec{H}_0) \\ &= -2\mu_0 M_{\mathrm{A}} H_0 \sin\phi \\ &\approx -2\mu_0 M_{\mathrm{A}} H_0 \phi \end{aligned} \tag{2.40}$$

3. the energy E_{aniso} accounting for the fact that the magnetization prefers to orient along a specific crystallographic axis (the easy axis is here z)

$$E_{\mathrm{aniso}} = \kappa \sin^2\phi \approx \kappa\phi^2 \tag{2.41}$$

with the constant κ.

Minimizing $E_{\mathrm{tot}} = E_{\mathrm{mf}} + E_{\mathrm{H}_0} + E_{\mathrm{aniso}}$ with respect to ϕ leads to

$$\phi_{\mathrm{min}} = \frac{\mu_0 M_{\mathrm{A}} H_0}{2\mu_0 |\alpha| M_{\mathrm{A}}^2 + \kappa} \tag{2.42}$$

and the susceptibility from equation 2.38 becomes

$$\chi_\perp = \frac{1}{|\alpha| \left(1 + \frac{\kappa}{2|\alpha|\mu_0 M_{\mathrm{A}}^2}\right)} \approx \frac{1}{|\alpha|}. \tag{2.43}$$

The last approximation is valid if the anisotropy is weak compared to the mean field. Thermal fluctuations reduce the sublattice magnetization equally and the susceptibility stays constant up to T_{N}.

Next, the case of a small magnetic field parallel to the axis of magnetization is considered. The scenario is illustrated in Fig. 2.6(b). The local field of one sublattice is increased while the local field on the other sublattice is reduced and the susceptibility is given as

$$\chi_\parallel = \frac{M_\parallel}{H_0} \tag{2.44}$$

with $M_\parallel = 2\delta M$ where δM is the change of the magnetization of one sublattice. The net magnetization can also be expressed through the Brillouin function introduced earlier with equation 2.34

$$M_\parallel = M_{\mathrm{sat}} (\mathcal{B}_{\mathrm{J}}(y_{\mathrm{A}}) - \mathcal{B}_{\mathrm{J}}(y_{\mathrm{B}})). \tag{2.45}$$

In contrast to the paramagnetic case not only the external field but additionally the mean field contribution has to be considered. With $H_{\mathrm{A,eff}} = \vec{H}_0 + |\alpha|\vec{M}_0 - |\alpha|\delta M$ and $H_{\mathrm{B,eff}} = -\vec{H}_0 + |\alpha|\vec{M}_0 + |\alpha|\delta M$ the variables y_{A} and y_{B} are given by

$$y_{\mathrm{A}} = \frac{\mu_0 \mu_{\mathrm{B}} g J}{k_{\mathrm{B}} T}(|\alpha| M_0 + H_0 - |\alpha|\delta M) \tag{2.46}$$

$$y_{\mathrm{B}} = \frac{\mu_0 \mu_{\mathrm{B}} g J}{k_{\mathrm{B}} T}(|\alpha| M_0 - H_0 + |\alpha|\delta M). \tag{2.47}$$

For $|\alpha| M_0 \gg H_0, |\alpha|\delta M$ the Brillouin function can be expanded in the following way:

$$\mathcal{B}_{\mathrm{J}}(y_{\mathrm{A,B}}) \approx \mathcal{B}_{\mathrm{J}}(y_{\mathrm{A,B},H=0}) \pm \frac{\mu_0 \mu_{\mathrm{B}} g J}{k_{\mathrm{B}} T}(H_0 - |\alpha|\delta M) \frac{\mathrm{d}\mathcal{B}_{\mathrm{J}}}{\mathrm{d}y_{\mathrm{A,B}}}\bigg|_{y_{\mathrm{A,B}},H=0}. \tag{2.48}$$

Inserting equation 2.48 into equation 2.45 leads with $\delta M = M_{\parallel}/2$ and $M_{\mathrm{sat}} = N_{\mathrm{A}} \mu_{\mathrm{B}} g J/2$ to

$$M_{\parallel} = (2H_0 - |\alpha| M_{\parallel}) \cdot \frac{N_{\mathrm{A}} g^2 \mu_{\mathrm{B}}^2 J^2}{2 k_{\mathrm{B}} T} \frac{\mathrm{d}\mathcal{B}_{\mathrm{J}}}{\mathrm{d}y}\bigg|_{y,H=0}. \tag{2.49}$$

With the Curie constant C the susceptibility can be written as

$$\chi_{\parallel} = \frac{\frac{3J}{J+1} \cdot C \cdot \mathcal{B}'_{\mathrm{J}}(y, H=0)}{T + \frac{|\alpha|}{2} \cdot C \cdot \frac{3J}{J+1} \mathcal{B}'_{\mathrm{J}}(y, H=0)}. \tag{2.50}$$

For $T \to T_{\mathrm{N}}$ the sublattice magnetization is nearly lost and $y_{H=0} \to 0$. With the Taylor series expansion for $\coth(y)$ $\mathcal{B}'_{\mathrm{J}}(y_{H=0} \to 0) = \frac{J+1}{3J}$ is obtained and

$$\chi_{\parallel}(T_{\mathrm{N}}) = \frac{C}{T_{\mathrm{N}} + \frac{|\alpha|}{2} C} = \frac{1}{|\alpha|}. \tag{2.51}$$

In the last step $T_{\mathrm{N}} = \frac{|\alpha|}{2} C$ was used.

For $T \to 0$ $\mathcal{B}'_{\mathrm{J}}(y_{H=0} \to \infty) = 0$ and hence

$$\chi_{\parallel}(T \to 0) = 0. \tag{2.52}$$

The results for the susceptibilities are summarized in Fig. 2.6(c). If the external magnetic field parallel to the magnetization axis is increased further the system undergoes a spin-flop transition at a critical field.

For the calculation of the susceptibilities the following assumptions were made. The external magnetic fields are small compared to the mean fields. The interactions within a sublattice were neglected for simplicity. The mean field approach assumes that all regions within the sample are identical and correlations and fluctuations which become increasingly important near the critical temperature are ignored, which makes the mean field approach unsuited for the accurate description of critical regions. Ref. [21] was used as reference.

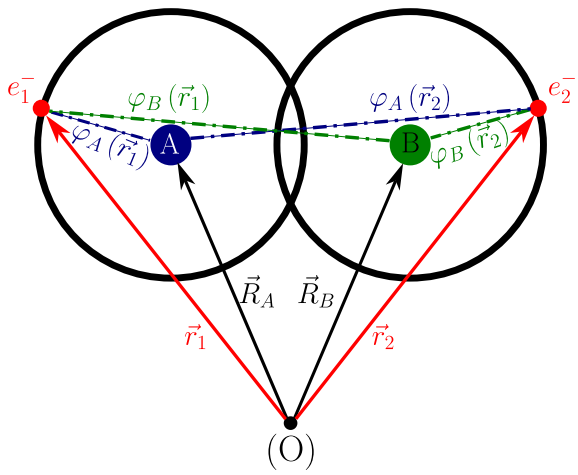

Figure 2.7.: Sketch of the hydrogen molecule to illustrate the labels referred to in the text.

2.6. Exchange Interactions

For the introduction of the exchange interaction the case of the H_2 molecule is considered. Nuclei A is located at $\vec{R}_A$ with the electron e_1^- at $\vec{r}_1$ and nuclei B is located at $\vec{R}_B$ with the electron e_2^- at $\vec{r}_2$ (see Fig. 2.7). The total Hamiltonian

$$\hat{\mathcal{H}} = \hat{\mathcal{H}}_A + \hat{\mathcal{H}}_B + \hat{\mathcal{H}}_{\text{int}} \tag{2.53}$$

contains the one-electron atomic Hamiltonians $\hat{\mathcal{H}}_A$ and $\hat{\mathcal{H}}_B$ and the Coulomb repulsion and attraction are considered in the interaction Hamiltonian $\hat{\mathcal{H}}_{\text{int}}$

$$\hat{\mathcal{H}}_{\text{int}} = \frac{e^2}{4\pi\epsilon_0}\left(\frac{1}{|\vec{r}_1 - \vec{r}_2|} + \frac{1}{|\vec{R}_A - \vec{R}_B|} - \frac{1}{|\vec{R}_A - \vec{r}_2|} - \frac{1}{|\vec{R}_B - \vec{r}_1|}\right) \tag{2.54}$$

which can be treated as perturbation. The total wave function can be separated into a spatial part $\varphi(\vec{r})$ and a spin part with α denoting spin-up and β spin down. The eigenstates are

$$\begin{aligned}
|\uparrow\uparrow\rangle &= \frac{1}{\sqrt{2(1-L^2)}}\alpha_1\alpha_2\left[\varphi_A(\vec{r}_1)\varphi_B(\vec{r}_2) - \varphi_A(\vec{r}_2)\varphi_B(\vec{r}_1)\right] \\
|\downarrow\downarrow\rangle &= \frac{1}{\sqrt{2(1-L^2)}}\beta_1\beta_2\left[\varphi_A(\vec{r}_1)\varphi_B(\vec{r}_2) - \varphi_A(\vec{r}_2)\varphi_B(\vec{r}_1)\right] \\
\frac{1}{\sqrt{2}}\left(|\uparrow\downarrow\rangle + |\downarrow\uparrow\rangle\right) &= \frac{1}{2\sqrt{(1-L^2)}}\left(\alpha_1\beta_2 + \beta_1\alpha_2\right)\left[\varphi_A(\vec{r}_1)\varphi_B(\vec{r}_2) - \varphi_A(\vec{r}_2)\varphi_B(\vec{r}_1)\right] \\
\frac{1}{\sqrt{2}}\left(|\uparrow\downarrow\rangle - |\downarrow\uparrow\rangle\right) &= \frac{1}{2\sqrt{(1-L^2)}}\left(\alpha_1\beta_2 - \beta_1\alpha_2\right)\left[\varphi_A(\vec{r}_1)\varphi_B(\vec{r}_2) + \varphi_A(\vec{r}_2)\varphi_B(\vec{r}_1)\right].
\end{aligned} \tag{2.55}$$

The first three states are triplets and the last state is a singlet with the energies

$$\begin{aligned} E_t &= 2E_0 + \frac{C_{AB} - I_{AB}}{1 - L^2} \\ E_s &= 2E_0 + \frac{C_{AB} + I_{AB}}{1 + L^2}, \end{aligned} \tag{2.56}$$

respectively. E_0 is the eigenenergy of the isolated hydrogen atom, C_{AB} is the Coulomb integral, I_{AB} is the exchange integral, and L is the overlap integral

$$\begin{aligned} C_{ab} &= \iint d^3r_1 d^3r_2 \varphi_A^*(\vec{r}_1)\varphi_B^*(\vec{r}_2)\hat{\mathcal{H}}_{\text{int}}\varphi_A(\vec{r}_1)\varphi_B(\vec{r}_2) \\ I_{ab} &= \iint d^3r_1 d^3r_2 \varphi_A^*(\vec{r}_2)\varphi_B^*(\vec{r}_1)\hat{\mathcal{H}}_{\text{int}}\varphi_A(\vec{r}_1)\varphi_B(\vec{r}_2) \\ L &= \int d^3r \varphi_A^*(\vec{r})\varphi_B^*(\vec{r}). \end{aligned}$$

The singlet-triplet splitting is

$$E_t - E_s = 2\frac{L^2 C_{AB} - I_{AB}}{1 - L^4} = 2J_{AB} \tag{2.57}$$

with the exchange coupling J_{AB}. For a sizeable overlap L $J_{AB} > 0$ is antiferromagnetic and the spin-singlet is the ground state of the hydrogen molecule. The antisymmetric spin part is connected to a symmetric spatial part of the wave function and the electron density between the nuclei A and B is non-zero in contrast to the antisymmetric spatial part. Ref. [22] was used as reference.

It should be noted that in insulating d-transition metal compounds the exchange is not carried by the direct exchange mechanism presented above because the magnetic ions are well separated by non-magnetic ions. Instead an indirect exchange between magnetic ions is mediated by non-magnetic ions.

For a many-body system the spin-spin Hamiltonian in a more general form is

$$\hat{\mathcal{H}} = \sum_{\langle ij \rangle} \hat{S}_i \mathbb{J}_{ij} \hat{S}_j \tag{2.58}$$

with the exchange matrix $\mathbb{J}_{ij}$ coupling the spins on sites i and j. The exchange matrix can often be simplified and some examples relevant for this work are given in the following.

In the Heisenberg model the exchange matrix $\mathbb{J}_{ij}$ reduces to a single value J_{ij}

$$\hat{\mathcal{H}}_{\text{Heisenberg}} = -\sum_{\langle ij \rangle} J_{ij} \hat{S}_i \hat{S}_j = -J \sum_{\langle ij \rangle} \hat{S}_i \hat{S}_j. \tag{2.59}$$

J can be written outside the sum if only nearest-neighbor (nn) interactions are considered.

The XXZ model is obtained from the Heisenberg model if an anisotropy parameter Δ_{aniso} is introduced

$$\hat{\mathcal{H}}_{\text{XXZ}} = J \sum_{\langle ij \rangle} \left(\hat{S}_i^x \hat{S}_j^x + \hat{S}_i^y \hat{S}_j^y + \Delta_{\text{aniso}} \hat{S}_i^z \hat{S}_j^z \right). \tag{2.60}$$

SOC can introduce Dzyaloshinsky-Moriya (DM) interaction between two spins

$$\hat{\mathcal{H}}_{\text{DM}} = \vec{D}_{ij} \cdot \left(\vec{S}_i \times \vec{S}_j \right). \tag{2.61}$$

The vector $\vec{D}_{ij}$ lies perpendicular to the plane spanned by the otherwise parallel or antiparallel spins. It becomes energetically favorable for spins to cant and for the case of $Na_2SrCo(PO_4)_2$ considered herein DM interactions introduce weak ferromagnetism in the antiferromagnet.

The symmetries of the lattice impose restrictions on the exchange matrix. Since needed later on it is noted that DM interactions are not allowed between spins connected via a bond with inversion symmetry $\mathbb{I}$

$$\mathbb{I} \left[\vec{D}_{ij} \left(\vec{S}_i \times \vec{S}_j \right) \right] = \vec{D}_{ij} \left(\vec{S}_j \times \vec{S}_i \right) = -\vec{D}_{ij} \left(\vec{S}_i \times \vec{S}_j \right). \tag{2.62}$$

If the bond has inversion symmetry $\vec{D}_{ij}$ must be zero. $\vec{D}_{ij}$ is non-zero if the inversion is broken for the bond. This is a necessary but not sufficient condition for DM interactions. The necessity for the absence of inversion is also easily seen when $\hat{\mathcal{H}}_{\text{DM}}$ from equation 2.61 is written in the form of equation 2.58 with

$$\mathbb{J}_{ij} = \begin{pmatrix} 0 & D_z & -D_y \\ -D_z & 0 & D_x \\ D_y & -D_x & 0 \end{pmatrix} \text{ and } \mathbb{J}_{ji} = -\mathbb{J}_{ij} = \begin{pmatrix} 0 & -D_z & D_y \\ D_z & 0 & -D_x \\ -D_y & D_x & 0 \end{pmatrix}. \tag{2.63}$$

Bond inversion symmetry allows only symmetric exchange and hence the antisymmetric DM interaction is forbidden.

2.7. Exotic Magnetism

2.7.1. Frustration

Two types of frustration can be distinguished. Geometrical and exchange frustration both illustrated in Fig. 2.8. For geometrical frustration to occur the lattice must meet the condition of connected triangular features such as found in the triangular, Kagome, and pyrochlore lattices. If the spins couple antiferromagnetically the exchange interactions can not be satisfied simultaniously. Exchange frustration can be found for example in honeycomb lattice compounds. Each lattice site is connected to three nearest neighbors. The Ising-type interactions depend on the specific bond and along each different bond one of the three different spin components couple.

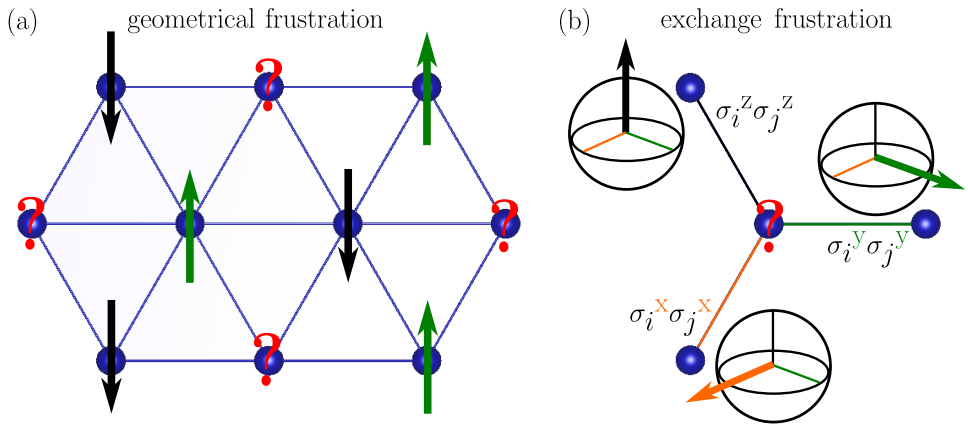

Figure 2.8.: Different types of frustration. (a) Geometrical frustration occurs if spins on a lattice with triangular features couple antiferromagnetically. The spins can not be arranged such that all the interactions are satisfied. (b) Exchange frustration arises if Ising-type interactions are bond dependent. Different spin components couple along different bonds. Figure redrawn from Ref. [23].

Commonly observed in frustrated systems are incommensurate magnetic structures. In this context the anisotropic triangular lattice is introduced and the results will be needed later for Na_3RuO_4. The study of frustrated magnets was largely motivated by the search for a QSL, but its existence in any material remains heavily debated in the community. The concept of QSLs will be given with focus on triangular lattice compounds, which will be taken up later in the light of the discussion of the spin-1/2 TLAFs $Na_2BaCo(PO_4)_2$ and $Na_2SrCo(PO_4)_2$.

2.7.2. Anisotropic Triangular Lattice

When exchange interactions compete often non-collinear and even incommensurate spin arrangements are formed as a compromise. The energetically most favorable spin arrangement can be often calculated analytically if classical spins $\vec{S}$ are considered. In the following the case of the anisotropic triangular lattice is illustrated. It will be needed later in the context of Na_3RuO_4. The situation is depicted in Fig. 2.9. The triangular lattice is spanned by $\vec{a}_1$ and $\vec{a}_2$ and nn interactions between the sites n_i, n_j are considered only. To create frustration J_1 is set to be antiferromagnetic ($J_1 > 0$) while J_2 can be ferromagnetic ($J_2 < 0$) or antiferromagnetic ($J_2 > 0$).

To find the ground state spin configuration which is defined by the propagation vector $\vec{k}$, the energy minimum has to be found. The total energy is obtained by

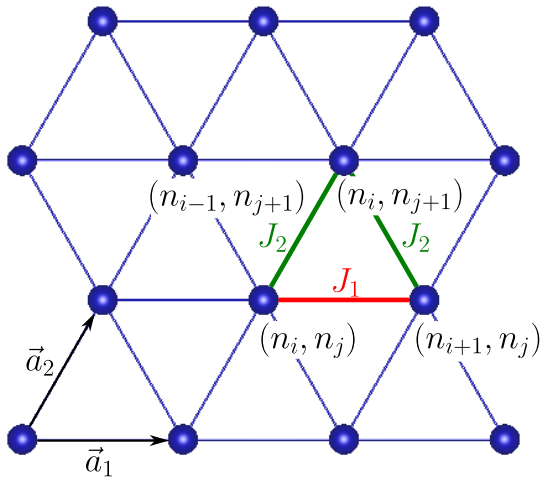

Figure 2.9.: The antiferromagnetic exchange interaction J_1 between nearest neighbors along $\vec{a}_1$ and the exchange interaction J_2 between nearest neighbors along $\vec{a}_2$ and $\vec{a}_2 - \vec{a}_1$ compete on the triangular lattice.

summing over all nearest neighbors:

$$\begin{aligned} E &= \sum_{n_i,n_j}^{N} \left[J_1 \vec{S}_{n_i,n_j} \vec{S}_{n_{i+1},n_j} + J_2 \left(\vec{S}_{n_i,n_j} \vec{S}_{n_i,n_{j+1}} + \vec{S}_{n_i,n_j} \vec{S}_{n_{i-1},n_{j+1}} \right) \right] \\ &= N S_0^2 \left\{ J_1 \cos\left(\vec{a}_1 \vec{k}\right) + J_2 \left[\cos\left(\vec{a}_2 \vec{k}\right) + \cos\left(\left(\vec{a}_2 - \vec{a}_1\right) \vec{k} \right) \right] \right\} \\ &= N S_0^2 \left\{ J_1 \cos\left(a k_x\right) + J_2 \left[\cos\left(\frac{a k_x}{2} \frac{\sqrt{3} a k_y}{2} \right) + \cos\left(-\frac{a k_x}{2} + \frac{\sqrt{3} a k_y}{2} \right) \right] \right\}. \end{aligned} \tag{2.64}$$

The equation can be simplified with $\cos\alpha + \cos\beta = 2\cos\left(\frac{\alpha+\beta}{2}\right)\cos\left(\frac{\alpha-\beta}{2}\right)$ to

$$E = N S_0^2 \left[J_1 \cos\left(a k_x\right) + 2 J_2 \cos\left(\frac{a}{2} k_x\right) \cos\left(\frac{\sqrt{3} a}{2} k_y \right) \right]. \tag{2.65}$$

By solving $\nabla E\left(k_x, k_y\right) = 0$ the propagation vector minimizing the energy is found to be:

$$\frac{\vec{k}}{2\pi/a} = \begin{cases} \begin{pmatrix} 0 \\ 0 \end{pmatrix} & \text{for } \frac{J_2}{J_1} \leq -2 \\ \begin{pmatrix} \frac{1}{\pi} \arccos\left(-\frac{J_2}{2J_1}\right) \\ 0 \end{pmatrix} & \text{for } \left|\frac{J_2}{J_1}\right| < 2 \\ \begin{pmatrix} 1 \\ 0 \end{pmatrix} & \text{for } \frac{J_2}{J_1} \geq 2. \end{cases} \tag{2.66}$$

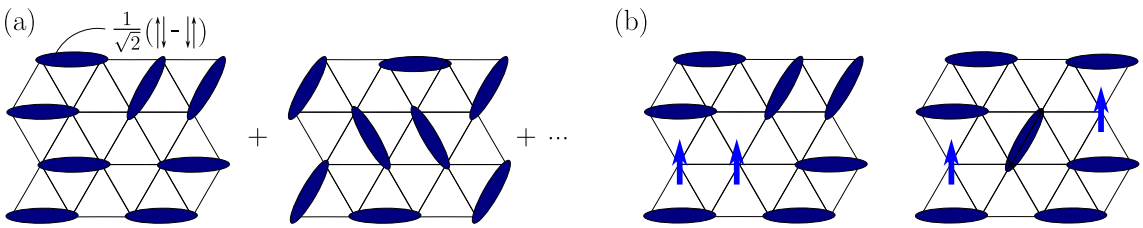

Figure 2.10.: Resonating valence bond model. (a) The resonating valence bond state is a superposition of all possible configurations of the spin singlets. (b) A spin-1 excitation can fractionalize into two spinons with spin 1/2.

An incommensurate order develops if the competing interactions are similar in size. If J_2 becomes the leading interaction the magnetic order is commensurate and the spins along the J_1 bond are oriented parallel.

2.7.3. Quantum Spin Liquids in Triangular Lattice Compounds

Even if the spins are strongly interacting frustration can lead to the absence of long-range magnetic order down to 0 K. This quantum state is called a QSL with a large degeneracy of the classical ground state and with long-range entangled spins. In contrast to a classical spin liquid in which the spins freeze at finite temperature because thermal fluctuations are necessary to switch between the different spin configurations, the QSL state realized in spin-1/2 systems is driven by quantum fluctuations and is a superposition of all possible configurations. Persistent spin dynamics can be found down to 0 K.

The QSL state was first introduced by Anderson as ground state for spin-1/2 triangular Heisenberg antiferromagnets. The resonating valence bond model based (see Fig. 2.10) on Pauling's model of benzene was used to describe the QSL state [24]. Any two spins that are antiparallel are arranged in pairs and form a $S = 0$ singlet state. The resonating valence bond state is a superposition of all possible pairing configurations. A spin-1 excitation in form of a spin flip can fractionalize into two so-called spinons with spin 1/2. The two unpaired spins can move independently through the crystal at no energy cost since all possible valence bond configurations share the same energy. Fractionalized excitations are key features in QSLs.

Now it is known that the nn isotropic Heisenberg antiferromagnet on a triangular lattice does not host a QSL state but develops long-range magnetic order. Theoretically and experimentally a non collinear 120 ° spin configuration was found [25, 26]. The same is true for the XXZ model presented in Sec. 2.6 [27]. Considering the symmetries of the isotropic triangular lattice the most general form of the exchange Hamiltonian from equation 2.58 can be re-written to [28]

$$\hat{\mathcal{H}} = \sum_m \left[\hat{\mathcal{H}}_m^{\mathrm{XXZ}} + \hat{\mathcal{H}}_m^{\pm\pm} + \hat{\mathcal{H}}_m^{\mathrm{z}\pm}\right]. \tag{2.67}$$

m larger than one accounts for interactions beyond nn interactions, the bond-independent XXZ part $\hat{\mathcal{H}}_m^{\mathrm{XXZ}}$ was already introduced in Sec. 2.6, and the remaining

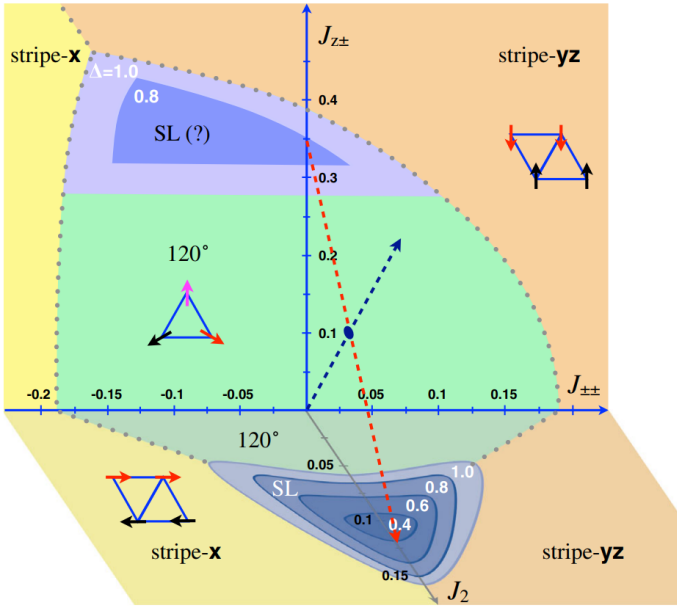

Figure 2.11.: Phase diagram of a TLAF in the parameter space J_2-$J^{\pm\pm}$-$J^{z\pm}$. A spin-liquid phase can be realized in the presence of nnn interaction J_2 or off-diagonal anisotropy $J^{z\pm}$. The third exchange interaction $J^{\pm\pm}$ accounts for the diagonal anisotropy. The ground state of the isotropic TLAF is the canted 120° spin structure. Figure taken from Ref. [2].

anisotropic bond dependent part contains diagonal components

$$\hat{\mathcal{H}}_m^{\pm\pm} = \sum_{\langle ij \rangle} 2J_m^{\pm\pm} \left[\left(S_i^x S_j^x - S_i^y S_j^y \right) \cos\phi_\alpha - \left(S_i^x S_j^y + S_i^y S_j^x \right) \sin\phi_\alpha \right] \tag{2.68}$$

and off-diagonal components

$$\hat{\mathcal{H}}_m^{z\pm} = \sum_{\langle ij \rangle} J_m^{z\pm} \left[\left(S_i^y S_j^z + S_i^z S_j^y \right) \cos\phi_\alpha - \left(S_i^x S_j^z + S_i^z S_j^x \right) \sin\phi_\alpha \right] . \tag{2.69}$$

$\phi_\alpha = \{0, 2\pi/3, -2\pi/3\}$ accounts for the bond dependency in a lattice with three-fold symmetry.

A delicate interplay between bond-directional exchange interactions and next nearest neighbor (nnn) interactions J_2 can push the system into a QSL state as illustrated in the phase diagram in Fig. 2.11 [2, 3, 28–30]. Only 6% nnn interactions with respect to the isotropic nn interaction are sufficient to stabilize a QSL phase. It is still under debate whether a QSL can be realized by bond-dependent interactions without the presence of nnn interactions [31, 32]. Concerning the bond-independent exchange interactions, an isotropic regime with $\Delta_{\text{aniso}} = 1$ is desirable because increasing XXZ anisotropy leads to the shrinking of the QSL window in the J_2-$J^{\pm\pm}$-$J^{z\pm}$ parameter space.

2.7.4. Excitonic Magnetism

SOC is a key factor that leads to novel exotic states in $4d$ and $5d$ transition metal systems. Widely studied is the spin-orbit Mott insulating state, which is found in numerous compounds [33–35]. d^5 systems with spin-orbit entangled $J = 1/2$ pseudospins on a honeycomb lattice with edge-shared octahedra are extensively investigated in the context of Kitaev physics. Frustration induced by bond-dependent Ising interactions (see Fig. 2.8) leads to a QSL ground state [36–39].

In d^4 systems (Re^{3+}, Ru^{4+}, Os^{4+}, Ir^{5+}) with octahedrally coordinated ions, four electrons reside on the t_{2g} level if the crystal field splitting exceeds the Hund's coupling and a low-spin ($S = 1$, $L = 1$) configuration is realized. SOC leads to the formation of a $|J = 0\rangle$ ground state singlet and the system is non-magnetic (see Fig. 2.4). However, novel magnetism referred to as excitonic magnetism is induced through the condensation of the excited $|J = 1\rangle$ states [40, 41]. The formation of the spin-orbit entangled excitons is only possible, if the exchange interactions overcome the energy gap between the $|J = 0\rangle$ and $|J = 1\rangle$ states of a single d^4 ion [41]. Since the energy gap is proportional to the SOC strength, $4d$ systems are more promising candidates than $5d$ systems to host excitonic magnetism. Ca_2RuO_4 is a compound which fulfills the prerequisites, also because trigonal distortions of the RuO_6 octahedra split the $|J = 1\rangle$ levels and thus decrease the gap size. Indeed, in Ca_2RuO_4 condensation of $|J = 1\rangle$ excitons was reported [42–44].

Due to the inherited orbital contribution, excitonic interactions are anisotropic. This property can be exploited by appropriately choosing the crystal structure and thus adding frustration to the system. Especially 90 °M-O-M exchange geometry as found in honeycomb lattices with edge-shared octahedra is suited to combine quantum criticality and frustration. To describe this system, the $J = 1$ excitations are introduced as bosons called triplons which come in three different flavors. In the extreme case, the three different bond-types are connected each with a different flavor of the interaction. This can be regarded as bosonic analogue of the spin-1/2 Kitaev model. One similarity is the suppression of magnetic condensation. [41, 45]

This rather new physics has not been studied in detail in real materials. Due to dimerization, Li_2RuO_3 is not suited as model compound [46]. Na_2RuO_3 reportedly avoids dimerization [47, 48] but its ground state is highly debated [49–51].

3. Experimental Details

In this chapter the experimental procedures are presented in the same order as carried out in the lab. Unarguably the first step is the powder or single crystal synthesis. Recipes found in the literature are often not reproducible right away and have to be adapted. This is due to sometimes rough descriptions or simply different conditions in the labs. In both cases an unambiguous account facilitates the reproducibility and detailed instructions are given in Subsec. 3.1.3. A list of the conducted experiments on each compound is given in Table 3.1. In the following sections the theoretical basics, and the measurement principles and devices are introduced before the sample preparation is described. Since the theoretical basics of diffraction and magnetization were already given in Chap. 2, only the measurement setup will be described in the Secs. 3.2 and 3.5.

Table 3.1.: Overview of the conducted experiments on the four investigated compounds.

	Na_2RuO_3	Na_3RuO_4	$Na_2BaCo(PO_4)_2$	$Na_2SrCo(PO_4)_2$
X-ray powder diffraction (XRPD)	✓	✓	✓	✓
Synchrotron XRPD			✓	✓
Neutron powder diffraction (NPD)		✓		
Nuclear magnetic resonance (NMR)			✓	
Magnetization (^{4}He)	✓	✓	✓	✓
Magnetization (^{3}He)			✓	✓
Heat capacity (^{4}He)	✓	✓	✓	
Heat capacity (^{3}He)			✓	✓
Heat capacity dilution refrigerator			✓	
Resonant inelastic x-ray scattering (RIXS)	✓			

3.1. Synthesis

3.1.1. Horizontal Furnace

Often, chemical reactions at higher temperatures have to be carried out in an inert atmosphere to prevent the educts and products from oxidization. One way is to seal the crucible with the chemicals into a quartz ampule which can be either evacuated or filled with an inert gas [see Fig. 3.1(a)]. If gaseous by-products form during the synthesis, a sealed ampule cannot be used. In this case, the synthesis can be performed in a horizontal tube furnace as shown in Fig. 3.1(b). An alumina combustion boat containing the educts is placed in the middle of the quartz tube (Aachener Quarzglas, RQ200 and HSQ100, $\varnothing 32 \pm 0.5\,\mathrm{mm} \times 2 \pm 0.2\,\mathrm{mm} \times 1000\,\mathrm{mm}$) at the heater. Customized gas flows through the pipe can be set with a flow meter. Except for the intercalation of Li_2RuO_3 every synthesis was carried out in the horizontal tube furnace.

3.1.2. Flux Growth and Solid State Reaction

Polycrystalline Na_2RuO_3, Na_3RuO_4, and Li_2RuO_3 samples were synthesized via solid state reaction. The powders used as starting materials are mixed and ground thoroughly to ensure good homogeneity and a large surface area. The mixture is heated in a controlled way to higher temperatures and held there, since the reaction is carried by solid state diffusion. After the reaction is completed the compound is cooled to room temperature.

$Na_2BaCo(PO_4)_2$ and $Na_2SrCo(PO_4)_2$ single crystals were grown with the flux method. All educts are dissolved in a flux media at sufficiently high temperatures. When the solution is slowly cooled down, nucleation points will form out of a supersaturated solution. To reach supersaturation again the solution has to be cooled down further and continuous cooling leads to the growth of the precipitates. The growth procedure will eventually stop, when the temperature falls below the melting point.

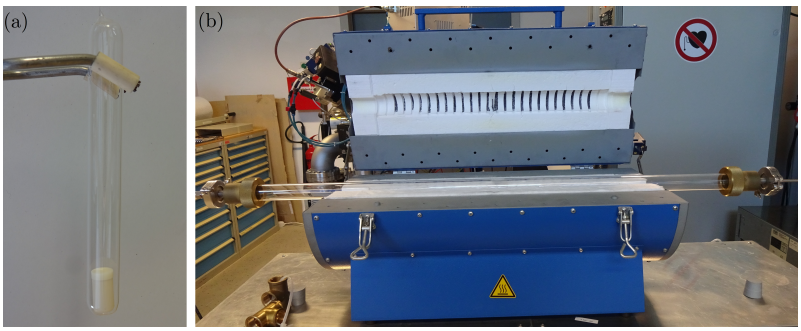

Figure 3.1.: Synthesis in controlled atmospheres. (a) Alumina crucible with lid in a quartz ampule filled with Ar. (b) Different gas flows can be realized in a horizontal furnace.

3.1.3. Synthesis Procedure

Na_2RuO_3

Refs. [49] and [50] propose the self-flux method as direct way to synthesize powder and single crystals. Na_2CO_3 and RuO_2 were mixed in a slightly off-stoichiometric ratio (1.1:1) and heated in steps up to 1100 °C. This direct synthesis route in air and in an inert Ar atmosphere and its variations with lowered temperatures to prevent evaporation failed. Indeed, the single crystals in Ref. [49] seem to be miscategorized as Na_2RuO_3 and the described properties strongly resemble those of Na_3RuO_4. Here, powder samples of Na_2RuO_3 were obtained in a two-step synthesis as suggested in Ref. [47]. In a first step, the precursor powder compound Na_2RuO_4 was synthesized by solid state reaction. Following the steps described in Ref. [52], stoichiometric amounts of Na_2O_2 (96% Arcos Organics) and RuO_2 (99.9% Alfa Aesar) were mixed and ground together in an agate mortar in an Ar glove box. The mixture was placed in an alumina combustion boat and heated in the following way in an O_2 flow (20 sccm). In 10 hours the mixture was first heated to 450 °C and held there for 5 hours, and was next heated in 2 hours to 530 °C and held there for 10 hours. Finally the sample was heated in 3 hours to 630 °C and held there for 15 to 20 hours. After intermediate grinding, the mixture was again loaded in the horizontal furnace and heated in 3 hours to 630 °C in an O_2 flow (20 sccm). After 50 hours at 630 °C black-green Na_2RuO_4 powder was obtained. The Na_2RuO_4 powder was ground in a glove box and reduced in the second step to Na_2RuO_3 by heating the compound in 3 hours to 850 °C in a reducing Ar flow (20 sccm). After 48 hours black Na_2RuO_3 powder was obtained. The powder is mildly air-sensitive and was finally ground in a glove box and always stored in Ar atmosphere.

For all measurements powder samples were prepared. Plastic capsules filled with about 6 mg of the powder were prepared for magnetization measurements up to 400 K. For measurements at higher temperatures a 5 mm pellet was glued to the sample holder. For heat capacity measurements a 4.7 mg piece of a pressed pellet and for RIXS measurements a 3 mm pellet was used.

So far, no single crystals of this compound have been synthesized and their synthesis was beyond the scope of this work. The two-step method described above is rather unsuited on the way to single crystals and a direct method would be advantageous. Growing single crystals directly from the pure powder is also unlikely. In the case of Na_2IrO_3 the powder is heated 150 °C above the maximum temperature during the powder synthesis and is then slowly cooled down to obtain single crystals [35]. Na_2RuO_3 is thermally not stable enough and oxidizes to Na_3RuO_4 if hold too long (approximately four days) at 850 °C even in an Ar flow. The additional heat treatment was originally intended to reduce stacking faults and improve crystallinity, but due to the formation of Na_3RuO_4 further heat treatments were renounced. Na_3RuO_4 often formed as by-product during the synthesis attempts and the targeted synthesis is described in the next paragraph.

Finally, a small excursion into interlayer tuning of Li_2RuO_3 will be given as

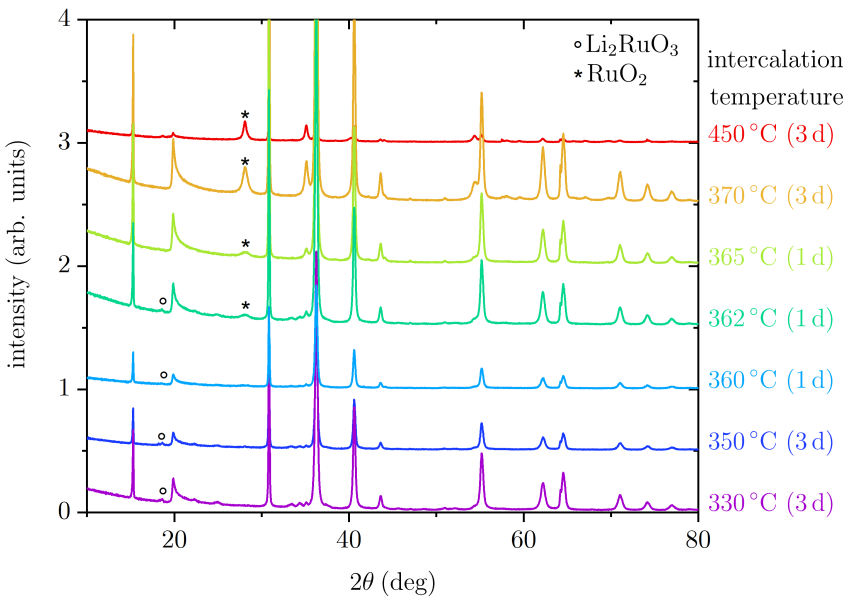

Figure 3.2.: Room temperature XRPD patterns of Cu intercalated Li_2RuO_3 synthesized at temperatures between 330 and 450 °C. The open circles mark the peak originating from the parent Li_2RuO_3 compound and the asterisks mark the peak stemming from the decomposition product RuO_2. Both Li_2RuO_3 and RuO_2 can be detected in the sample synthesized at 362 °C.

different route to new layered ruthenates. Starting material is Li_2RuO_3 which was synthesized in a straightforward manner by mixing stoichiometric amounts of Li_2CO_3 (99.998% Alfa Aesar) and RuO_2. The mixture was loaded in an alumina crucible and heated in air in 4 hours to 1000 °C and held at 1000 °C for 24 hours [53]. In the next step, the Li^+ ions separating the Ru honeycomb slabs were exchanged with Ag^+ ions. The Ru layers contain Li^+ ions as well but those Li^+ ions were not replaced. An excess of $AgNO_3$ powder (99.9995% Thermo Fisher) was added to the Li_2RuO_3 powder in an alumina crucible. The crucible with lid was sealed in a quartz ampule with Ar atmosphere [see Fig. 3.1(a)]. The ampule was placed in a preheated muffle furnace and was left for 3 days at 250 °C. Afterwards, the $AgNO_3$ excess was removed by washing the sample several times with distilled water and finally with acetone. The growth method was adapted from Ref. [54], who reported phase pure powder samples of $Ag_3LiRu_2O_6$ before.

For Cu intercalated Li_2RuO_3 the procedure was slightly adapted. Instead of $AgNO_3$ CuCl (99.995% Carl Roth) was used and the excess had to be removed with diluted hydrochloric acid. Main difference and resulting problem is the temperature during the intercalation. This is illustrated in Fig. 3.2 showing the room temperature diffraction data for samples synthesized at different temperatures. At the lower intercalation temperatures (330 to 362 °C) the ion exchange is not complete and Li_2RuO_3 is still present (open circles in Fig. 3.2). Above 360 °C the compound decomposes and RuO_2 is formed (see asterisks in Fig. 3.2). In the samples synthesized

at 362 °C the parent compound Li_2RuO_3 and the decomposition product RuO_2 can both be detected and completely Cu intercalated Li_2RuO_3 is not possible because the compound decomposes before all Li_2RuO_3 is intercalated.

Na_3RuO_4

Na_3RuO_4 powder was synthesized by following a slightly modified version of the recipe from Ref. [55]. RuO_2 was pre-dried for 2 hours at 700 °C and mixed with NaOH (99.99% Alfa Aesar) in a small off-stoichiometric molar ratio 1 : 3.1. The small excess of NaOH was chosen to avoid RuO_2 impurities in the sample. RuO_2 impurities form easily during syntheses of Ru based compounds and are difficult to remove afterwards. The educts were ground together in an Ar glove box and loaded in an alumina combustion boat. In the horizontal furnace the mixture was heated in an O_2 flow (20 sccm) in 2 h to 500 °C and held at this temperature for 18 h. After grinding the powder in the glove box the sample was again heated in the horizontal furnace. In this second step, the powder was heated in a mixed Ar + O_2 flow (3 : 1, 20 sccm) in 2 h to 650 °C and held there for 18 h. The Na_3RuO_4 powder was finally ground in the glove box. To improve the crystallinity a tempering step was added. Similar to the second step, the sample was heated to 650 °C in the mixed Ar + O_2 flow but with slower heating and cooling rates. The sample was heated to 650 °C in two days, held there for three days, and was finally cooled down to room temperature within three days.

All measurements were conducted on powder. For magnetization measurements 7.9(2) mg powder was filled in a plastic capsule. For heat capacity measurements a pellet was pressed and tempered. A 5.41(7) mg piece was mounted on the platform. For NPD measurements the powder from seven different batches were tempered, mixed, and ground together in an Ar glove box. The vanadium container was loaded with 3.45 g of the powder and sealed in a glove box to avoid decomposition of the hygroscopic powder.

$Na_2BaCo(PO_4)_2$

The flux growth synthesis of $Na_2BaCo(PO_4)_2$ single crystals was first reported in Ref. [4] and described as follows. Stoichiometric amounts of the reactants Na_2CO_3, $BaCO_3$, CoO, and $(NH_4)_2HPO_4$ were ground together with the flux media NaCl. The mixture was heated in air to 950 °C. Pink single crystals formed during the cooling to 750 °C. Reproducing single crystal growth with these instructions was not possible in our lab. Some crucial parts of the synthesis had to be adjusted to obtain single crystals. The temperature was lowered to 850 °C, the more active $Co(NO_3)_2$ was used as Co source and the atmosphere was changed from air to N_2 to prevent the oxidization of cobalt. The procedure was as follows. In an Ar glove box the educts Na_2CO_3 (99.999% Sigma-Aldrich), $BaCO_3$ (99.997% Alfa Aesar), $Co(NO_3)_2{\cdot}6H_2O$ (99.999% Sigma-Aldrich), and $(NH_4)_2HPO_4$ (99% Grüssing GmbH) were mixed in stoichiometric amounts and ground together in an agate mortar with

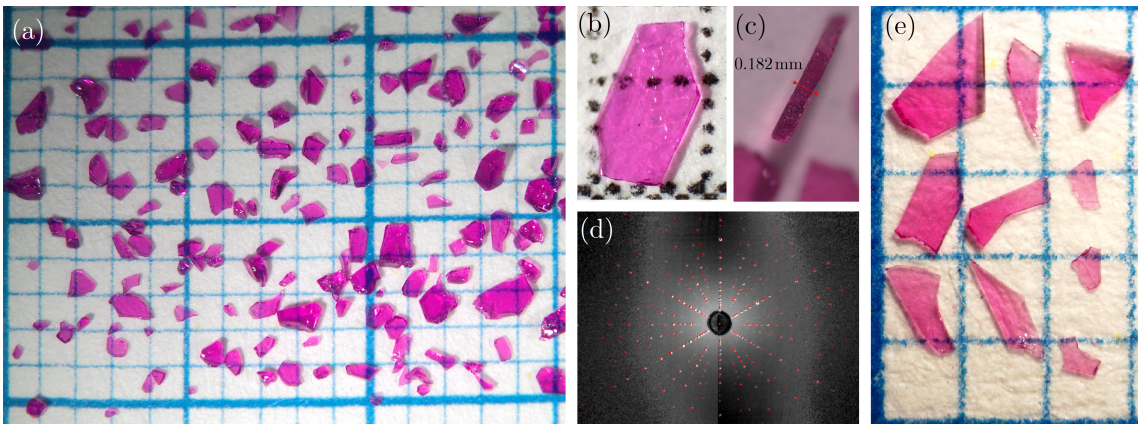

Figure 3.3.: Single crystals. (a) Single crystals of $Na_2BaCo(PO_4)_2$ from approximately four different batches. (b) Largest $Na_2BaCo(PO_4)_2$ single crystal in terms of area. The crystal has a weight of around 0.26 mg and was used for ^{3}He heat capacity measurements. (c) The thickness of $Na_2BaCo(PO_4)_2$ single crystals is usually around 200 μm. (d) Laue diffraction pattern of a $Na_2BaCo(PO_4)_2$ single crystal. The pattern can be indexed with a trigonal space group. (e) Single crystals of $Na_2SrCo(PO_4)_2$.

the flux medium NaCl (99.99% Alfa Aesar) (Co : Cl 1 : 25). In the horizontal furnace the mixture in the alumina combustion boat was heated from room temperature in 2 hours to 850 °C and cooled to 750 °C with a rate of 3 K/h. A lower cooling rate of 1 K/h had no impact on the crystal size. The reaction was conducted in a N_2 flow (20 sccm). The pink crystals, which grew in the end regions of the combustion boat, were detached mechanically with spatula and tweezers and/or the crucible was immersed in distilled water. Afterwards, the crystals were cleaned with distilled water in an ultrasonic bath to remove residuals from the growth. Finally, the crystals were manually sorted out under a microscope. The crystals are thin platelets with an average size of 1 mm^2 and a thickness usually of around 200 μm [Fig. 3.3(a)-(d)]. Magnetization, heat capacity, thermal expansion, magnetostriction, magnetocaloric, and NMR were measured on single crystals with a weight below 1 mg. A 6.13(1) mg single crystal was used for ^{4}He heat capacity measurements because larger sample masses are required. Powder for high-resolution synchrotron XRPD measurements were prepared by grinding single crystals from seven different batches. The powder was filled in a quartz capillary with a radius of 0.5 mm and sealed with grease.

$Na_2SrCo(PO_4)_2$

The single crystal growth of $Na_2SrCo(PO_4)_2$ is analogous to $Na_2BaCo(PO_4)_2$. Different Sr sources ($SrCl_2$, $SrCO_3$, and $Sr(NO_3)_2$) were tested in combination with different Co sources ($Co_2C_2O_4$ and $Co(NO_3)_2{\cdot}6H_2O$). Clean crystals were only obtained with the educts $SrCl_2$ (anhydrous, 99.5% Alfa Aesar) and $Co(NO_3)_2{\cdot}6H_2O$ and a cooling rate of 1.5 K/h. In contrast to $Na_2BaCo(PO_4)_2$, the crystals did not form in the end regions of the combustion boat but in the center together with

other phases. The purity, amount, and size of the crystals varied from one batch to another and the growth procedure was not always successful. The yield was always lower compared to the $Na_2BaCo(PO_4)_2$ synthesis. Pink crystals also formed on the quartz tube suggesting that the growth is not exclusively carried by flux growth but also by vapor transport. The $Na_2SrCo(PO_4)_2$ crystals are comparable in size to the $Na_2BaCo(PO_4)_2$ crystals but show a lower thickness [see Fig. 3.3(e)]. Magnetization and heat capacity were measured on single crystals. Due to the light weight of the sample, the heat capacity measurements were limited to temperatures up to 10 K. For synchrotron XRPD the single crystals obtained from nine batches were ground. To allow for a proper mounting, the quartz capillary has to be filled approximately up to 2 cm. A crushed quartz capillary was used as filler material and the quartz powder was carefully placed on top of the $Na_2SrCo(PO_4)_2$ powder.

3.2. Diffraction

3.2.1. X-ray Powder Diffraction

The used educts were first checked with the benchtop diffractometer `MiniFlex600` from Rigaku equipped with a fixed x-ray tube operated at 40 kV and 15 mA. The diffraction data were collected in Bragg-Brentano geometry and with CuK_α radiation ($\lambda_{K_\alpha} = 1.5418$ Å). A 5.0 ° Soller slit in the incoming beam path limited the axial divergence. A 10 mm mask limited the beam height and a 1.250 ° divergence slit limited the angular divergence. A 5.0 ° Soller slit and a 13 mm anti-scatter slit to reduce beam scatter were placed in front of the D/teX Ultra2 detector. The powder was attached with grease onto a Si single crystal sample holder with zero background.

The control of the sample quality and a first structural characterization were performed in-house using the x-ray diffractometer `EMPYREAN` from Panalytical. The samples were as well measured with CuK_α radiation in Bragg-Brentano geometry but in this setup, the position of the spinning sample holder was fixed and tube and detector moved in $\theta - \theta$ geometry. The x-ray tube was operated at 40 kV and 40 mA. The incident beam optic module contained a 1/8 ° divergence slit, a 10 mm fixed mask, a focusing mirror, a 0.04 rad Soller slit, and a 1/2 ° anti-scatter slit. The optic module in front of the 1D-line detector ($PIXcel^{3D}$) contained a 7.5 or 8 mm anti-scatter slit, and a 0.04 rad Soller slit. An obliquely cut silicon crystal with zero background was used as sample holder. Small amounts of powder are sufficient and were sprinkled onto the sample holder with a drop of isopropanol.

In general, the program `JANA2006` [56] was used to refine structural models. To quantify the amount of stacking faults in Na_2RuO_3, the diffraction pattern was simulated with `GSAS-II` [57] using the `DIFFaX` routine [58, 59]. Since for the `DIFFaX` routine a unit cell with $\alpha, \beta = 90\,°$ is necessary, the monoclinic unit cell had to be transformed into a cartesian coordinate system first. In a second step, the faulted stacking vector and the ratio of ideal and faulted stacking had to be chosen [59].

The powder diffraction pattern was then simulated in recursive mode under the assumption of an infinite number of layers.

3.2.2. Synchrotron X-ray Powder Diffraction

To go beyond the resolution obtained with the laboratory x-ray diffraction, the wavelength has to be further decreased. At the ID22 beamline of the European Synchrotron Radiation Facility (Grenoble, France) high-resolution synchrotron XRPD measurements were performed with a wavelength of 0.35423 Å. The experiments were performed with Alexander A. Tsirlin and the beamline scientists Andy Fitch, Catherine Dejoie, and Ola Grendal. The data for $Na_2BaCo(PO_4)_2$ were collected at ALBA (Barcelona, Spain) with a wavelength of 0.35405 Å by Aleksandr Zubtsovskii and Alexander A. Tsirlin.

The electrons for the synchrotron are produced with an electron gun and are pre-accelerated in a linear accelerator. Before entering the storage ring, the electrons are accelerated in a booster synchrotron. In the storage ring the electrons are kept close to the speed of light by synchronizing the frequency of the electric field to the orbital period of the electrons which becomes larger due to relativistic mass increase. Additionally, the magnetic field strength has to be increased to maintain the orbital path. Tangential to the direction of movement the accelerated charged particles emit electromagnetic radiation in form of synchrotron radiation which is guided to the beamlines.

For the measurements, quartz capillaries were filled with fine powder obtained from grinding single crystals. Based on the calculation of x-ray absorption for different diameters of the capillaries, a suited capillary was chosen to ensure a good balance between the amount of sample and the level of absorption. The beamline is equipped with different options to set various temperature windows. For the $Na_2BaCo(PO_4)_2$ sample the temperatures between 10 and 225 K were set with a He flow cryostat and the temperatures between 150 and 300 K with a N_2 flow cryostream. For the $Na_2SrCo(PO_4)_2$ sample the He flow cryostat was used for temperatures between 10 and 220 K, the N_2 flow cryostream for temperatures between 150 and 450 K, and the hot-air blower was used to cover the temperatures between 450 and 1025 K. Structural models were refined with JANA2006 [56].

3.2.3. Neutron Powder Diffraction

At the Institut Laue-Langevin (Grenoble, France) neutrons are created by fission. NPD experiments on Na_3RuO_4 were performed under supervision of the local contact Clemens Ritter. The measurements were conducted at the two-axis diffractometers D2B and D20 sketched in Fig. 3.4. The high resolution of the instrument D2B is achieved by the large take-off angle of 135 ° of the Ge monochromator and two collimators. The first one collimates the polychromatic beam and the second radial collimator is located in front of the detector. The 2D-detector consists of 128 ^{3}He detector tubes which are spaced in 1.25 ° intervals. The diffraction pattern is

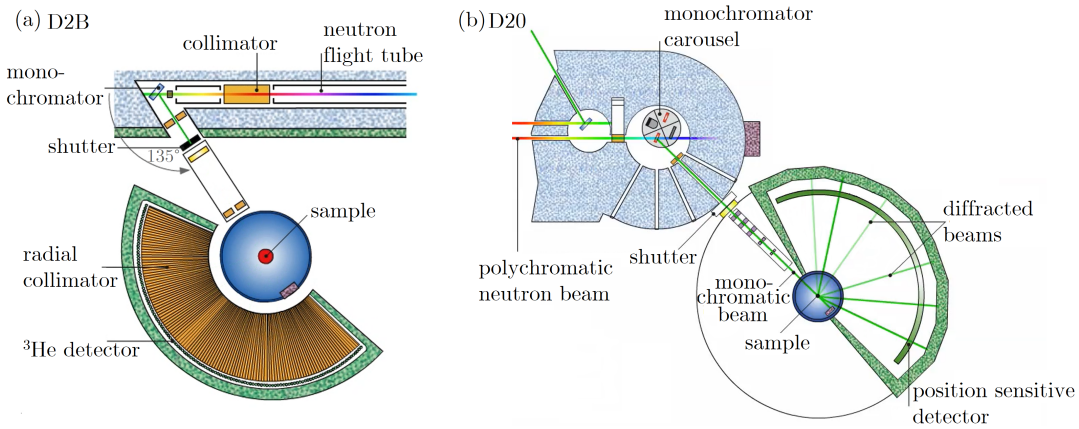

Figure 3.4.: NPD beamlines at which the data were collected. (a) Instrument `D2B` is a high-resolution diffractometer with large take-off angle of the monochromator and two collimators. (b) High-intensity instrument `D20` with a static detector. The figures were adapted from Ref. [61].

recorded by moving the detector and the intensity is summed over several detectors. A cryostat as sample environment offers a base temperature of 1.5 K. Due to the high resolution, the first experiments were performed at `D2B` to characterize the crystal structure in dependence of the temperature and to seek for possible structural phase transitions. At a wavelength of 1.594 Å five shorter scans at 300, 250, 200, 150, and 100 K and three longer scans of 4.5 h at 40, 27, and 1.5 K were recorded. The experimental setup is always a trade-off between resolution and intensity but magnetic Bragg peaks could already be observed with the instrument `D2B`.

To study the magnetic structure, measurements were performed at the beamline `D20` with the wavelength 2.415 Å. The collimators are omitted and a static detector allows to collect high intensity data. First, a thermodiffractogram (117 measurements, 10 minutes each) was recorded by ramping the temperature from 5 to 40 K (0.03 K/min). The magnetic thermodiffractogram was obtained by subtracting the nuclear background measured at 40 K. After this first overview, 2 h measurements at the selected temperatures 1.5, 10, 15, 20, 23, 25, 27, 29, 31, and 40 K were performed for future refinement of the magnetic structure. Instead of the 40 K data, the 31 K data were used as nuclear background for a better subtraction of the nuclear Bragg peaks. The structural models were refined with `FullProf` [60].

3.3. Spectroscopy

3.3.1. Nuclear Magnetic Resonance

In NMR spectroscopy, nuclei with non-zero nuclear spin I act as probes for local fields. One of the probe nucleus looked at later is ^{31}P with $I = 1/2$. In a static magnetic field with flux density B_0, Zeeman splitting lifts the degeneracy of the $m_s = \pm 1/2$ levels with the energy difference $\Delta E = \gamma \hbar B_0 = \hbar \omega_L$ between the Zeeman levels. The gyromagnetic ratio of a nuclei γ is of the order of several MHz/T and with laboratory fields of a few Tesla, pulses in the radio frequency range lead to resonance [62]. For resonance, the radio frequency has to match the Larmor frequency ω_L with which the nuclear spins precess around the axis of B_0.

Beside the external magnetic field, internal fields are probed and lead to a shift of the resonance frequency. The surrounding environment of the nuclei can have shielding or de-shielding effects, leading to a chemical shift constant with temperature. The nuclear spins can also couple to the electron spin of the magnetic ion. This coupling is expressed in the most general case via the hyperfine coupling tensor $\bar{\bar{A}}$.
The associated temperature-dependent shift is also referred to as Knight shift and is connected to the local spin susceptibility χ_s in the paramagnetic state as follows [65]

$$K(T) = \bar{\bar{A}} \bar{\bar{\chi}}_s(T). \tag{3.1}$$

Nuclei with spins larger than 1/2, like ^{23}Na with $I = 3/2$, have a non-spherically symmetric electric quadrupolar moment which interacts with the surrounding electric field gradients [see Fig. 3.5(a)]. Instead of one resonance line, satellites form in accordance with first-order perturbation theory. Second-order quadrupolar interactions affect all level splittings including the central transition, which causes unequal shifts of the satellites with respect to the central transition [63].

In general, the interactions are anisotropic. This results in a line broadening in the case of polycrystalline samples and a loss of spectral resolution. To overcome this problem, the powder samples are spun rapidly around an axis which is tilted by 54.74° from the external magnetic field axis. This method is called magic angle spinning (MAS). The angular dependence of the dipolar coupling, the chemical shift, and the first-order quadrupolar coupling are given, inter alia, by a second-order Legendre polynominal $P_2(\cos\theta) = 0.5 \cdot (3\cos\theta^2 - 1)$, with the angle θ between the vector connecting two spins and the magnetic field axis. Fast spinning around the magic angle axis leads to an averaging of the interaction components perpendicular to that axis and thus a complete annihilation in the case of interactions described with the second-order Legendre polynominal. [66]

NMR measures additionally the dynamics in the system. At resonance, the nuclear spins become phase coherent and a $\pi/2$ pulse rotates the spins into the plane perpendicular to B_0. The transverse magnetization induces a current in a coil. The signal decays with time because the transverse magnetization is lost due to dephas-

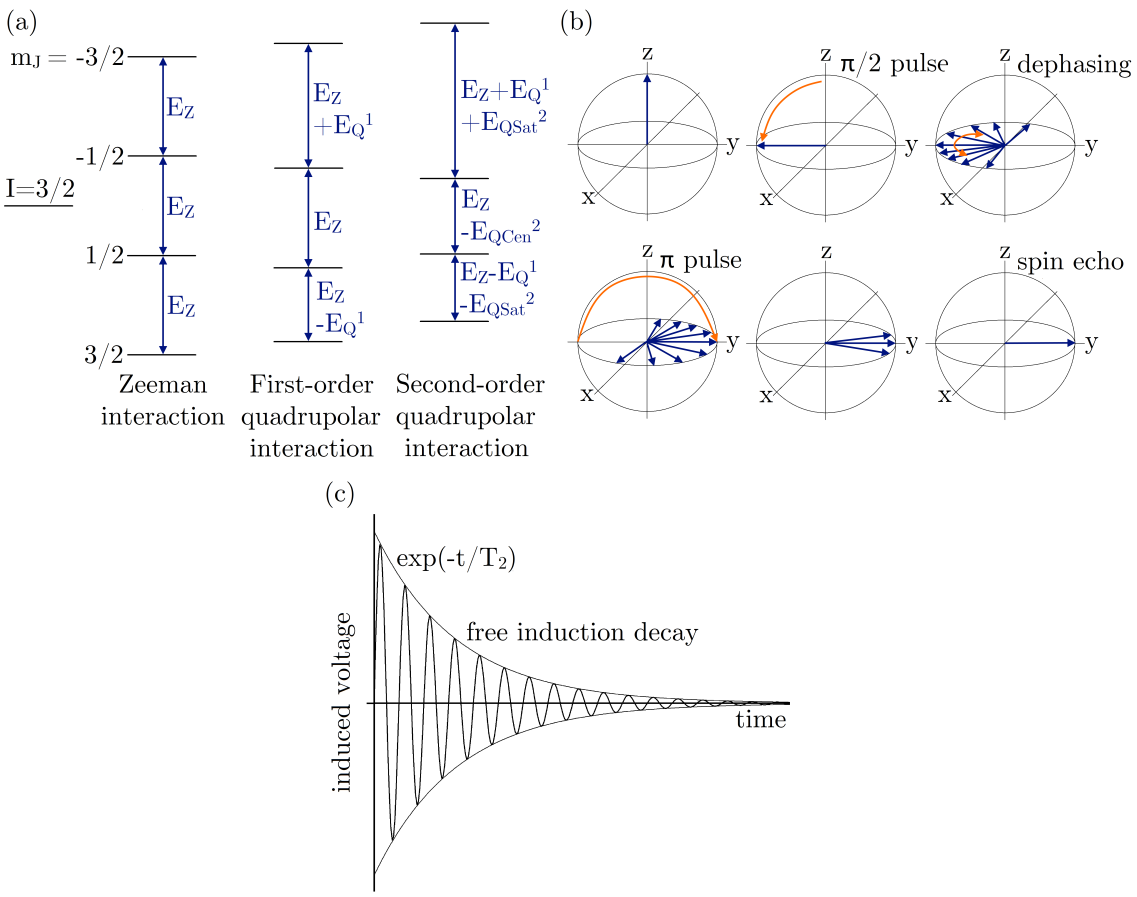

Figure 3.5.: Some NMR basics. (a) Energy level splitting in the case of a nucleus with spin $I = 3/2$. Due to first-order quadrupolar interactions, satellite lines will emerge in the NMR spectra. Second-order quadrupolar interaction affects also the central transition, leading to different shifts of the satellites with respect to the central transition. The figure is adapted from Ref. [63]. (b) Illustration of the spin echo pulse technique. The phase coherent spins are rotated into the plane perpendicular to the static magnetic field by a $\pi/2$ pulse. The nuclear spins start to dephase due to inhomogeneities of the magnetic field. After a π pulse, a spin echo can be recorded. The diagrammatic concepts are taken from Ref. [64]. (c) The precession of the net magnetization induces a signal, called the free induction decay, in a coil. The signal oscillates with the Larmor frequency and is damped due to spin-spin relaxation processes.

ing [see Fig. 3.5(b) top row]. The induced signal in the coil is called free induction decay and has the form of a damped sine wave $(\sin \omega_L t)\, e^{-t/T_2}$ [67] [see Fig. 3.5(c)]. Fourier transformation leads to the NMR spectra and the exponentially decaying envelop is governed by T_2, the spin-spin relaxation time. Direct spin-spin interactions and field inhomogeneities are responsible for the dephasing. By applying a π pulse after the $\pi/2$ pulse (spin echo pulse sequence), the spins are turned by 180 ° [64]. Thus, dephasing due to inhomogeneities of static magnetic fields is prevented and only the interactions between the spins contribute [see Fig. 3.5(b)]. The spin-spin relaxation process has no effect on the energy of the spin system. The exponential relaxation back to the Boltzmann equilibrium, that is, the restoration of the equilibrium magnetization M_0, is quantified by the decoupled spin-lattice relaxation time T_1. In the relaxation process, energy is exchanged with the surrounding lattice [64]. For a magnetic field along z, the evolution of the macroscopic magnetization (M_x, M_y, M_z) is given by the Bloch equations [68]

$$\frac{dM_x}{dt} = \gamma M_y(t) B_0 - \frac{M_x(t)}{T_2} \tag{3.2}$$

$$\frac{dM_y}{dt} = -\gamma M_x(t) B_0 - \frac{M_y(t)}{T_2} \tag{3.3}$$

$$\frac{dM_z}{dt} = \frac{M_0 - M_z(t)}{T_1}. \tag{3.4}$$

The first term in equations 3.2 and 3.3 describe the Larmor precession, and the remaining terms represent the relaxation.

The ^{31}P and ^{23}Na spin echo NMR measurements at a static magnetic field of 4.7 T were performed by Ivo Heinmaa and Raivo Stern at the National Institute of Chemical Physics and Biophysics (Tallinn, Estonia). The spectrometer `Bruker AVANCE-II` was used. For powder measurements 38 mg of the powder obtained by grinding the crystals of ten batches were filled in a Si_3N_4 rotor with a diameter of 1.8 mm. A first MAS NMR spectrum at room temperature was recorded. All other measurements were carried out on a static sample. Measurements were also performed on one single crystal. A He flow cryostat allowed measurements down to 10 K. For ^{31}P the resonance of H_3PO_4 at 80.971 MHz and for ^{23}Na the resonance of NaCl dissolved in water at 52.912 MHz were used as reference.

3.3.2. Resonant Inelastic X-ray Scattering

RIXS is a technique used to probe the electronic structure, in this work of Na_2RuO_3. To perform experiments in resonance at the $L_{2,3}$ absorption edge of $4d$ elements, an intermediate x-ray energy is required [69]. Intermediate x-ray energy RIXS (IRIXS) measurements were performed at the Ru L_3-edge of 2840 eV. IRIXS is a two-step process of absorption and spontaneous emission. An incoming photon excites a core electron (here $2p$) to an unoccupied state (here $4d$) [44]. The excited state decays

when an electron fills the core hole and consequently a photon is emitted in a random direction. The emitted photons are detected at a fixed angle. Number of the scattered photons and the energy loss between the incident and emitted photons, corresponding to the low-energy excitations, are recorded [70, 71].

The IRIXS measurements were carried out by Hakuto Suzuki under the supervision of Bernhard Keimer at Deutsches Elektronen-Synchrotron (Hamburg, Germany) at the beamline `P01` of `PETRAIII` [69]. The photons hit the 3 mm pellet of pressed Na_2RuO_3 powder and the scattered photons were detected at an angle of 90 ° with respect to the incident beam. At 300 K the spectra were recorded for the incident x-ray energies 2838.9 eV and 2839.4 eV. An additional spectrum was measured at the incident energy of 2838.9 eV at 25 K. The non-resonant spectrum of silver was used to calibrate the zero energy loss.

3.4. Cooling Techniques

With ^{4}He bath cryostats temperatures down to the boiling point of 4.2 K are directly accessible. Further cooling is realized with ^{4}He evaporation cryostats. The slope of the vapor pressure curve is given by the Clausius-Clapeyron equation

$$\frac{dp}{dT} = \frac{L}{T\Delta V} \tag{3.5}$$

with the evaporation or latent heat L. Under the assumption of an ideal gas equation 3.5 transforms into the Arrhenius form

$$p = p_0 \exp\left[-\frac{L}{R}\left(\frac{1}{T} - \frac{1}{T_0}\right)\right] \tag{3.6}$$

with $p_0 = 1013$ mbar and $T_0 = 4.2$ K for ^{4}He. When the vapor above the liquid helium is pumped, the temperature can be reduced down to 1.8 K because latent heat is needed for the evaporation of helium. Due to the lower latent heat compared to ^{4}He, ^{3}He has a higher vapor pressure [see Fig. 3.6(a)] [72]. With modest pumping, temperatures of 400 mK can be reached if ^{3}He is used as cryogenic liquid. Additionally, no disturbing superfluid films acting as possible thermal links occur. The lower millikelvin regime can be reached by adiabatic demagnetization or dilution refrigerators. Within the framework of this work, temperatures down to 40 mK were accessed with a dilution refrigerator, which uses a ^{3}He/^{4}He-mixture. Below 0.87 K a miscibility gap opens [see Fig. 3.6(b)] [73]. Close to 0 K a nearly pure ^{3}He phase and a ^{4}He-rich phase containing around 6.5% ^{3}He coexist [74, 75]. The finite solubility of ^{3}He in ^{4}He is due to a stronger ^{4}He-^{3}He bonding compared to a ^{3}He-^{3}He bonding as a consequence of the lower zero-point energy of ^{4}He, and due to a reduced Fermi energy which scales with the number density of fermions [76]. In a dilution refrigerator, ^{3}He is removed from the ^{4}He-rich phase, which leads to an osmotic pressure and to the transfer of ^{3}He across the phase boundary from the

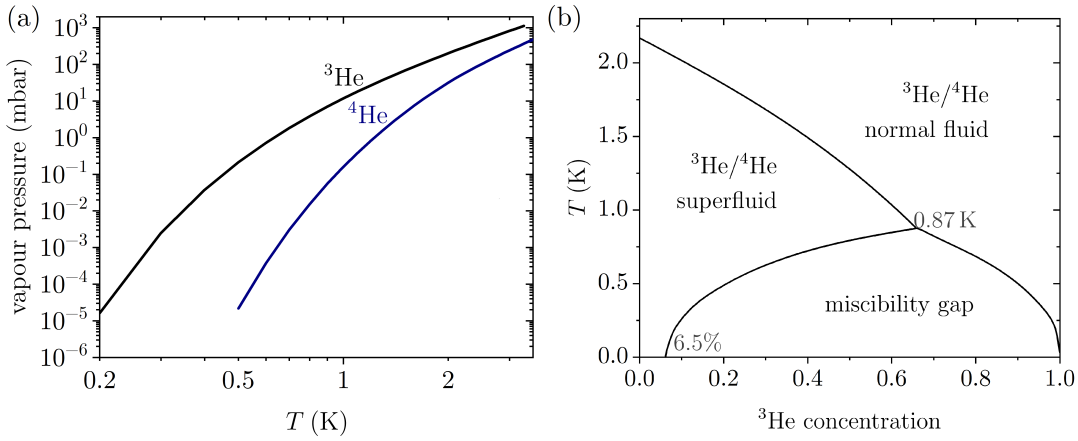

Figure 3.6.: Low-temperature properties of helium. (a) ^{3}He has a higher vapor pressure than ^{4}He. The data were taken from Ref. [72]. (b) The ^{4}He-^{3}He phase diagram shows a miscibility gap below 0.87 K. The phase diagram was adapted from Ref. [76].

nearly pure ^{3}He-phase to the ^{4}He-rich phase. In analogy to the role of the latent heat in the evaporative cooling, the required mixing enthalpy leads to further cooling of the mixture. ^{3}He is used in a circuit and is finally led back into the mixing chamber.

3.5. Magnetization

The superconducting quantum interference device (SQUID) is sensitive to changes of the magnetic flux Φ on the order of a flux quantum $\Phi_0 = h/2e = 2.0678 \cdot 10^{-15}$ Wb (1Wb = 1Tm^2). The experimental setup is sketched in Fig. 3.7. To reduce noise, the SQUID is shielded and spatially separated from the sample. The magnetic sample oscillates within a magnetic field and induces an electrical current in the superconducting pickup coils. To minimize the effect of the outside environment, the pickup coils are built as second derivative axial gradiometer. The coil set of the experiment is coupled to the SQUID into which the input coil induces a magnetic flux $\Delta\Phi$. The SQUID comprises a superconducting loop with two non-superconducting barriers, the so-called Josephson junctions (JJ). The physical phenomenon the SQUID takes advantage of is the quantization of the magnetic flux within a superconducting loop, which can only be an integer multiple n of Φ_0. The induction of the magnetic flux $\Delta\Phi$ leads to screening currents I_s within the superconducting loop to compensate that flux. Increasing the magnetic flux leads to higher screening currents until the highest screening currents are reached for $\Delta\Phi = \Phi_0/2$. Further increase of the flux leads to the reverse of the screening currents to raise Φ to the next integer value $(n+1)\,\Phi_0$. To detect the currents, two JJ are integrated into the superconducting ring. Up to a critical value I_c, the current can tunnel through the junction without

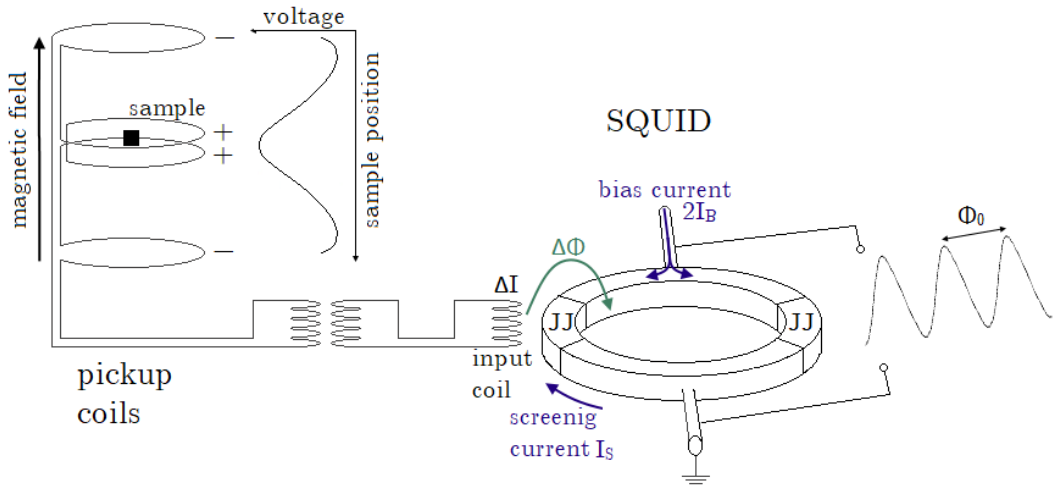

Figure 3.7.: Sketch of the setup for magnetization measurements. The oscillating sample induces a current in the pickup coils. The input coil induces the measurement signal as magnetic flux $\Delta\Phi$ in the SQUID. The SQUID is a superconducting loop with two Josephson junctions (JJ). Increase or decrease of the magnetic flux leads to a periodically changing output voltage with the period of the flux quantum Φ_0. The figure was adapted from Refs. [77] and [78].

voltage drop. The total current through one JJ is given by $I_{\text{tot}} = I_{\text{bias}} - I_{\text{s}}$ ($I_{\text{tot}} < I_{\text{c}}$), and the current through the other JJ is given by $I_{\text{tot}} = I_{\text{bias}} + I_{\text{s}}$ ($I_{\text{tot}} > I_{\text{c}}$). I_{bias} is the DC bias current at which the JJ is operated. Since one JJ is now operated above I_{c}, a voltage drop across the JJ can be measured. The voltage as a function of the external magnetic flux changes periodically with the period of Φ_0. A feedback current locks a specific $V - \Phi$ point and quantifies the external magnetic flux. The signal as a function of sample position is fitted by the software with a dipole response function under the assumption of a point source with constant magnetic moment during the measurement. [77, 78]

Measurements in DC mode determine the size of the magnetic moment in equilibrium. AC measurements allow to probe the magnetization dynamics. Therefore, an AC drive magnetic field with a given frequency and amplitude is applied in addition to the DC field and the time dependent variation of the magnetic moment is recorded. The measured AC susceptibility has a magnitude χ and a phase shift ϕ with respect to the drive signal. The real component of the susceptibility can be written as $\chi' = \chi \cos\phi$ and corresponds to the in-phase response of the magnetic moment. The imaginary component $\chi'' = \chi \sin\phi$ is the out-of-phase response related to dissipative processes.

Magnetization was measured with the `MPMS3` from Quantum Design. In the `MPMS3` magnetic fields up to 7 T can be generated. For powder measurements with the DC, VSM, or AC option, plastic capsules were filled and closed in an Ar glove box. The capsule was then clamped into a brass sample holder [see Fig. 3.8(a)]. With this setup measurements between 2 and 400 K can be performed.

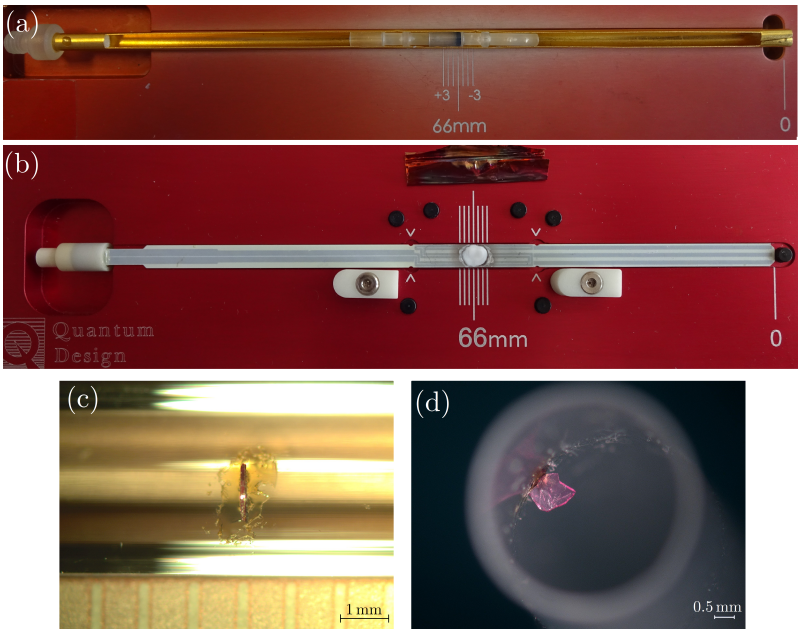

Figure 3.8.: MPMS3 sample mounting. (a) Filled powder capsule in a brass sample holder for measurements between 2 and 400 K. (b) Sample holder with cement glue for the oven option covering temperatures between 300 and 900 K. The copper foil is wrapped around the sample for thermal isolation. (c) $Na_2BaCo(PO_4)_2$ single crystal glued with varnish onto a quartz sample holder for measurements between 2 and 400 K. In this case B is parallel to c during the measurement. (d) $Na_2BaCo(PO_4)_2$ single crystal glued with varnish in a plastic straw for measurements with the ^{3}He option down to 400 mK. The magnetization is measured for B parallel to c.

For temperature dependent magnetization measurements to higher temperatures, the oven option was used. The standard setup described above is operated between 1 and 10 Torr. In contrast, the oven option requires a vacuum with pressures below 50 mTorr, which may lead to the out gassing of the sample upon heating and affects the chemical stability.

For powder measurements in DC mode up to 900 K a pellet was glued with cement onto a high-temperature sample holder [see Fig. 3.8(b)]. After the cement has dried a Cu foil was wrapped around the sample to specifically heat the sample without heating the environment. The temperature was swept up and down in loops to check for possible sample degradation during the measurement. For Na_2RuO_3 measurements up to 500 K could be performed. At higher temperatures a difference was observed between the up sweep and the down sweep indicating decomposition of the sample.

For DC-mode measurements of single crystals between 2 and 400 K a quartz sample holder was used. A small amount of GE varnish was used to attach the crystal to the sample holder. The $Na_2BaCo(PO_4)_2$ crystal in Fig. 3.8(c) was glued in such a way that the magnetic field was oriented parallel to the c axis during the measurement. For measurements with the magnetic field oriented perpendicular to the c axis, the platelet was glued planar onto the sample holder.

By using the ^{3}He inset from Quantum Design, DC-mode measurements down to 400 mK could be performed. The single crystals were glued with GE varnish into a plastic straw [see Fig. 3.8(d)]. The sample centering was performed at room temperature and again at 400 mK to account for possible changes of the center during cooling.

3.6. Heat Capacity

The heat capacity C is defined as the amount of heat dQ which is needed to increase the temperature by dT

$$C = \frac{dQ}{dT}. \tag{3.7}$$

The heat capacity is referred to as specific heat C_{mol} if normalized to the molar number.

The absorption of heat leads to excitations in the system. The total heat capacity is a sum of the heat capacity of the lattice C_{lat}, the heat capacity due to magnetic excitations C_{mag}, the heat capacity due to conduction electrons C_{e^-}, and a nuclear contribution C_{nuc}

$$C = C_{\mathrm{lat}} + C_{\mathrm{mag}} + C_{\mathrm{e}^-} + C_{\mathrm{nuc}}. \tag{3.8}$$

C_{nuc} will be briefly covered in the context of Schottky anomalies (see Subsec. 3.6.1). C_{lat} and C_{mag} will be shortly reviewed below (Subsecs. 3.6.2 and 3.6.3). C_{e^-} is not discussed any further as this contribution does not play a role in the insulating systems of this work.

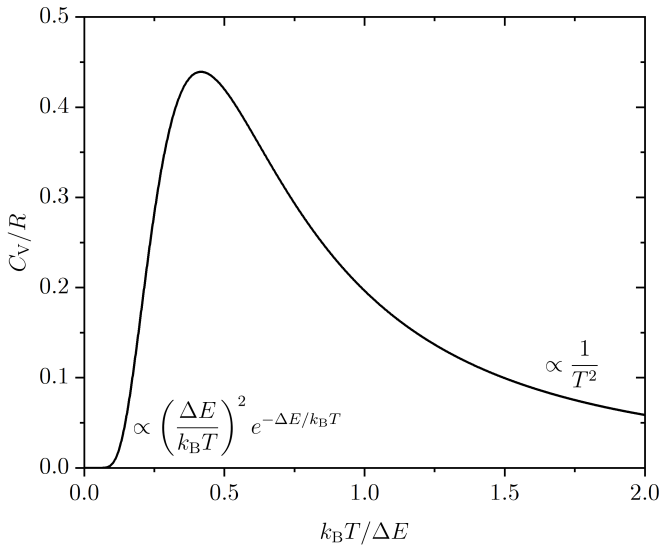

Figure 3.9.: Heat capacity of a two-level system. The Schottky anomaly shows an exponential behavior for $T \ll \Delta E/k_B$ and a power-law behavior for $T \gg \Delta E/k_B$.

Measurements of the heat capacity are usually performed at constant pressure, whereas theoretical considerations take advantage of the relation

$$C_V = \left(\frac{dQ}{dT}\right)_V = \left(\frac{dU}{dT}\right)_V, \tag{3.9}$$

which only holds for a constant volume. U is the internal energy. In contrast to gases, thanks to a small thermal expansion in solids, the distinction between C_V and C_p is not necessarily required [79].

3.6.1. Schottky Anomaly

Statistical thermodynamics postulates that the internal energy U of a system with N particles is given by

$$U = N\langle E\rangle, \tag{3.10}$$

with the expectation value for the energy of a particle $\langle E\rangle$. The expectation value is given by $\langle E\rangle = \sum_{i=1}^{n} p_i E_i$. The sum extends over all energy levels i ($1 \leq i \leq n$) and p_i is the probability to find the particle in state i. Now the simplest system that can be thermally excited, two levels separated by the energy ΔE, will be considered. In thermal equilibrium, the occupation probability is given by the Boltzmann distribution. With the assumption $E_1 = 0$

$$\langle E\rangle = \frac{\Delta E\, e^{-\Delta E/k_B T}}{1 + e^{-\Delta E/k_B T}} \tag{3.11}$$

is obtained. With the equations 3.9 to 3.11 the heat capacity can be expressed as

$$C_{\mathrm{V}} = Nk_{\mathrm{B}} \left(\frac{\Delta E}{k_{\mathrm{B}}T}\right)^2 \frac{e^{\Delta E/k_{\mathrm{B}}T}}{\left[e^{\Delta E/k_{\mathrm{B}}T}+1\right]^2}. \tag{3.12}$$

The temperature dependence of the so called Schottky anomaly is visualized in Fig. 3.9. At low temperatures ($T \ll \Delta E/k_{\mathrm{B}}$) the energy gap cannot be overcome and the thermally activated process leads to an exponential behavior of the heat capacity. At high temperatures ($T \gg \Delta E/k_{\mathrm{B}}$) the system cannot absorb more heat because the two levels are equally populated and the heat capacity vanishes following a power-law behavior.

Internal or external magnetic or electric fields can lift the degeneracies of spin states and create Schottky systems with splittings at different energy scales. The splitting of the nuclear levels of magnetic nuclei is in the radio-frequency range. This results in a Schottky anomaly at temperatures below 10 mK [80]. The $\propto 1/T^2$ tail can still be observed at higher temperatures and may lead to an upturn of the specific heat at the lowest temperatures accessed with the dilution fridge. Schottky anomalies are also observed in multilevel systems, although mathematically expressed differently [80].

3.6.2. Lattice Heat Capacity

The lattice vibrations can be treated as quantum mechanical oscillators with discrete energy levels which are separated by $\hbar\omega$. ω is the angular frequency of the oscillator. The bosonic quasiparticles, the phonons, follow the Bose-Einstein distribution $f_{\mathrm{BE}}(\omega, T)$ and hence, the thermal energy of one oscillator is given as

$$\langle E \rangle = f_{\mathrm{BE}}(\omega, T)\hbar\omega. \tag{3.13}$$

Debye introduced a density of states $D(\omega)$ into which enters the assumption of a linear dispersion relation $\omega = vk$ with the sound velocity v and the wave vector k. The expression for $D(\omega)$ can be found in solid state textbooks [81]. Equation 3.10 can now be written as

$$U = \int_0^{\omega_{\mathrm{D}}} D(\omega) f_{\mathrm{BE}}(\omega, T)\hbar\omega d\omega. \tag{3.14}$$

The normalization of the density of states yields the cut-off frequency ω_{D}. With equation 3.9 the heat capacity can be derived

$$C_{\mathrm{V}} = 9Nk_{\mathrm{B}} \left(\frac{T}{\Theta_{\mathrm{D}}}\right)^3 \int_0^{x_{\mathrm{D}}} \frac{x^4 e^x}{(e^x-1)^2} dx, \tag{3.15}$$

with $x = \hbar\omega/k_{\mathrm{B}}T$ and $x_{\mathrm{D}} = \hbar\omega_{\mathrm{D}}/k_{\mathrm{B}}T \equiv \theta/T$. θ is the Debye temperature and depends on the material. For $T \gg \theta$ the molar heat capacity becomes

$$C_{\mathrm{V,mol}} = 3R, \tag{3.16}$$

which is the classical Dulong-Petit law. For $T \ll \theta$, the specific heat follows a cubic temperature dependence

$$C_{\mathrm{V,mol}} \propto \left(\frac{T}{\Theta_{\mathrm{D}}}\right)^3. \tag{3.17}$$

3.6.3. Magnetic Heat Capacity

The precessions of coupled spins in magnetically ordered systems are collective excitations which add a magnetic contribution to the heat capacity. The quantized spin waves are also called magnons due to the close analogy to phonons. Magnons are bosonic quasiparticles and equation 3.13 holds true as well. The temperature dependence of the heat capacity depends now on the dispersion relation which enters the density of states. For small wave vectors, magnons in 3D Heisenberg antiferromagnets have the same dispersion relation $\omega \propto k$ as phonons. In analogy to the Debye law for phonons, the magnetic heat capacity shows a cubic temperature dependence, $C_{\mathrm{mag}} \propto T^3$. 2D antiferromagnets show a $C_{\mathrm{mag}} \propto T^2$ behavior and ferromagnets a $C_{\mathrm{mag}} \propto T^{3/2}$ behavior. Power-law dependencies are characteristic for gapless excitations. The magnetic heat capacity due to gapped excitations follows an exponential behavior (like the low-temperature behavior of a gapped two-level system described in Subsec. 3.6.1).

Spin wave theory does not apply for QSLs, which feature spin excitations with fractional quantum numbers. Any non-T^3 behavior may be indicative of exotic excitations, especially when no long-range order is observed. There is no generic behavior of the low-temperature heat capacity for QSLs which can again be classified into those with gapped excitations following an Arrhenius law and those with gapless excitations showing a $C_{\mathrm{mag}} \propto T^{\alpha}$ dependency. For example, spin liquids with a Fermi surface of spinons show, in analogy to Fermi metals, a linear temperature dependency ($\alpha = 1$) or even a sublinear dependency ($\alpha = 2/3$) [82], and $\alpha = 2$ for Dirac QSLs [83].

3.6.4. Entropy

As is clearly apparent from $dQ = TdS$, the entropy S can be obtained from the measured heat capacity

$$S(T) = \int_0^T \frac{C}{T'} dT'. \tag{3.18}$$

In the following, the high-temperature limit of the entropy which carries information about the ground state will be looked at. The Helmholtz free energy is given as $F = -k_{\mathrm{B}}T \ln Z$. Z is the partition function which equals the normalization constant of the Boltzmann distribution introduced with equation 3.11 and is expressed as a sum extending over all states $Z = \sum_{i=1}^{n} e^{-E_{\mathrm{i}}/(k_{\mathrm{B}}T)}$. The entropy can now be written

as

$$S = -\frac{dF}{dT} = k_\mathrm{B} \ln Z + k_\mathrm{B} T \frac{d \ln Z}{dT}$$
$$= k_\mathrm{B} \ln \sum_{i=1}^{n} e^{-E_\mathrm{i}/(k_\mathrm{B}T)} + \frac{1}{T} \frac{\sum_{i=1}^{n} E_\mathrm{i}\, e^{-E_\mathrm{i}/(k_\mathrm{B}T)}}{\sum_{i=1}^{n} e^{-E_\mathrm{i}/(k_\mathrm{B}T)}}. \tag{3.19}$$

For high temperatures, the last term $\langle E \rangle / T$ becomes vanishingly small and the high-temperature molar entropy is dominated by

$$\lim_{T \to \infty} S_\mathrm{mol} = R \ln(n). \tag{3.20}$$

Hence, the high-temperature limit of the entropy gives immediate access to the multiplicity of the ground state. Considering magnetic entropy n is given as $2J + 1$.

3.6.5. Measurement Technique

Thermal relaxation calorimetry was used to determine the heat capacity [84–86]. The simplest case is illustrated in Fig. 3.10(a). The sample with the heat capacity C_S is thermally linked to a bath with constant bath temperature T_B. The link has the thermal conductance k_SB. The sample is directly subjected to a heat pulse with power $P(t)$. This is mathematically described in analogy to an electrical circuit with

$$P(t) = k_\mathrm{SB} \Delta T + C_\mathrm{S} \frac{d\Delta T}{dt}. \tag{3.21}$$

This linear first order differential equation describes the evolution of the temperature difference ΔT between sample and bath with time. Rearranging leads to

$$\frac{P(t)}{C_\mathrm{S}} = \frac{k_\mathrm{SB}}{C_\mathrm{S}} \Delta T + \frac{d\Delta T}{dt}. \tag{3.22}$$

The heating power is well defined and indicated in Fig. 3.10(b). The sample is first heated with constant power P_0 and when the power is turned off at time t_0 the sample relaxes back to the bath temperature. With the boundary conditions that sample and bath are in thermal equilibrium at $t = 0$ and that the temperature difference is continuous at t_0, the solution is given as

$$\Delta T(t) = \begin{cases} (P_0/k_\mathrm{SB}) \left[1 - e^{-(k_\mathrm{SB}/C_\mathrm{S})\, t}\right], & 0 \leq t \leq t_0 \\ (P_0/k_\mathrm{SB}) \left(1 - e^{-(k_\mathrm{SB}/C_\mathrm{S})\, t_0}\right) \left[e^{-(k_\mathrm{SB}/C_\mathrm{S})\,(t - t_0)}\right], & t \geq t_0. \end{cases} \tag{3.23}$$

During heating ($0 \leq t \leq t_0$) the rising exponential and during cooling ($t > t_0$) the falling exponential are governed by C_S and k_SB. The two quantities can be combined in the time constant $\tau = C_\mathrm{S}/k_\mathrm{SB}$ leading to

$$\Delta T(t) = \begin{cases} (\tau P_0/C_\mathrm{S}) \left[1 - e^{-t/\tau}\right], & 0 \leq t \leq t_0 \\ (\tau P_0/C_\mathrm{S}) \left(1 - e^{t_0/\tau}\right) \left[e^{-(t - t_0)/\tau}\right], & t \geq t_0. \end{cases} \tag{3.24}$$

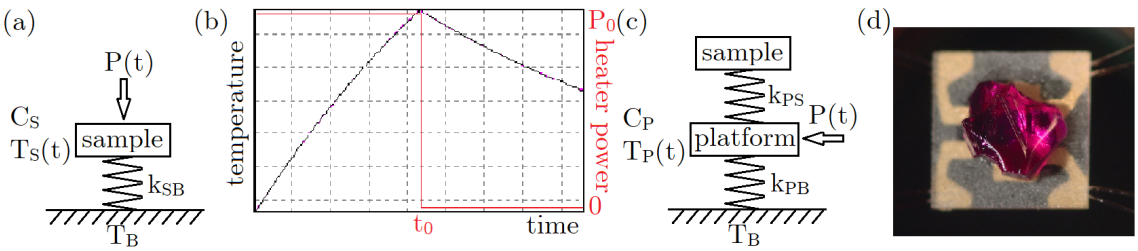

Figure 3.10.: Heat capacity measurements by the thermal relaxation method. (a) In the simple relaxation model the sample is thermally linked to a bath with constant temperature. The sample is then subjected to a heat pulse $P(t)$. The response is given in (b) During the heating the temperature difference between sample and bath grows exponentially. When the heater power is turned off the temperature difference decreases exponentially. The figure was adapted from Ref. [84]. (c) In the experiment the sample is attached to a platform containing heater and thermometer. The second thermal link between platform and sample is considered in the two-tau model. (d) $Na_2BaCo(PO_4)_2$ single crystal attached with N-grease to the platform.

The time constant is determined experimentally by fitting the exemplary data shown in Fig. 3.10(b) and with known k_{SB} the heat capacity is accessible.

In the experiment it is impracticable to link every single sample directly to a bath and to attach heater and thermometer. Instead, the sample is heated indirectly by placing it onto a platform. The schematic in Fig. 3.10(a) is augmented to Fig. 3.10(c). The platform is directly linked with wires to the bath and contains the heater and thermometer. To ensure a good thermal contact between sample and platform, the sample is attached with vacuum grease suited for low temperatures (N grease). A $Na_2BaCo(PO_4)_2$ single crystal attached to the platform for ^{4}He measurements is shown in Fig. 3.10(d). The additional link k_{PS} between platform and sample is taken into account in the 2τ model. The temperature difference over time is now described with two exponential functions, one governed by the relaxation time between platform and bath τ_{PB} and one governed by the simultaneous relaxation time between platform and sample τ_{PS}:

$$\Delta T(t) = -\left(A_1 e^{-t/\tau_{PB}} + A_2 e^{-t/\tau_{PS}}\right). \tag{3.25}$$

A_1 and A_2 are constants. τ_{PS} is usually much faster which leads to a small drop in the raw data when the heater is turned off. If the sample is coupled ideally to the platform, the model reduces to the simple τ model. For a further description of the 2τ model the reader is referred to Ref. [85].

From the measured total heat capacity, the contribution of platform and grease has to be subtracted to obtain the heat capacity of the sample. Therefore, an addenda measurement of platform and grease was conducted at the same temperatures and magnetic fields at which the later measurements were performed.

The ^{4}He and ^{3}He heat capacity measurements were performed in the PPMS from Quantum Design. In the case of powder measurements a pellet was mounted on the platform. For a good internal thermal contact the pellet should be tempered. The sample coupling was always larger than 90% and the data could always be described with the 2τ model. In the case of $Na_2SrCo(PO_4)_2$ single crystals, ^{4}He measurements were not possible due to sample masses well below 1 mg. Mounting several crystals onto the platform could not help solving the problem since too many different time constants did not allow for a fitting of the raw data. $Na_2SrCo(PO_4)_2$ single crystals could only be analyzed with the ^{3}He option because of the smaller background of the setup.

3.6.6. Heat Capacity Measurements in the Dilution Refrigerator

For $Na_2BaCo(PO_4)_2$ heat capacity measurements were performed in a dilution refrigerator by Noah Winterhalter-Stocker. Like in the PPMS the heat capacity was measured with the relaxation method. The principle of the relaxation method was already described in Subsec. 3.6.5, albeit the setup in the dilution refrigerator is slightly different. The sample is mounted onto a sapphire platform, which is due to the suspension design thermally decoupled from the environment. The resistive heater is attached to the platform below the sample. In contrast to the measurement in the PPMS, the thermal link to the bath and the RuO_2 thermometer are directly attached on top of the sample. This has the advantage that an additional thermal link between platform and sample is avoided and the temperature change of the sample can be described with a single exponential. A deviation from this behavior can occur if the nuclear heat capacity of the sample and platform contributes to the measured heat capacity. In this case, the data cannot be described with the simple model and the analysis may become challenging. For $Na_2BaCo(PO_4)_2$ no nuclear contribution was seen in the relaxation curves.

In a first step, the heater was fixed with epoxy to the platform. A $Na_2BaCo(PO_4)_2$ single crystal around 0.5 mg was mounted in a planar manner with GE varnish on to the platform. Using silver paste and GE varnish the thermal link and the thermometer, respectively, were glued onto the sample. The heat capacities $C(T)$ and $C(B)$ were recorded in zero magnetic field and for magnetic fields up to 2 T for B perpendicular to c and B parallel to c. The lowest temperature reached was 50 mK.

4. Results and Discussion

4.1. Na_2RuO_3

SOC is a key factor that leads to novel exotic states in $4d$ and $5d$ transition metal systems. Widely studied are d^5 systems with spin-orbit entangled $J = 1/2$ pseudospins on a honeycomb lattice with edge-shared octahedra in the context of Kitaev physics. The here presented Na_2RuO_3 has a honeycomb lattice with edge-shared octahedra but with a $4d^4$ configuration the system should not be confused with a Kitaev material. The ground state is still debated in the literature and Na_2RuO_3 is reported as insulating antiferromagnet, semiconducting antiferromagnet and correlated electron metal. In general, the ground state of $4d^4$ Ru compounds is under discussion. The magnetism in Ca_2RuO_4 was first explained by tetragonal crystal-field splitting and Hund's coupling leading to a $S = 1$ ground state [87–89]. Later it was found that the orbital momenta are unquenched and SOC seems to have an important role in ruthenates and can lead in an interplay with Hund's coupling and crystal-field splitting to exotic excitonic magnetism [90]. Experimental findings hint towards the scenario of J multiplets in Ca_2RuO_4 with the lowest energy level $J = 0$ [43, 44, 91]. If the superexchange is comparable in size to the singlet-triplet splitting the so called triplon condensation causes the magnetism in the system. RIXS spectroscopy on single crystals of K_2RuCl_6 with an undistorted cubic crystal field revealed the SOC driven non-magnetic $J = 0$ singlet state [92]. Ref. [92] suggests the J multiplet scenario as generic basis in $4d^4$ Ru compounds.

Here, first structural features will be discussed before the analysis of the heat capacity, magnetization and IRIXS data is addressed with regard to characteristics of $J = 0$ physics. The XRPD pattern shows partly reduced peak intensities and asymmetric peak broadening which originate from the faulted stacking of the honeycomb slabs. The amount of stacking faults in the structure was quantified by `DIFFaX` simulations of the XRPD pattern. In both the heat capacity and magnetization data down to 2 K no phase transitions are observed. Magnetization measurements up to 500 K show a deviation from the Curie-Weiss behaviour and signatures of Van-Vleck magnetism point towards a non-magnetic $J = 0$ ground state. This finding is supported by low-temperature RIXS measurements. The spectrum reveals four transitions at around 70, 350, 780, and 1000 meV. The lowest excitation energy fits perfect to the SOC energy scale for Ru^{4+}-compounds.

4.1.1. Crystal Structure and Stacking Faults

The crystal structure is characterized by a honeycomb lattice formed by $Ru^{4+}O_6$ octahedra in the *ab* plane [see Fig.4.1(a)]. The octahedra are connected via the edges. The center of the honeycomb cells are each occupied by one Na^+ ion. In addition, the Na^+ ions serve as non-magnetic spacer ions and separate the honeycomb slabs which are stacked along the crystallographic *c* direction [see Fig.4.1(b)]. The monoclinic unit cell with the symmetry $C2/c$ (no. 15) was already described in the literature [47]. Simulation on the basis of this symmetry yields the PXRD pattern depicted in Fig. 4.2(a) in black. For comparison with the experimental results, the measured XRPD pattern is superimposed in red. The simulation and experimental data share common features but show also severe differences in the form of reduced peak intensities and asymmetric peak broadening in the measured data. Particularly striking is the broad asymmetric feature at around 20 °. This feature is characteristic for stacking faults and is also referred to as triangular Warren-type peak originally investigated in the context of faulted stacking in graphite [94]. Also for layered honeycomb compounds, e.g. Li_2IrO_3, Li_2PtO_3, and Li_2MnO_3, the Warren peak is commonly observed in the diffraction data [95–97].

The effect of the stacking faults on the XRPD pattern depends on the proportion of stacking faults in the structure. To simulate the XRPD pattern under the assumption of stacking faults, a faulted stacking vector has to be chosen first. In

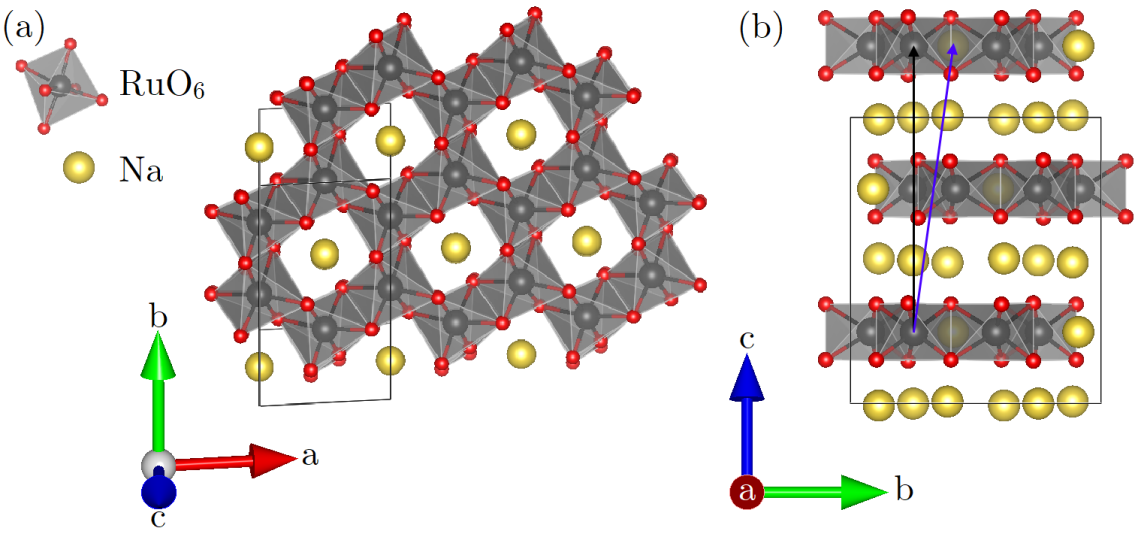

Figure 4.1.: Crystal structure of Na_2RuO_3. (a) The honeycomb layers in the *ab* plane are formed by RuO_6 octahedra. Na^+ ions occupy the centers of the honeycomb cells. The Na^+ ions which separate the honeycomb layers are omitted for clarity. (b) The honeycomb layers and Na^+ layers are alternately stacked along the *c* axis. The ideal stacking along (001) is indicated with the black arrow. The faulted stacking vector (0.5 0.172 1) drawn in blue was used for the simulation of the XRPD patterns. The visualization program `VESTA` was used to depict the crystal structure [93].

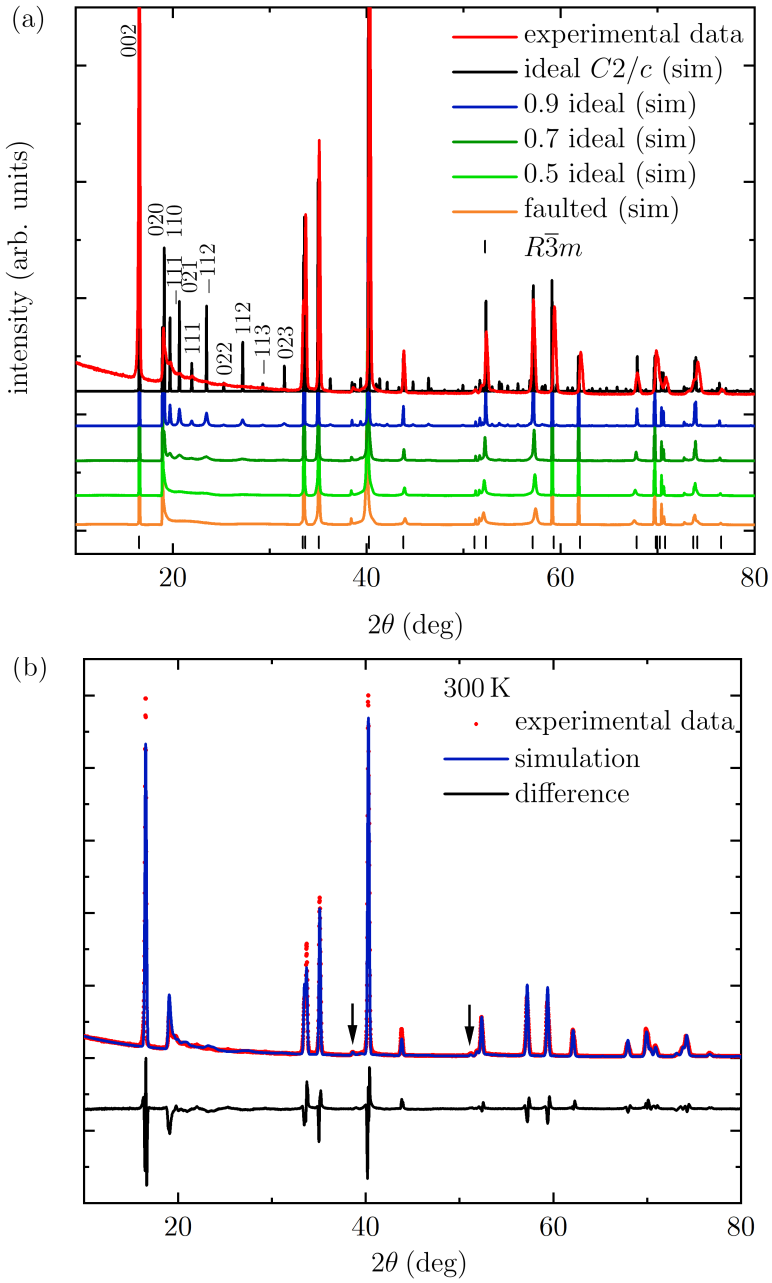

Figure 4.2.: Comparison of the measured XRPD pattern of Na_2RuO_3 and the simulation of the XRPD pattern under the assumption of stacking faults. (a) Experimental data and simulated PXRD pattern for the ideal case without stacking faults and for different proportions of stacking faults. The peak positions for the hexagonal space group are added as gray ticks. (b) The simulated PXRD pattern for Na_2RuO_3 with an amount of stacking faults of 30% is combined with the refined profile parameters and compared to the experimental data.

the ideal case the (001) stacking vector stacks the honeycomb layers along c. This is indicated in Fig. 4.1(b) with the black arrow. The faulted vector is depicted as blue arrow and shifts one Ru ion onto a Na ion in the center of a honeycomb cell. This corresponds to a (0.5 0.172 1) stacking vector in the monoclinic coordinate system. Other descriptions of the stacking faults are possible but a good match of simulation and experiment in the end justifies the choice. Also multiple stacking vectors are conceivable but simulating the XRPD pattern with two different stacking vectors did not lead to a better description of the experimental data. In the following, the results are given for the (0.5 0.172 1) stacking vector.

Before the results are presented it should be noted that a detailed description of the simulation procedure with the `DIFFaX` routine is given in Ref. [59]. As already mentioned in Sec. 3.2 a coordinate transformation from the monoclinic into a Cartesian coordinate system is necessary since the program requires the c axis orthogonal to the ab plane ($\alpha, \beta = 90\,^\circ$, no restrictions for γ). In a first consistency check the diffraction pattern was simulated for the structure without stacking faults using the ideal stacking vector only. Thus, the expected diffraction pattern for the space group $C2/c$ was recreated. Next, the effect of different degrees of disorder on the diffraction pattern was investigated by setting different ratios of the faulted and ideal stacking vectors. To introduce for example 10% of stacking faults one out of ten times the unit cells were stacked in a faulted manner on top of each other. Note that in this work the unit cell containing two honeycomb layers was used. Care should be taken when comparing ratios of stacking faults because values found in the literature are sometimes referred to stacking of unit cells containing only one honeycomb layer.

The results for different quantities of stacking faults are illustrated in Fig 4.2(a). Already small amounts of stacking faults of 10% are noticeable, especially in the region between 20 and 30 $^\circ$ in the form of significant peak broadening and intensity reduction. The effects become stronger if the degree of disorder increases. For 30% of faulted stacking the smeared out peaks merge into the Warren-type peak. If the unit cells are stacked in a completely faulted manner, a featureless Warren-type peak is observed [see orange pattern in Fig. 4.2(a)].

The easiest way to determine the amount of stacking faults in the compound from the diffraction pattern is to use two structural models in the Rietveld refinement. The space group $C2/c$ describes the ideal case and the second space group $R\bar{3}m$ (no. 166) accounts for the complete stacking disorder [47, 51]. The peak positions in the second case are given as gray ticks in Fig. 4.2. The hexagonal space group describes a structure with a random distribution of the Ru and Na ions in the honeycomb layers. This is only a crude approximation of the real situation. There is no site mixing in Na_2RuO_3. The average structure recorded by the x rays is not truly hexagonal and monoclinic distortions are sill present. The degree of disorder is gained from the phase fraction. Drawback of this method is that the Warren-type peak cannot be interpreted and many peak intensities and the asymmetric broadening cannot be modeled correctly.

A more straightforward estimate of the stacking faults compared to the two-phase

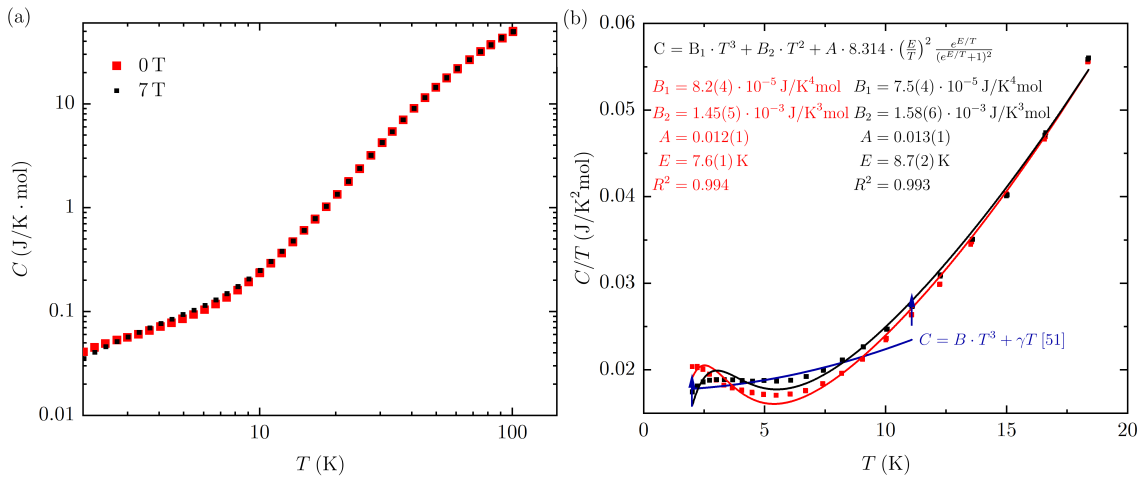

Figure 4.3.: Heat capacity of Na_2RuO_3. (a) The heat capacity in zero field and at 7 T does not show any phase transition down to 2 K. (b) Low-temperature heat capacity divided by temperature. The data can be fitted with a phonon contribution and a Schottky anomaly stemming from magnetic impurities.

approach is possible with the concept of the stacking vector. Fig. 4.2(b) shows the simulation to which the refined profile parameters were added. The data are well described assuming 30% of stacking faults. Besides a more accurate evaluation of the amount of stacking faults, this method can distinguish if low-intensity peaks stem from stacking faults or impurity phases. For example, the peaks marked with arrows in Fig. 4.2(b) can be clearly assigned to stacking faults and impurities can be excluded. However, there is still room for optimization because refining and simulating simultaneously was not possible and the amount of stacking faults had to be adapted manually.

4.1.2. Thermodynamic Properties

No phase transition can be observed in the heat capacity. Fig. 4.3(a) shows the heat capacity between 2 and 100 K. The low-temperature part of the heat capacity divided by temperature is given in Fig. 4.3(b). A sizeable residual value of C/T is present at 2 K and Ref. [51] suggests an electronic contribution to the heat capacity $C_{\mathrm{el}} = \gamma T$ with the electronic coefficient γ. However, the fit function used by Ref. [51] $C = B \cdot T^3 + \gamma T$ with the electronic contribution added to the phonon contribution with constant B fails to describe the data. The fit was added in blue to Fig. 4.3(b). The data can be described by

$$C = B_1 \cdot T^3 + B_2 \cdot T^2 + A \cdot 8.314 \cdot \left(\frac{E}{T}\right)^2 \frac{e^{E/T}}{(e^{E/T}+1)^2}. \tag{4.1}$$

The first two terms are phonon contributions. The first term is the known Debye T^3 law. The prefactor is two orders of magnitude smaller than the prefactor of the

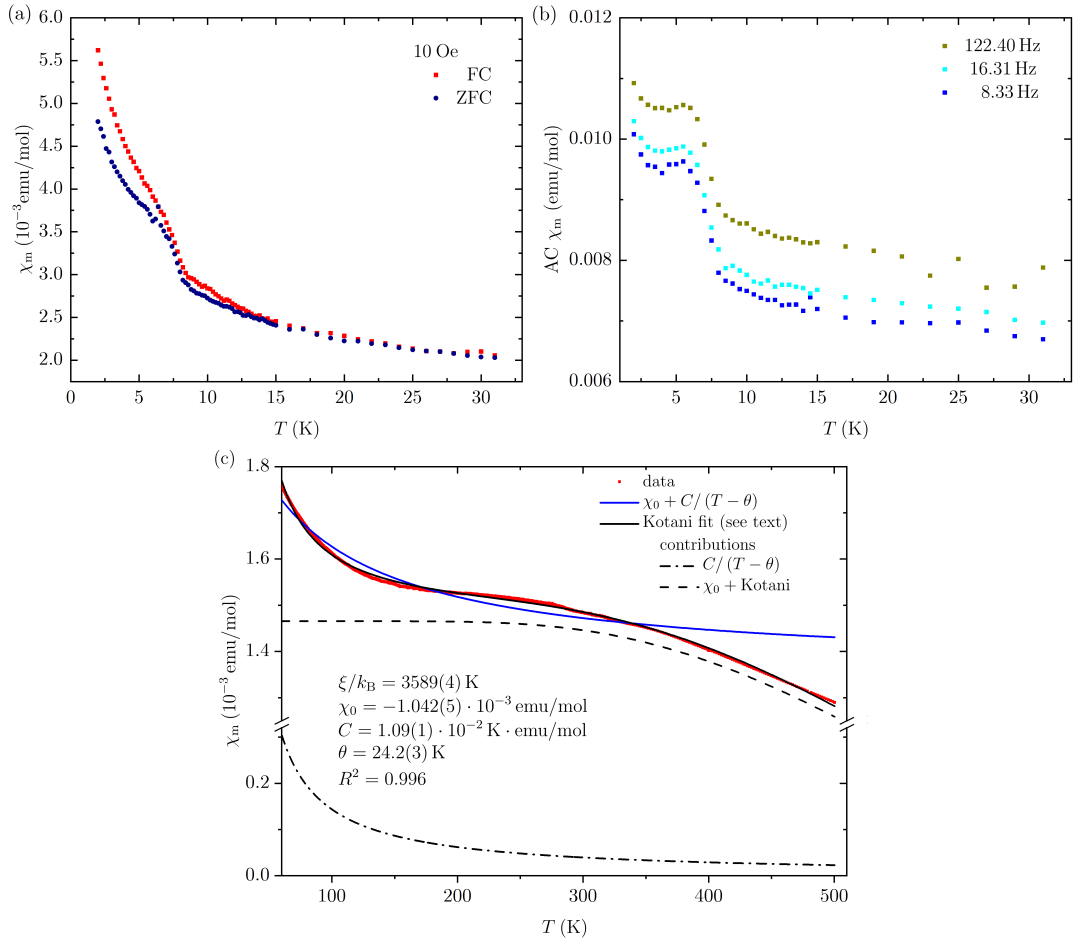

Figure 4.4.: The susceptibility of Na_2RuO_3 shows no phase transition. (a) The FC and ZFC susceptibility measured at 10 Oe differ slightly below 15 K and show a sharp upturn below 8 K, which can be traced back to magnetic impurities. (b) Ferromagnetic impurities cause also the small peak in the AC susceptibility. The absence of frequency dependent shifts excludes a spin glass. (c) The susceptibility measured at 7 T shows a plateau and a clear deviation from the Curie-Weiss behavior. The data can be fitted accurately by adding a Kotani contribution to the Curie-Weiss fit. The individual contributions are indicated with dashed lines. The fit is discussed in the text.

T^2 term. The phonon heat capacity of two dimensional crystals follows a T^2 behavior. The stacking faults in Na_2RuO_3 possibly break the crystallinity in c direction, which is mirrored in the T^2 behavior of the heat capacity. Additionally, a Schottky contribution was added to account for an impurity contribution. The impurity is non magnetic since the Schottky anomaly is nearly independent of the magnetic field with $E = 7.6(1)$ and $8.7(2)$ K for 0 and 7 T, respectively. From the entropy contained in the Schottky anomaly the amount of paramagnetic spins is estimated to be around 1%. Note, however, that anomalies in the heat capacity or in the thermal expansion can also be led back to stacking faults [98–100].

Also the magnetic susceptibility does not reveal any phase transition down to 2 K. The abrupt increase of the magnetic susceptibility below 8 K [see Fig. 4.4(a)] is typical of a tiny ferromagnetic impurity contribution. The FC and ZFC susceptibility at 10 Oe shown in Fig. 4.4(a) starts to differ slightly below 15 K. This difference of the FC and ZFC data is probably related to the ferromagnetic contribution and to exclude that the difference is caused by glassy dynamics AC susceptibility measurements were performed. A small cusp is visible in the AC susceptibility shown in Fig.4.4(b) at the same temperature at which the sharp increase of the FC and ZFC susceptibility was observed. In case of a spin glass the cusp would shift to higher temperatures for higher frequencies. The AC magnetic susceptibility does not show any frequency dependence and spin glass physics can be ruled out. Instead the weak magnetism is caused by ferromagnetic impurities.

The susceptibility at 7 T up to 500 K is given in Fig. 4.4(c) and deviates from a Curie-Weiss behavior. The data are badly described by the Curie-Weiss fit shown in blue. Striking is the plateau which was already reported for other d^4 compounds [92, 101] and is characteristic of the Van Vleck contribution to the susceptibility. The Curie tail at low temperatures is assigned to paramagnetic impurities. The fit function used to describe the data

$$\chi_\mathrm{m} = \chi_0 + \frac{C}{T-\theta} + \frac{N_\mathrm{A}\mu_0\mu_\mathrm{B}^2}{3k_\mathrm{B}T}\,\frac{3\left[24 + \left(\frac{\xi}{2k_\mathrm{B}T} - 9\right)e^{-\xi/(2k_\mathrm{B}T)} + \left(\frac{5\xi}{2k_\mathrm{B}T} - 15\right)e^{-3\xi/(2k_\mathrm{B}T)}\right]}{\frac{\xi}{k_\mathrm{B}T}\left(1 + 3e^{-\xi/(2k_\mathrm{B}T)} + 5e^{-3\xi/(2k_\mathrm{B}T)}\right)} \tag{4.2}$$

consists of a Curie-Weiss part which accounts for the Curie tail and the Kotani part [15]. Concerning the Kotani part the SOC constant is the only free parameter. It is noted in passing, that the constant refers to the single-electron SOC strength ξ. In the literature also $\lambda = \xi/2$ can be found but the notation is not used uniformly. As described in Subsec. 2.5.1 Kotani calculated the Van Vleck susceptibility of 6-fold coordinated complex d ions. In contrast to rare-earth compounds with the SOC as dominating interaction, the electrostatic energy due to the surrounding ligands can not be neglected for transition metal compounds. Kotani included the corresponding energy in the Hamiltonian assuming a crystal field with cubic symmetry. Moreover, only the low-spin configurations are considered.

The Kotani fit given in equation 4.2 describes the bending. Although the Curie paramagnetism is caused by impurities, it dominates over the weaker Van Vleck paramagnetism especially at low temperatures and the fit parameters strongly de-

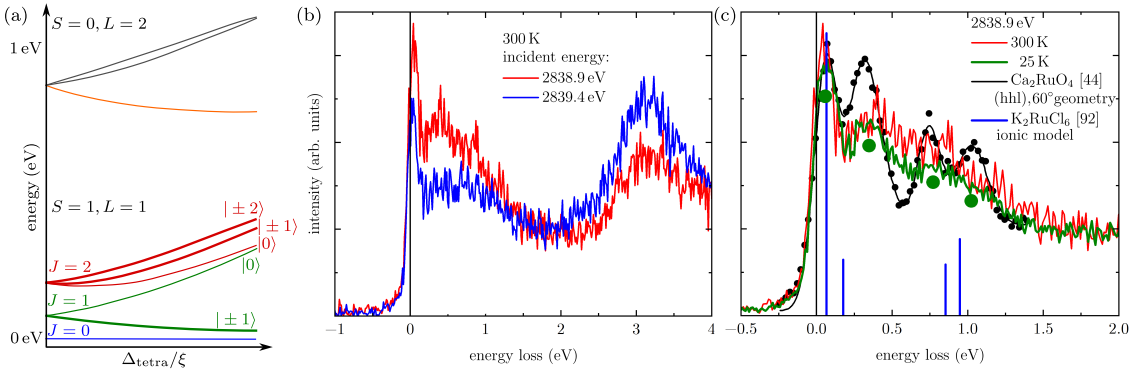

Figure 4.5.: Excitations in Na_2RuO_3. (a) The energies of the t_{2g}^4 multiplet levels as for the case of Ca_2RuO_4 depend on the strength of the tetragonal crystal field Δ_{tetra} and the SOC constant ξ. Hund's coupling leads to the separation of the levels with different S and L. The scheme was redrawn from Ref. [44]. (b) Two IRIXS spectra were recorded at 300 K for two different incident x-ray energies 2838.9 eV and 2839.4 eV. At the lower energy 2838.9 eV, the excitations below 1 eV are better resolved. (c) Beside the IRIXS spectrum at 300 K, a further spectrum was recorded at 25 K. Four features, marked with green circles, can thus be observed at 70, 350, 780, and 1000 meV. The Ca_2RuO_4 single crystal data collected with an incident angle of the photons of 60 ° from Ref. [44] are superimposed and the peak positions from ionic model calculations for K_2RuCl_6 from Ref. [92] are indicated for comparison. Measurements by Hakuto Suzuki and Bernhard Keimer.

pend on the chosen temperature window. The parameters obtained by fitting the data between 57 and 500 K are given in Fig. 4.4(c). The Curie contribution is overestimated which might be due to the hardly separable contributions. Also the SOC constant of $\xi/k_{\text{B}} = 3589(4)\,K$ is nearly two times higher than 2014 K, the highest value reported in the literature for Ru^{4+} [102]. This makes clear that Kotani's theory does not include every aspect present in this material, which will be further discussed in Subsec. 4.1.4. The SOC energy ξ ranges between 120 and 170 meV (1400 and 2000 K) for Ru^{4+} compounds [44, 102–104] and possible excitations on this scale should be detectable with IRIXS.

4.1.3. Resonant Inelastic X-ray Scattering

At 300 K two IRIXS spectra were recorded at the L_3 absorption edge of Ru. At 2838.9 and 2839.4 eV $2p \rightarrow 4d$ transitions are excited. Three features are observable in the spectrum shown in Fig. 4.5(b). The excitations below 1 eV can be assigned to intra $t_{2\text{g}}$ excitations. The level scheme up to around 1 eV is sketched in Fig. 4.5(a). The scheme was originally published for Ca_2RuO_4 [44] to which Na_2RuO_3 will be compared at the end of this subsection and in Subsec. 4.1.4. The excitations above 3 eV correspond to $t_{2\text{g}} \rightarrow e_{\text{g}}$ transitions. At the higher incident energy (2839.4 eV) the resolution of the low energy excitations is reduced, whereas the feature above 3 eV shows a higher intensity. Since the focus is on the lowest energy excitations, a

third spectrum was collected at the lower incident energy of 2838.9 eV at 25 K [see Fig. 4.5(c)]. Three transitions at 70, 350, and 780 meV can thus be resolved and are indicated with green circles. An additional weak and broad peak can be identified at around 1 eV.

In Fig. 4.5(c) the collected IRIXS spectra are compared to the IRIXS data of Ca_2RuO_4 and K_2RuCl_6, two other $4d^4$ Ru^{4+} compounds [44, 92]. In the case of Ca_2RuO_4 the spectrum recorded at the incident energy of 2838.5 eV at 12 K is superimposed in dark blue on the data in Fig. 4.5(c). The spectra show strong resemblance concerning the excitation energies. Ca_2RuO_4 as well shows four transitions up to 1 eV. The energies of 50, 320, 750, and 1000 meV in Ca_2RuO_4 are very similar to those of Na_2RuO_3 at around 70, 350, 780, and 1000 meV. The spectrum of K_2RuCl_6 shows very sharp peaks and the spectra are more difficult to compare. Only the peak positions are added to Fig. 4.5(c). In K_2RuCl_6 two excitations were recorded below 0.5 eV as well and the lowest energy excitation at 66 meV coincides with the lowest energy excitation in Na_2RuO_3. The comparison to Ca_2RuO_4 and K_2RuCl_6 will be further discussed in Subsec. 4.1.4 in the context of $J = 0$ magnetism.

4.1.4. Discussion

It is published that Na_2RuO_3 crystallizes in the Li_2SnO_3 structure type with the symmetry $C2/c$ [47]. Yet, it should be noted that the peak broadening and reduction of the intensities due to the stacking faults observed in the XRPD pattern do not allow for the determination of the space group symmetry unambiguously. Both symmetry restrictions and stacking faults can lead to the absence of peaks and the intensity of the peaks is affected by both the atomic positions and stacking faults. For Na_2IrO_3 the space group was initially reported to be $C2/c$ but was later corrected to $C2/m$ [105]. In the $C2/m$ structure the honeycomb layers are stacked along the monoclinic c axis. In contrast, in the $C2/c$ structure the honeycomb lattice in the adjacent layer is displaced by a few percent of the unit cell parameters which makes a description with a doubled unit cell volume necessary. The absence of superstructure peaks in the well-ordered single crystal diffraction pattern ruled out the $C2/c$ scenario in Na_2IrO_3. For Na_2RuO_3 samples with less stacking faults would be necessary to determine the preferred stacking sequence, i.e. to distinguish between the two space groups $C2/c$ and $C2/m$. Here, the more general space group $C2/c$ was used as starting point for the simulation.

All samples prepared in this work had a comparable amount of stacking faults. Controlling this amount during synthesis is, therefore, not easy. Since the same two-step synthesis used here is commonly reported as synthesis method in the literature the samples should have similar amounts of stacking faults. The simulation of the XRPD pattern shows that small changes in the amount of stacking faults is directly visible and the resemblances of the rather featureless asymmetric peak indicates similar amounts of stacking faults in the samples. Still, sample dependencies can not be ruled out.

In the literature Na_2RuO_3 is described as insulating antiferromagnet [49], semi-

conducting antiferromagnet [50] and by contrast as correlated metal [51]. The single crystals in Ref. [49] were claimed to be Na_2RuO_3 single crystals but show all properties of Na_3RuO_4. This can be lead back to the easy formation of Na_3RuO_4 as by-product during the synthesis of Na_2RuO_3. Ref. [50] partly relies on those results and neglects SOC in the calculations. However, SOC seems to be a key factor in $4d^4$ Ru compounds.

Here, the experimental results are discussed in the context of a non-magnetic $J = 0$ ground state. The energy level scheme and a short introduction into excitonic magnetism is given in Figs. 2.4 and 4.5(a) and Subsec. 2.7.4.

The correlated-metal scenario of Ref. [51] implies that the magnetic susceptibility of Na_2RuO_3 should be temperature independent. The upturn at low temperatures is possibly caused by impurities. At higher temperatures the susceptibility shows a strong temperature dependence in the form of a downward bending that the temperature independent Pauli paramagnetism fails to explain. The susceptibility keeps decreasing to at least 500 K, at odds with the correlated-metal scenario. Instead, an alternative scenario of J=0 magnetism is considered. Level excitations from the spin-orbit entangled $J = 0$ ground state to the higher lying $J = 1$ and $J = 2$ levels captured by the Kotani fit explain the main features of the curve which were also observed for other $J = 0$ systems [92]. In contrast to Ref. [51] the heat capacity shows no linear γT contribution and hence no signatures of itinerant electrons in the system can be seen. This fits to the insulating behavior in Ref. [51], which contradicts the hypothesis of a correlated electron metal.

Possible excitations from the ground state to higher lying J levels can be probed spectroscopically. Reported inelastic neutron scattering results do not show excited states below 150 meV [51]. IRIXS allowed to extend the energy range to 4 eV and four excitations could be detected at around 70, 350, 780, and 1000 meV. It is not clear why the lowest energy excitation was not detected by inelastic neutron scattering. The spectrum of Na_2RuO_3 strongly resembles that of Ca_2RuO_4 and the energy of the first transition coincides with that of K_2RuCl_6 [see Fig. 4.5(c)]. It was found that the two lowest energy excitations in Ca_2RuO_4 and K_2RuCl_6 are excitations from $J = 0$ to $J = 1$ or $J = 2$. In analogy, the excitation in Na_2RuO_3 at 70 meV can be assigned to the $J = 0$ to $J = 1$ transition and the excitation at 350 meV can be assigned to the $J = 0$ to $J = 2$ transition. As illustrated in Fig. 4.5(a) the Hund's coupling can be surpassed at higher energies and spin-state transitions explain the excitations at higher energies. Besides SOC and Hund's coupling, the strength of the tetragonal crystal field Δ_{tetra} plays an important role and lifts the degeneracy of the J levels [see Fig. 4.5(a)]. This can be observed in a broadening of the peaks. The peaks in the case of K_2RuCl_6 with ideal octahedra are rather sharp. The different environment of the Ru^{4+} ions can explain the broader peaks, especially the second one, in Na_2RuO_3 compared to Ca_2RuO_4. The monoclinic Na_2RuO_3 shows distortions of the RuO_6 octahedra beyond orthorhombic and features two different Ru sites, whereas the orthorhombic Ca_2RuO_4 has only one Ru site. Besides, the measurements were not performed on single crystals as for Ca_2RuO_4 and K_2RuCl_6 but on powder samples, which can cause a broadening of the peaks too. Moreover,

sample degradation during the measurement can additionally contribute to the peak broadening.

The fit of the Kotani model to the susceptibility data shows that the behavior can be quantitatively explained with excitations into higher J levels. The difference of the RIXS peak positions of Na_2RuO_3 to those of K_2RuCl_6 with an ideal octahedral environment of the Ru ions mirrors the deviation of the RuO_6 octahedra from the octahedral symmetry in Na_2RuO_3. However, trigonal crystal field splitting is not considered in the Kotani model, which explains the inconclusive fit parameters.

4.2. Na_3RuO_4

After the presentation of a Ru^{4+} compound the focus is now on Na_3RuO_4 with a by one increased oxidation state of the Ru ion. Initially, the synthesis of the compound was not intended but Na_3RuO_4 formed easily as by-product and its investigation allowed to clarify the situtation concerning the miscategorization of Na_3RuO_4 which was published as Na_2RuO_3 in Ref. [49]. The crystal structure sets the basis for various actors like frustration, low-dimensionality, and Ru-O covalency. In the layered Na_3RuO_4 two isosceles Ru triangles form a tetramer and the tetramers form again a triangular lattice (see Fig. 4.6). The Ru ions carry a spin of 3/2 and hence, a triangular spin lattice is formed on two different length scales. The magnetic susceptibility shows that long-range antiferromagnetic order forms at 30 K. The heat capacity reveals a second transition at 26 K. To explore the nature of the two phase transitions and to study the influence of the frustration on the magnetic ordering, temperature dependent NPD measurements were performed. The magnetic moments of Ru1 and Ru2 are 2.23(3) and 3.04(3) μ_B, respectively. The tetramers are nearly antiferromagnetically coupled but the magnetic structure is incommensurately modulated on the secondary triangular lattice with the propagation vector $\vec{k} = (0.242, 0, 0.312)$. The incommensurability is caused by frustration between the tetramers, which is confirmed by density functional theory (DFT) calculations of the exchange couplings by Alexander A. Tsirlin. Elias Papke optimized the exchange couplings and the experimentally determined propagation vector could be perfectly recreated. Finally, the system will be compared to the anisotropic TLAF presented in Subsec. 2.7.2.

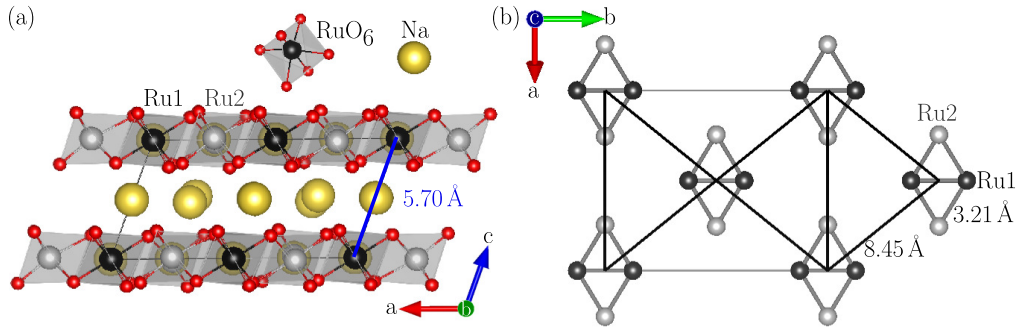

Figure 4.6.: Crystal structure of Na_3RuO_4. The distances refer to the crystal structure at 300 K. (a) The Ru^{5+} ions form magnetic layers which are stacked along the monoclinic c axis. The Ru layers are separated by Na^+ ions. (b) View of the unit cell along the c axis. The Ru ions are arranged such that a triangular motif can be found on two different length scales. Two isosceles triangles form tetramers (drawn in gray) which form a triangular lattice as well (drawn in black). The octahedral coordination and the Na atoms are omitted for clarity. The RuO_6 octahedra are bridged over the edges. The visualization program `VESTA` was used to depict the crystal structure [93].

4.2.1. Room-temperature Crystal Structure

One interesting aspect of Na_3RuO_4 lies within the crystal structure. The unit cell is shown in Fig. 4.6. The triangular motif, one possible prerequisite for geometrical frustration, is found on two different length scales. The edged-shared $Ru^{5+}O_6$ octahedra form lozenges with an edge length of around 3.21 Å. The tetramers are composed of two isosceles triangles. The lozenge units again are arranged on a secondary triangular lattice, also referred to as simplex lattice [106]. The triangles forming this simplex lattice are isosceles as well with the two shortest edges of 8.45 Å. The triangular layers are stacked along the crystallographic c axis and are separated by non-magnetic Na^+ layers.

The crystal structure is described with the monoclinic space group $C2/m$ (no. 12). The lattice parameters obtained from the refinement for the neutron diffraction data at 300 K are $a = 11.0280(3)$ Å, $b = 12.8141(3)$ Å, $c = 5.7047(2)$ Å, and $\beta = 109.906(2)\,°$. The lattice parameters are in perfect agreement with the values from [55]. It is noted in passing, that the table for atomic coordinates in Ref. [107] contains two typos (for atom Na3 $z = 0.5$ and for atom O3 $y = 0.5$).

The temperature dependence of the crystal structure was investigated with neutron diffraction and the results are given in Subsec. 4.2.3.

4.2.2. Thermodynamic Properties

Fig. 4.7(a) shows the temperature dependent heat capacity between 2 K and 50 K. The heat capacity is field independent to at least 7 T. Striking are two successive phase transitions at 26 K and 29 K. The data are in good accordance with the heat capacity given in Ref. [107]. The double peak characteristic in the heat capacity was also reported in Ref. [49] and assigned to Na_2RuO_3. This is in contrast to the findings of this work. For Na_2RuO_3 no phase transition was detected (see Fig. 4.3). The compound in Ref. [49] was most likely miscategorized, which was also stated in Ref. [51]. This can be explained by the easy formation of Na_3RuO_4 as a side product during the synthesis of Na_2RuO_3 if the reducing atmosphere is not sufficient.

The magnetic susceptibility and Fisher's heat capacity, given in Figs. 4.7(b) and 4.7(a), respectively, show one antiferromagnetic transition at 30 K. The paramagnetic regime follows a Curie-Weiss behavior and the corresponding fit of the Curie-Weiss equation $\chi = \chi_0 + (C/(T - \theta))$ to the data collected at 1 T between 150 and 300 K is depicted in Fig. 4.7(b) in red. A Curie-Weiss temperature θ_{CW} of -161.5(5) K and an effective moment of 4.07(2) μ_{B} are obtained. The fit parameters obtained by fitting the data collected at 3 and 7 T differ less than 2%. The value of the effective moment is close to the spin-only value 3.87 μ_{B} expected for Ru^{5+} carrying a spin of $S = 3/2$. The diamagnetic susceptibility of Na_3RuO_4 was calculated from Pascal's constants taken from [108] to $\chi_{\mathrm{dia}} \approx -9 \cdot 10^{-5}$ emu/mol. A similar contribution as for Ru^{3+} and Ru^{4+} was assumed for Ru^{5+}. The temperature independent constant χ_0 accounts for the diamagnetic contribution from the sample and the background ($\chi_0 = -4.97(8) \cdot 10^{-4}$ emu/mol). The inset in Fig. 4.7(b) shows

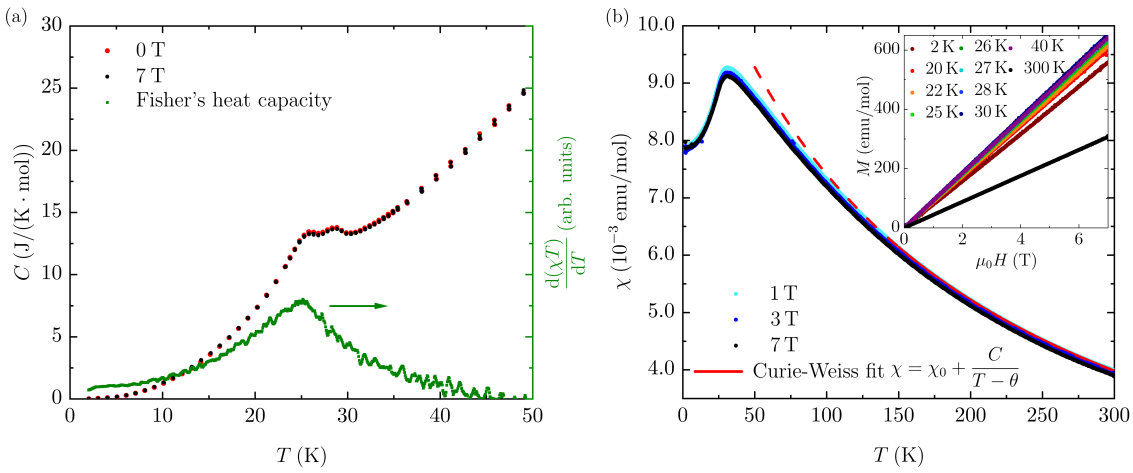

Figure 4.7.: Thermodynamic properties of Na_3RuO_4. (a) The measured heat capacity shows no dependence on the magnetic field up to 7 T. Clearly visible are two phase transitions at 26 and 29 K. Only one phase transition is observed in Fisher's heat capacity depicted in green. (b) The magnetic susceptibility measured at 1, 3, and 7 T reveals an antiferromagnetic phase transition at around 30 K. The high-temperature susceptibilities follow a Curie-Weiss behavior and the Curie-Weiss fit between 150 and 300 K is shown for the data collected at 1 T. The field-dependent magnetization for temperatures between 2 and 300 K is given in the inset. The magnetization shows a linear field dependence.

the linear magnetization with magnetic field for temperatures between 2 and 300 K. The slope in the paramagnetic regime increases with decreasing temperature. The slope decreases again after passing the antiferromagnetic transition temperature of 30 K, which was already expected from the susceptibility data.

The ratio of Curie-Weiss temperature and Néel temperature $\theta_{\mathrm{CW}}/\mathrm{T_N} \approx 5.4$ could already indicate a medium frustrated system in which magnetic ordering is shifted to lower temperatures. However, a weaker coupling between the tetramers compared to the intra-tetramer coupling could have the same effect on the ratio. If frustration is present in the system can be revealed by the determination of the magnetic structure with elastic neutron scattering. Additionally, neutron diffraction allows to clarify if both transitions are magnetic, but not resolvable in the magnetic susceptibility, or if one of them is structural. In the next section these open questions will be answered by determining the Néel temperature, the size of the ordered magnetic moment and the magnetic structure from neutron diffraction experiments.

4.2.3. Neutron Diffraction

Temperature-dependent Crystal Structure

First, to determine the temperature dependent cell parameters with high precision, experiments were performed at the high-resolution instrument D2B. The neutron diffraction data collected above the transition temperatures at 40 K, in the transition region at 27 K, and well below the transitions at the base temperature 1.5 K are given in Fig. 4.8(a). Pure nuclear scattering which is measured at high angles and given in the inset of Fig. 4.8(a) excludes a structural phase transition. No additional peaks or peak splitting indicating symmetry lowering is observed below the transition temperatures. Hence, both transitions observed in the heat capacity data must be of magnetic nature. The $C2/m$ space group describes the structure throughout the temperature window of the experiment and the refined monoclinic cell parameters are given in Fig. 4.8(b) in dependence of the temperature. No hints towards a structural phase transition can be seen in the evolution of the cell parameters which do not show any anomalies but decrease monotonically with decreasing temperature. Below 50 K the parameters a and c show a slight upturn. This is already an indication for magnetic ordering below 50 K which is accompanied by spin induced lattice deformations mediated through spin-lattice coupling. Indeed, magnetic Bragg peaks are discernible at low angles and the four peaks visible at 1.5 K are indicated with arrows in Fig. 4.8(a). At 15.5° first signs of magnetic ordering

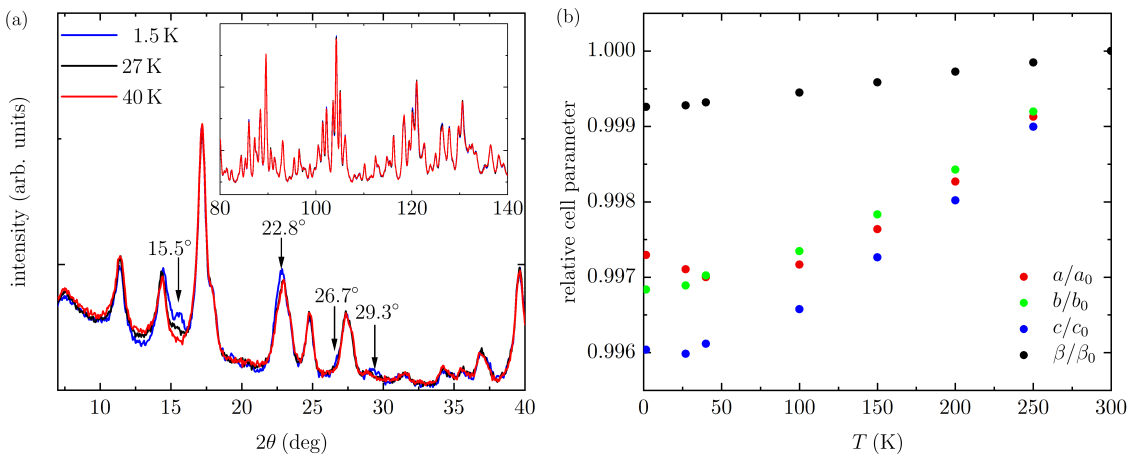

Figure 4.8.: Na_3RuO_4 high-resolution neutron diffraction data. (a) Neutron diffraction pattern at low angles recorded above the transition temperatures (40 K), in the transition region (27 K), and below the transitions at the base temperature (1.5 K). The four magnetic peaks visible at 1.5 K, and partly at 27 K, are indicated with arrows. The data at higher angles are shown in the inset. A structural phase transition can be ruled out. (b) The refined cell parameters of the monoclinic unit cell decrease monotonically with decreasing temperature. Below 50 K a and c increase slightly. The cell parameters were normalized with respect to the values at 300 K. The error bars are smaller than the symbol size.

are already visible at 27 K. At 40 K no magnetic scattering is recorded, which fits to the data presented in Subsec. 4.2.2.

At the beginning, the tetramers were thought to be magnetically decoupled, which would not be surprising given the fact that NaO_6 octahedra separate the tetramers in the plane and in adjacent layers [109]. Magnetization and elastic neutron scattering data presented herein show long-range magnetic order below 30 K and thus prove inter-tetramer coupling. If the inter-tetramer coupling is weak compared to the intra-tetramer coupling or if their strengths are comparable in size and competing interactions are at play, needs to be investigated. An analysis of the magnetic structure is not possible with the data obtained from D2B because of the lower intensity in the high-resolution mode. Therefore, in the next step, measurements at the high-intensity instrument D20 were performed. The collected data are discussed in the following section.

Magnetic Structure

For a first overview, the thermo diffraction pattern between 5 and 30 K was recorded at the high-intensity instrument D20. The nuclear background was subtracted and the magnetic contribution is given in Fig. 4.9. Two conclusions can be drawn from the measurements. First, the two phase transitions observed in the heat capacity are also reflected in the magnetic diffraction data. This is expected since both transitions were already known to have magnetic character. Upon cooling, a first set

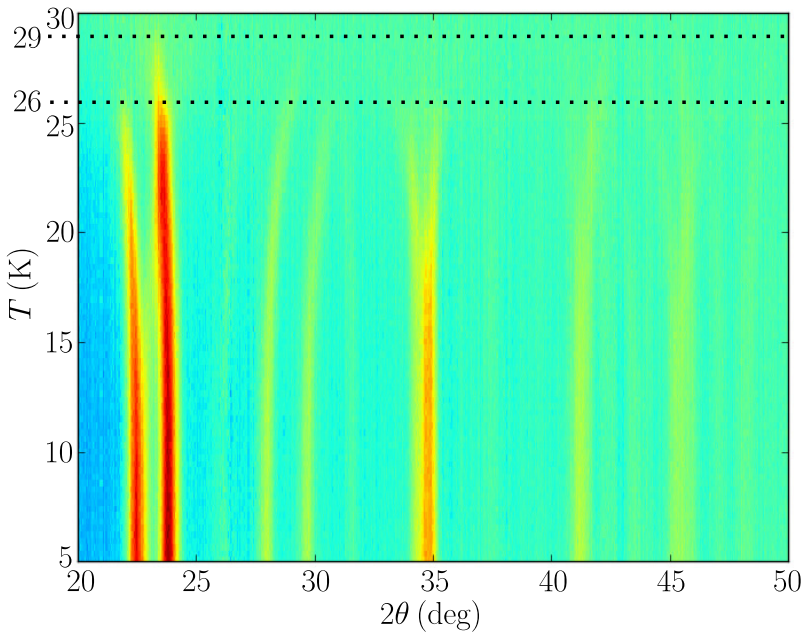

Figure 4.9.: The thermo-diffraction pattern of Na_3RuO_4 shows the magnetic contribution after subtraction of the nuclear background in dependence of the scattering angle and the temperature. Two sets of magnetic peaks emerging at 26 and 29 K, respectively, are distinguishable.

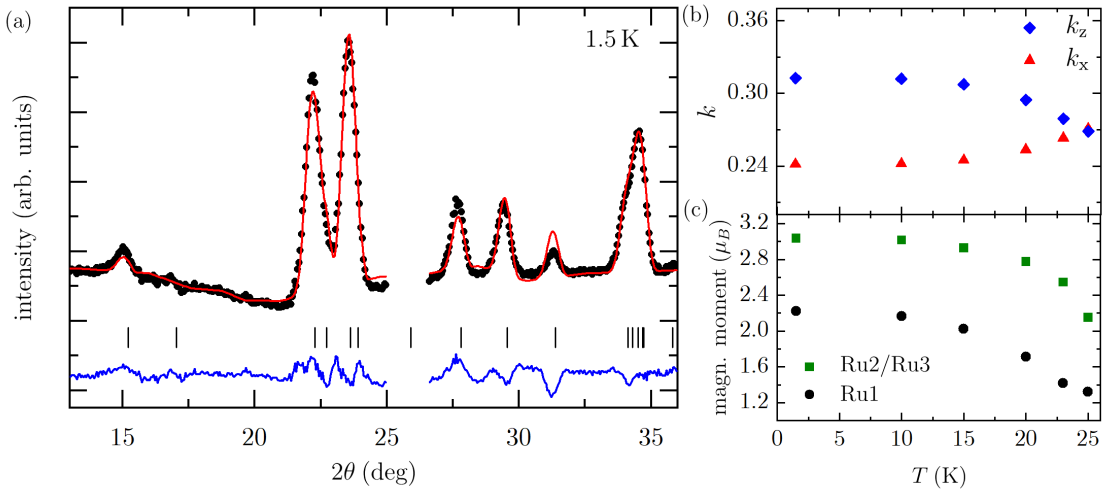

Figure 4.10.: Refinement of the magnetic structure of Na_3RuO_4. (a) Magnetic diffraction pattern at 1.5 K after subtraction of the nuclear background. The data (black dots) can be described accurately with the refined magnetic structure model. The residual magnetic R-factor is 4.79. The difference between experiment and fit is shown in blue. The black ticks mark the positions of the magnetic peaks. (b) Dependence of the components of the propagation vector k_x and k_z with temperature. (c) Dependence of the magnetic moments of Ru1 and Ru2/Ru3 with temperature. The error bars are smaller than the symbol size.

of magnetic Bragg peaks emerges at 29 K and a second set appears at 26 K. These transition temperatures fit perfectly to those determined earlier with the heat capacity. No further transitions are detectable. Second, the magnetic peak positions shift stronger with temperature compared to the nuclear positions. This already shows that the magnetic structure is incommensurate.

In the next step, measurements at fixed temperatures were recorded for a magnetic refinement. The magnetic diffraction pattern at 1.5 K is given in Fig. 4.10(a) in black. The propagation vector is determined from the positions of the magnetic Bragg peaks. The exact procedure is described in the following.

The cell parameters were refined for the data collected at 40 K at the high-resolution instrument D2B. The cell parameters can thus be determined with high precision and were taken and fixed during the refinement for the data collected at 40 K at the instrument D20. The wavelength and zero-shift were kept as refinable parameters. The magnetic peak positions at 1.5 K were determined and corrected for the zero-shift. Peak positions can be conveniently obtained with the program `WinPLOTR` [110]. The refined cell parameters, the wavelength, and the positions of the magnetic peaks were listed in an input file for the software `k-SEARCH`. The information was added that the propagation vector is incommensurate. `k-SEARCH` then generates an output file containing possible propagation vectors and their corresponding residual R-values. Reasonable vectors must be chosen and compared in a LeBail refinement. Experience is necessary in identifying reasonable vectors from the

list and would not have been possible without the help of the local contact Clemens Ritter. The propagation vector was found to be $\vec{k} = (0.2415(2), 0, 0.3127(2))$ and creates the magnetic peak positions with a residual R-value of ≈ 4.7. The incommensurability along c points already towards significant coupling between the layers, which will be addressed later in this subsection.

The software `BASIREPS` was used to determine all allowed irreducible representations and their basis vectors. After comparing the different possibilities one is left with an irreducible representation of dimension one and three basis functions. The final magnetic refinement for the data collected at 1.5 K is shown in Fig. 4.10. The residual nuclear peak in the angular region of 26 ° was excluded. The second Ru site is split by the propagation vector leading to three different Ru sites in the magnetic refinement (see Fig. 4.11). The Ru atom on site 1 carries the magnetic moment of $2.23(3)\,\mu_B$ and the magnetic moment of the Ru atoms on the split positions is $3.04(3)\,\mu_B$. These values are close to $3\,\mu_B$, the saturated moment of a $J = 3/2$ ion in the spin-only case. Without loss of the fit quality the magnetic moments of the Ru atoms on the former site 2 were restricted to be equal. The size of the magnetic moment at different temperatures was refined and the temperature dependence between 1.5 and 25 K is shown in Fig. 4.10(c). The magnetic moment could not be extracted from the data collected at 27 and 29 K. Between 1.5 and 10 K the magnetic moments stay constant within experimental error. Above 10 K the magnetic moments of the Ru atoms on site 1 and 2/3 decrease monotonically and have dropped at 25 K to 60% and 70% of the initial value.

Also the x and z components of the propagation vector first show a slow and then a strong change with increasing temperature. Between 1.5 and 15 K k_x and k_z change only around 2%. Up to 25 K the components change around 10% and both components merge at 25 K. The magnetic structure at 1.5 K is shown in Fig. 4.11. The individual tetramers are not frustrated but are antiferromagnetic units with a small phase shift of $\phi = 0.0924(31)$ concerning the moment of the Ru3 atoms. Refinement in the case of a spin density wave shows that all spin amplitudes are directed along c. The size of the magnetic moment is modulated incommensurately along the crystallographic a and c axis. In an isotropic system the helical structure evolves whereas in an anisotropic system the spins keep pointing along the easy axis and instead the size of the magnetic moment is modulated. The collinear spin density wave cannot be distinguished from a helical structure with unpolarized neutrons. With the same periodicity the same Bragg pattern is observed. Determination of the anisotropy via numerical calculations or direction dependent magnetization measurements on single crystals could point towards one of the two possible scenarios. Polarized single crystal neutron diffraction would be necessary to determine the magnetic structure unambiguously. The intensities of the spin-flip and non-spin flip channels for the magnetic Bragg peaks with the scattering vector perpendicular to the neutron spin polarization give information about the spin components in the plane perpendicular to the scattering vector [111]. Here, experiments with spin polarized neutrons along c would clarify if a spin density wave as depicted in Fig. 4.11 or a helical spin structure or a combination of those spin structures is present, but this investigation

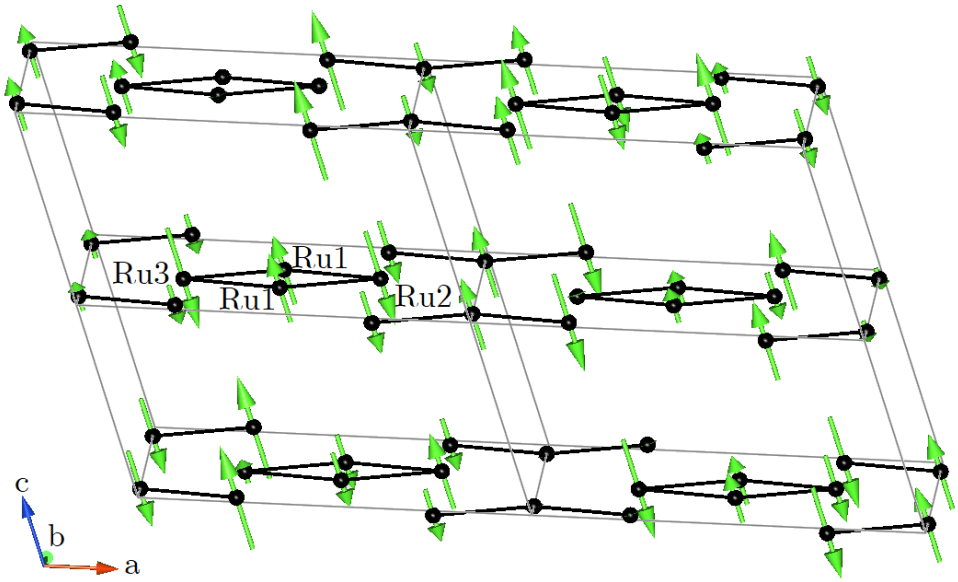

Figure 4.11.: Magnetic structure of Na_3RuO_4 obtained from powder neutron diffraction. The tetramers are nearly antiferromagnetic units and the spin density wave is modulated sinusoidally along a and c. The magnetic structure was depicted with the software `FpStudio`.

goes beyond the scope of this work.

The incommensurability of the magnetic order in the ab plane results from competing exchange interactions between the tetramers. Competing interactions between the tetramers lead also to incommensurability along c, because the c axis is not perpendicular to the ab plane in the monoclinic structure. To complete the picture, intra and inter-tetramer exchange couplings obtained from *ab-initio* DFT+U calculations (with the Coulomb and Hund exchange interaction $U_\mathrm{d} = 3\,\mathrm{eV}$ and $J_\mathrm{H} = 0.5\,\mathrm{eV}$, respectively) and their optimization via energy minimization [112] are summarized briefly in the following. The couplings are listed in Tab. 4.1. $J_\mathrm{ex} > 0$ for antiferromagnetic coupling and $J_\mathrm{ex} < 0$ for ferromagnetic coupling. The listed couplings are illustrated in Fig. 4.12 whereby the strength of the coupling scales with the thickness of the line.

An initial rough examination shows that the couplings fit to the observed magnetic structure. The leading intra-tetramer exchange energy $J2$ couples the spins antiferromagnetically along the edges of the tetramer. This fits to the scenario of antiferromagnetic units observed experimentally. The ferromagnetic exchange interaction $J1$ is compatible with that antiferromagnetic arrangement. $J3$ is a competing interaction but an order of magnitude smaller than $J2$ and hence, does not destroy the antiferromagnetic arrangement. The dominant interactions between the tetramers $J4$ and $J5$ are competing and explain the incommensurability in the magnetic structure along a. In contrast to $J8$, $J9$ couples oblique to the crystallographic c axis and the incommensurability along c is not surprising. Moreover, the k_x and

Table 4.1.: Exchange couplings in Na_3RuO_4. The labels are illustrated in Fig. 4.12. Listed are the values obtained from *ab-initio* DFT ($U_d = 3\,eV$, $J_H = 0.5\,eV$) and from further optimization to better match the experimental propagation vector. Antiferromagnetic couplings are positive and ferromagnetic couplings are negative.

bond	label	d (Å)	J_{ex} (K) DFT	J_{ex} (K) opt.
within the tetramer				
Ru1-Ru1	$J1$	3.210	-4.9	-4.90
Ru1-Ru2	$J2$	3.210	30.2	30.28
Ru2-Ru2	$J3$	5.559	2.0	1.96
between the tetramers in the *ab* plane				
Ru2-Ru2	$J4$	5.477	34.7	34.70
Ru1-Ru2	$J5$	5.531	23.4	24.68
Ru1-Ru1	$J6$	6.376	7.1	5.84
Ru2-Ru2	$J7$	6.413	2.0	1.97
between the *ab* planes				
Ru1-Ru1	$J8$	5.703	6.1	3.53
Ru2-Ru2	$J9$	6.262	20.9	21.83

k_z values are linked because the incommensurability along c is mostly due to the incommensurate order in the ab plane.

In a more quantitative approach in Ref. [112], the propagation vector resulting from the couplings determined via DFT was calculated. To this end, $E(\vec{k})$, the energy function assuming sinusoidal modulation of the magnetic moments and summing over all relevant bonds was set up and the couplings from DFT were fixed. The propagation vector was determined by numerical minimization with k_x, k_y, k_z and phase shifts between the different Ru ions taken as free parameters to $\vec{k}_{calc} = (0.2495, 0, 0.3502)$ and deviates around 9% from the experiment at 1.5 K ($\vec{k}_{exp} = (0.2415(2), 0, 0.3127(2))$). In contrast to the refinement for which a phase shift ϕ concerning the moment of the Ru3 atom was introduced, in Ref. [112] $\Delta\phi$ was defined as phase shift between neighboring atoms of the tetramer. A small phase shift $\Delta\phi = 0.01074$ was determined and confirms the almost antiferromagnetic arrangement of the tetramers obtained from the refinement with $\phi = 0.0924(31)$ at 1.5 K. In the next step, the exchange couplings $J1$ to $J9$ were optimized by making use of the experimental propagation vector and following the gradient of $\left|\vec{k}_{calc}(J1, ..., J9) - \vec{k}_{exp}\right|$ until the final propagation vector $\vec{k}_{calc} = (0.2420, 0, 0.3120)$ deviating less than 0.3% from the experimental propagation vector was reached. The optimized parameters were added in Tab. 4.1. It has to be kept in mind that the values can not be determined unambiguously as the nine coupling constants are optimized against only three values determined experimentally. The good agree-

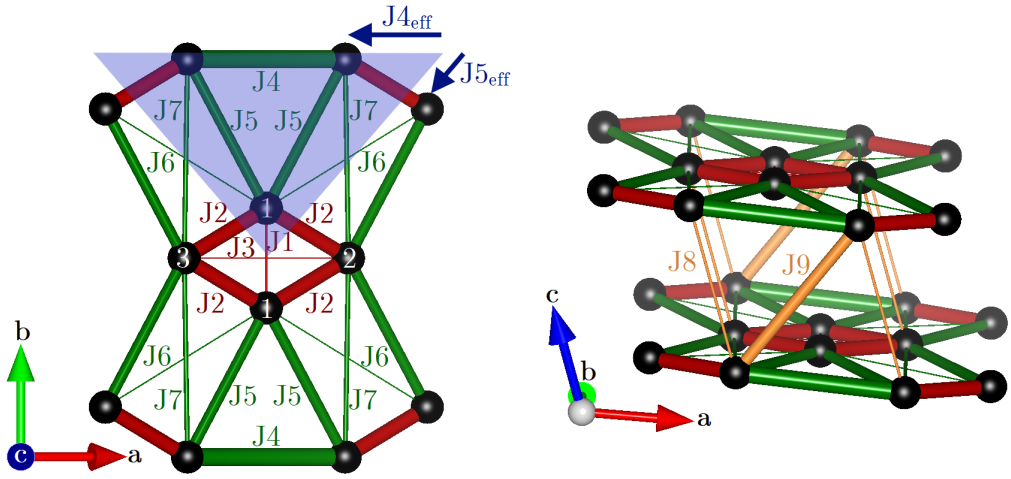

Figure 4.12.: Illustration of the exchange couplings in Na_3RuO_4. The strength of the couplings scales with the thickness of the line. Depicted in red are the intra-tetramer couplings, in green the inter-tetramer couplings, and in orange the interlayer couplings. Additionally, the effective couplings between the tetramer units are indicated in blue. The visualization program `VESTA` was used to depict the structures [93].

ment of the DFT and optimized values suggests that the starting values from DFT are reasonable and that the overall tendency is sound.

In the following the interplay of the calculated exchange interactions in view of the incommensurability of the magnetic structure in the *ab* plane will be discussed. In Ref. [112] it was shown that the four main interactions $J2$, $J4$, $J5$, and $J9$ are already sufficient to obtain the propagation vector similar to the experimental one. $J2$ and $J9$ do not add frustration into the system and the incommensurability can be led back to the competition between the exchange couplings $J4$ and $J5$. Indeed, keeping all exchange couplings constant and lowering $J4$ below the critical value 26.2 K leads to antiferromagnetic tetramers tiling up the *ab* plane, which is described by the propagation vector $\vec{k} = (0, 0, 1/2)$. Instead of lowering $J4$, $J5$ can be raised above 31.9 K to create the same result. The ratio $J4/J5$ is crucial for the formation of an incommensurate order.

To deduce now the incommensurability along c, it was shown in Ref. [112] that $J4$, $J8$, and $J9$ as the only couplings between the antiferromagnetic tetramers would not create an incommensurate structure, because $J8$ is too weak, but lead to a ferromagnetic stacking along c described by $\vec{k} = (1/2, 0, 0)$. By setting $J8 = 0$, which complies with the DFT result $J8 \ll J9$, the energy in dependence of k_z can be written as $E_{J8=0}(k_z) = J9 \cos(2\pi(k_x + k_z + \phi))$ and k_x and k_z are linked through the condition $k_x + k_z + \phi = 0.5$. The experimentally determined values nearly fulfill this condition $k_x + k_z + \phi = 0.6466(35)$.

Ignoring the small phase shift and assuming purely antiferromagnetic tetramers, parallels can be drawn to the anisotropic triangular lattice discussed in Subsec. 2.7.2. In the following only the in-plane propagation vector will be considered and the inter-

planar couplings will be neglected. Each tetramer can be treated as single magnetic site which couples to the neighboring tetramers via $J4_{\text{eff}}$ and $J5_{\text{eff}}$ as indicated in Fig. 4.12. Thus an anisotropic $J4_{\text{eff}}$ - $J5_{\text{eff}}$ triangular lattice is formed. Setting $k_{\text{y}} = 0$ as observed experimentally, the energy function is given by

$$E_{\text{ab}} = J4\cos(2\pi k_{\text{x}}) + 2\,(-2\,J5 + J6 + J7)\cos(\pi k_{\text{x}}). \tag{4.3}$$

Comparison with equation 2.65 shows that equation 4.3 describes an anisotropic triangular lattice if the effective antiferromagnetic coupling $J4_{\text{eff}} = J4$ and the effective ferromagnetic coupling $J5_{\text{eff}} = -2 \cdot J5 + J6 + J7$ are introduced. In the case of incommensurability the ratio of $J5_{\text{eff}}$ to $J4_{\text{eff}}$ dictates k_{x} via $\cos(\pi \cdot k_x) = -J5_{\text{eff}}/2J4_{\text{eff}}$ and to recreate the experimentally determined k_x of 0.2415, $J5_{\text{eff}}/J4_{\text{eff}} = -1.45$ must hold. Despite the simplifications made, the optimized exchange couplings yield a similar value $J5_{\text{eff}}/J4_{\text{eff}} = -1.20$ and the anisotropic triangular lattice is a justified model for the secondary triangular lattice.

From this point of view, the two successive magnetic phase transitions are not surprising and are commonly found in TLAFs. TLAFs show a rich phase diagram with various spin structures though temperature independent phase transitions in a larger magnetic field window as observed for Na_3RuO_4 between 0 and 7 T are unusual. It has to be kept in mind that Na_3RuO_4 has a secondary triangular lattice and a direct comparison with the spin structures in TLAFs is difficult. No statement can be made if the phase transition between the magnetic phases is due to a spin-reorientation process or due to the vanishing of the second independent magnetic moment upon increasing the temperature.

The section about Na_3RuO_4 with a secondary triangular lattice is now closed and in the following two sections the two antiferromagnets $Na_2BaCo(PO_4)_2$ and $Na_2SrCo(PO_4)_2$ with a simple triangular lattice will be discussed.

4.3. $Na_2BaCo(PO_4)_2$

In this section the $S = 1/2$ TLAF $Na_2BaCo(PO_4)_2$ will be presented. In the first publication about $Na_2BaCo(PO_4)_2$ the compound was presented as possible candidate hosting a spin-liquid state based on ac susceptibility measurements which do not show any static magnetism down to 50 mK [4]. This set the ball rolling and many experimental and theoretical reports followed. The results reported are highly contradictory and further efforts from both the experimental and theoretical side are necessary to define the low-temperature states and properties unambiguously. The controversy is described in what follows and an overview of all the publications so far is given.

$Na_2BaCo(PO_4)_2$ is reported to crystallize in the trigonal crystal structure $P\bar{3}m1$. The octahedrally coordinated Co^{2+} ions form an ideal triangular network in the *ab* plane. The magnetic layers are separated by non-magnetic ions and are stacked along *c* (see Fig. 4.13). At low temperatures the Co^{2+} ions have an effective spin-1/2 (see Sec. 2.4 and Fig. 2.5).

The absence of long-range magnetic order was later supported by muon spin relaxation measurements which show a dynamically fluctuating ground state down to 80 mK [113]. As summarized in Subsec. 2.7.3 a spin liquid can only be realized if nnn interactions and/or off-diagonal anisotropy are present in the system. In $Na_2BaCo(PO_4)_2$ the CoO_6 octahedra are not directly linked but connected via PO_4 tetrahedra and the nnn distance of around 9.2 Å is nearly twice as large as the nn distance of around 5.3 Å. Hence, off-diagonal anisotropy and nnn exchange are expected to be insignificant and the simple nn XXZ model describes the system. From this perspective not a QSL but an ordered 120° non-collinear ground state is expected in $Na_2BaCo(PO_4)_2$.

Indeed, the here presented heat capacity data collected by Noah Winterhalter-Stocker show a phase transition at 147 mK in zero magnetic field. This contrasts with

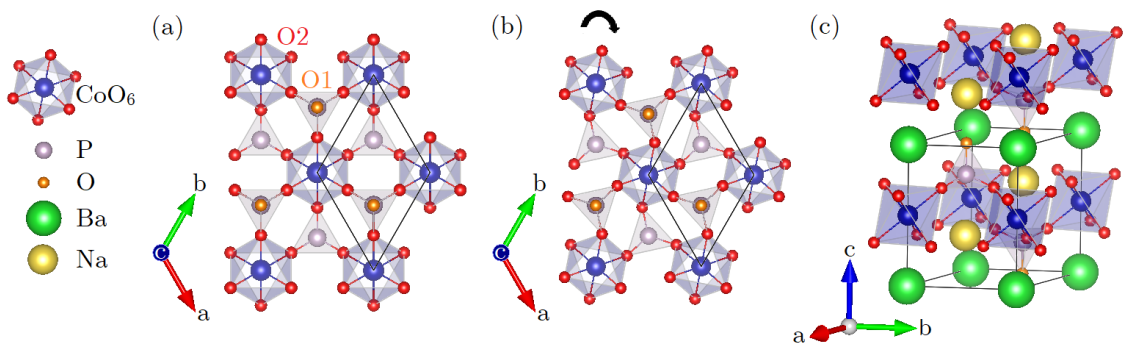

Figure 4.13.: Crystal structure of $Na_2BaCo(PO_4)_2$. (a) and (b) Triangular layer in the case of the $P\bar{3}m1$ and $P\bar{3}$ symmetry, respectively. The Na and Ba ions are omitted for clarity. In the case of $P\bar{3}$ ferrorotations of the Co octahedra are allowed. (c) The triangular layers are stacked along *c* and are separated by non magnetic layers. Illustrated is the $P\bar{3}$ structure and the unit cell is indicated with the black lines.

the experimental findings reported in Refs. [4, 113] but fits to the low-temperture heat capacity data shown in Ref. [114]. Additionally to the phase transition at 148 mK, Ref. [114] found a residual linear term by extrapolating the thermal conductivity in zero magnetic field above T_N. This could point towards the existence of gapless spinons and a QSL-like state above T_N. By modeling the ground state numerically Ref. [115] predicts a phase without magnetic order, possibly a QSL state, if besides nn Ising interactions Kitaev interactions are introduced into the system. Through theoretical considerations Ref. [16] found sizable Kitaev interactions in $Na_2BaCo(PO_4)_2$. Their ESR data suggest that magnetic correlations set in two orders of magnitude above T_N, which let them put $Na_2BaCo(PO_4)_2$ forward as Kitaev-exchange assisted QSL.

However, the picture of a QSL-like regime above T_N is challenged by other groups. While Ref. [116] confirms the phase transition, yet at 139 mK, the thermal conductivity could not be reproduced and the residual linear terms in different samples are negligible. In Ref. [117] heat capacity and magnetization could be successfully modeled assuming the simple XXZ model with negligible perturbations. The publication suggests a spin supersolid state in $Na_2BaCo(PO_4)_2$. Also Ref. [118] supports the picture of $Na_2BaCo(PO_4)_2$ being a TLAF which can be described with an easy-axis XXZ model. The experimental determined phase diagrams for in-plane and out-of-plane field directions are in good accordance to the theoretical phase diagrams for XXZ compounds. Neutron scattering showed a strongly reduced ordered moment of the Co ions, which indicates strong quantum fluctuations. The neutron diffraction data can be explained with the Y configuration expected for XXZ model TLAFs but the spin configuration could not be determined unambiguously.

In this work, the analysis of the heat capacity and magnetization data support the picture of a nn spin-1/2 TLAF with easy-axis anisotropy. The heat capacity in the milli-Kelvin temperature regime measured by Noah Winterhalter-Stocker confirm the phase transition in zero magnetic field published in the literature and hint towards a further transition below 50 mK.

All the reports so far agree on the space group $P\overline{3}m1$. The atomic displacement parameters (ADPs) are given in Ref. [4] and the atomic displacement is rather high for one of the O positions. Therefore, high-resolution synchrotron diffraction measurements were performed in dependence of the temperature. The crystal structure is trigonal but in contrast to the published $P\overline{3}m1$ space group, this study reveals a $P\overline{3}$ space group symmetry. The absence of the mirror plane allows ferrorotations of the Co octahedra [see Fig. 4.13 (a) and (b)]. Refinements for the synchrotron data between 2 and 300 K reveal a slightly enhanced ADP of Na compared to the displacements of the other elements. The displacements accompany structural dynamics which are further confirmed by NMR. The temperature dependence of the ADPs shows that the structural dynamics become frozen below 50 K. As for the previous presented compounds, the characterization of the crystal structure is presented before the properties are addressed.

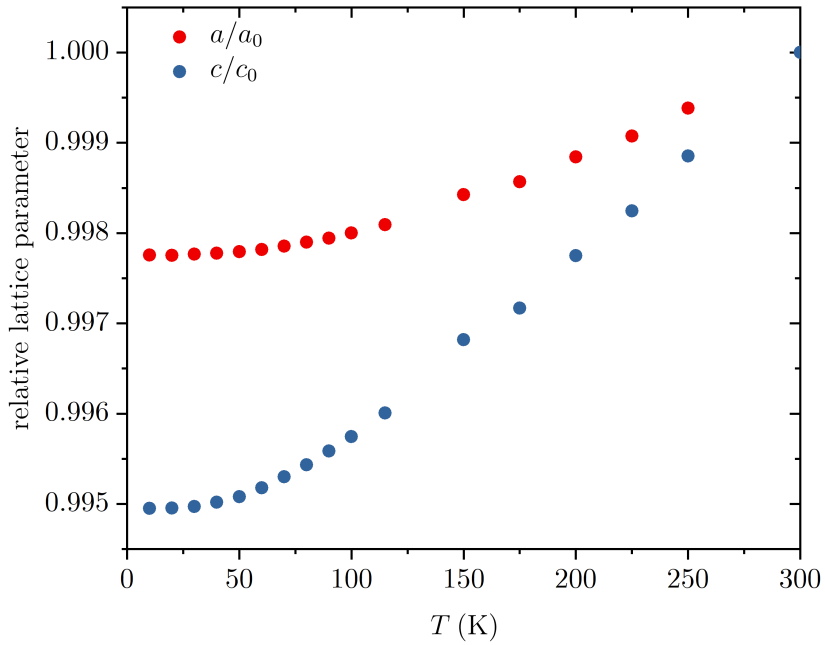

Figure 4.14.: Temperature dependence of the lattice parameters of $Na_2BaCo(PO_4)_2$. The error bars are smaller than the symbol size.

4.3.1. Crystal Structure

The published space group for $Na_2BaCo(PO_4)_2$ is $P\bar{3}m1$ (no. 164) [4]. The Co ions are octahedrally coordinated by O ions and the octahedra are connected via PO_4 tetrahedra [see Fig. 4.13(a)]. The octahedra form triangular layers in the *ab* plane which are stacked along *c*. Na ions fill the voids in the triangular layers and the layers are separated by Ba ions.

The trigonal lattice parameters at 300 K were determined to $a = 5.316677(5)$ Å and $c = 7.009656(8)$ Å through the refinement for the synchrotron XRPD data and are in good accordance with the lattice constants determined in Ref. [4]. The lattice parameters extracted from synchrotron XRPD between 10 K and 300 K and normalized to the values at 300 K are shown in Fig. 4.14. The lattice parameters in

Table 4.2.: Atomic positions and ADPs for $Na_2BaCo(PO_4)_2$ in the space group $P\bar{3}m1$ at 300 K.

Atom	x	y	z	U_{iso} [Å^2]
Ba	0	0	0	0.0048(1)
Co	0	0	0.5	0.0047(2)
P	0.3333	0.6667	0.2438(4)	0.0044(3)
Na	0.3333	0.6667	0.6748(6)	0.0181(8)
O1	0.3333	0.6667	0.022(1)	0.014(1)
O2	0.1746(4)	0.8254(4)	0.3192(6)	0.034(1)

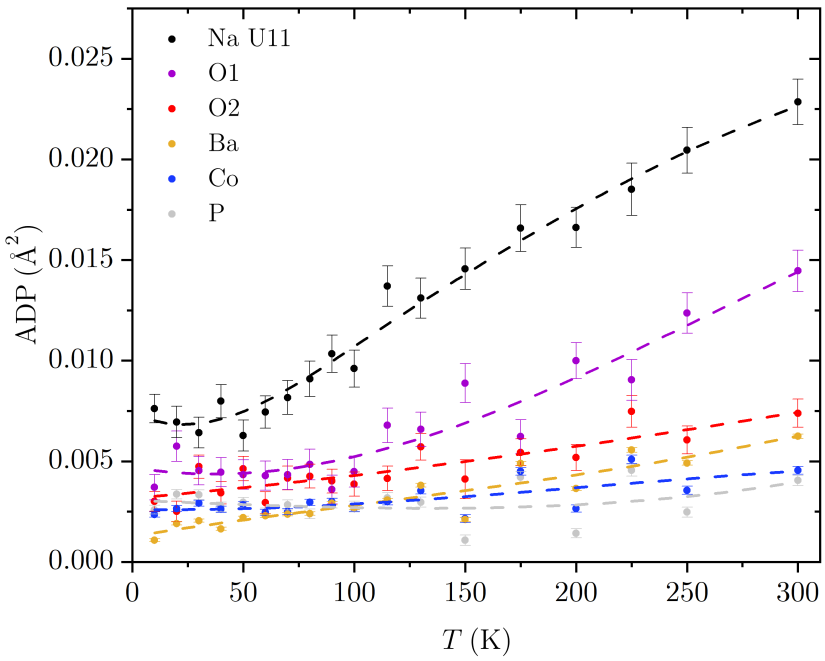

Figure 4.15.: Temperature dependence of the ADPs of $Na_2BaCo(PO_4)_2$. The values were obtained from the refinement with the space group $P\overline{3}$ and are thus different from the values listed in Table 4.2. The lines are guides for the eye.

dependence of the temperature do not show any anomalies and no peak splitting or superstructure reflections were observed in the whole temperature range. Therefore, a structural phase transition can be ruled out.

The atomic positions and isotropic ADPs at 300 K obtained by refining the $P\overline{3}m1$ structural model are listed in Tab. 4.2. Striking is the rather high ADP of 0.034(1) Å^2 for the O2 ion. The value is around three times larger than the ADP for the second O1 position. The two different O positions are marked in Fig. 4.13. The O1 ion is not connected to Co but part of the PO_4 tetrahedra. The large ADP is an indication that the atomic position of the O2 ion is slightly off the real position and hence that the space group symmetry is not chosen correctly. Glaserite type materials show a broad range of structure types. Another candidate structure is $P\overline{3}$ (no. 147) which is simply obtained from $P\overline{3}m1$ by removing the mirror plane symmetry element. If the symmetry is lowered from $P\overline{3}m1$ to $P\overline{3}$, ferrorotations of the Co octahedra are allowed [see Fig. 4.13(a) and (b)]. The rotation angle at 10 K was refined to be 9.4(2) °. The O1 ions are not affected by the rotations which explains the high ADPs in the $P\overline{3}m1$ case for O2 only. For the $P\overline{3}$ structure model the temperature dependence of the ADPs between 10 and 300 K is shown in Fig. 4.15. The ADPs are all in a reasonable range and the temperature dependence does not reveal any anomalies. A closer look at the ADPs shows that the values for Na are the highest at every temperature and the ADPs for Na and O1 increase strongly with increasing temperature. While all other ADPs are below 0.008 Å^2 at room temperature, U_{11}

of Na is 0.023(2) Å^2 and U_{iso} of O1 is 0.014(1) Å^2. In contrast to the displacements of Na, which appear mainly in the *ab* plane, the ADPs for the other elements were refined to be isotropic. The displacements are connected to structural dynamics which affect mainly Na and the flattening of the ADP of Na below 50 K indicates the freezing of the displacements and hence the dynamics. The dynamics and its temperature dependence are further investigated with NMR presented in the next subsection.

4.3.2. Nuclear Magnetic Resonance

The disorder in the structure revealed through the ADPs is also seen in the ^{23}Na NMR spectra. ^{23}Na is a nucleus with quadrupolar moment with spin 3/2 so three allowed transitions for the magnetic field parallel and perpendicular *c* are observed [see Fig. 4.16(a) and (b)]. It is striking that the satellite transitions are much broader than the central transition. The width of the narrow central peak is due to an inhomogeneous hyperfine shift. The difference of the frequency of the satellite compared to the central transition is caused by the quadrupolar interaction. The broad lines indicate that there is a distribution of the quadrupolar interaction, therefore of the local electric field gradient. This in turn indicates an intrinsic disorder involving the displacement of Na. The ^{23}Na spectrum and the high-resolution MAS NMR ^{31}P spectrum recorded at room temperature show single resonance indicating that the distortions are dynamical (see Fig. 4.16).

The Na displacement is also apparent from the angular dependence of the ^{23}Na Knight shift given in Fig. 4.17. The data were collected at room temperature and the crystal was rotated around the *c* axis. Captured was the hyperfine shift of the central transition in the *ab* plane. The Knight shift shows a sinusoidal behavior and can be described by $724\,\text{ppm} + 27 \cdot \cos(2\pi \cdot (\upsilon + 24)/180)$ ppm with the rotation angle υ. The angular dependence of the Knight shift clearly shows the absence of 3-fold rotation and confirms the displacements of the Na atoms away from the 3-fold rotation axis.

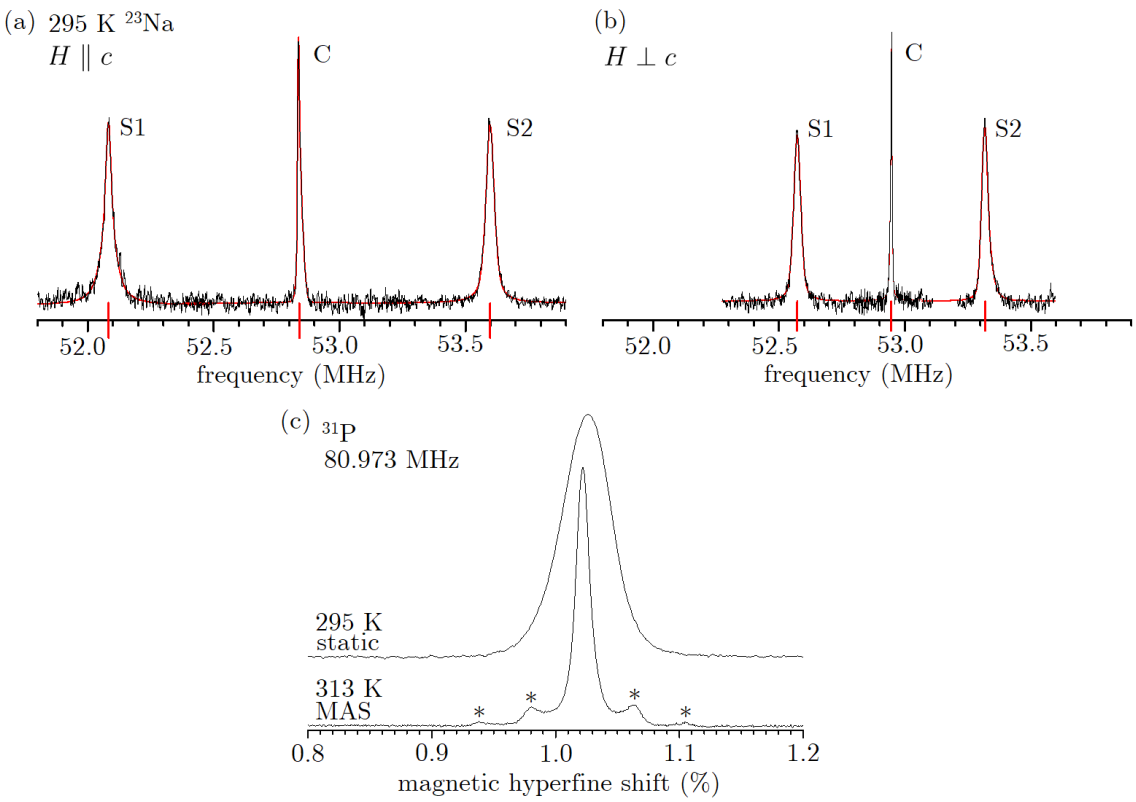

Figure 4.16.: NMR spectra at room temperature. (a) and (b) ^{23}Na NMR spectra for the magnetic field of 4.7 T parallel and perpendicular to c, respectively. The satellites are broader than the central line. (c) The static and MAS ^{31}P NMR spectra show a single line. The spinning side lines are marked with asterisks. Measurements by Ivo Heinmaa and Raivo Stern.

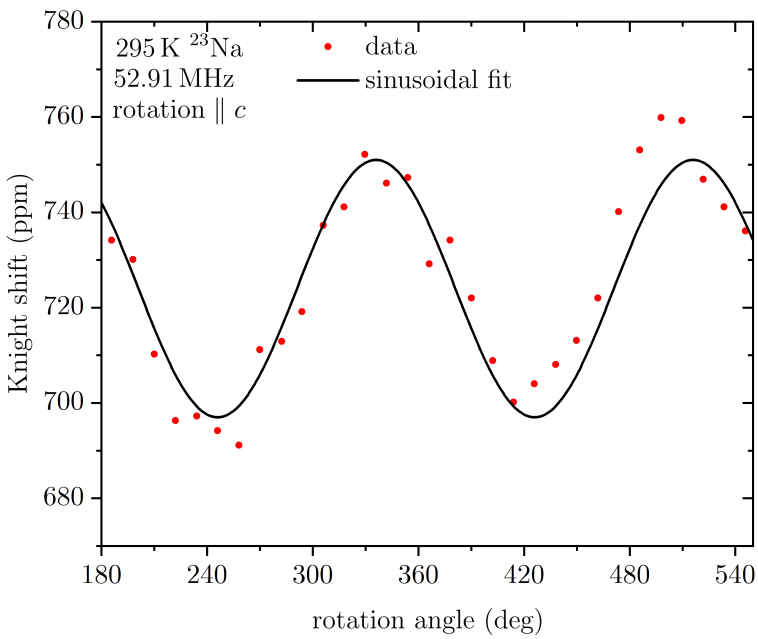

Figure 4.17.: Angular dependence of the ^{23}Na Knight shift at room temperature. Shown is the hyperfine shift of the central transition in the *ab* plane. The single crystal was rotated around the *c* axis. Measurements by Ivo Heinmaa and Raivo Stern.

4.3.3. Magnetization

In $Na_2BaCo(PO_4)_2$ the magnetic Co^{2+} ions with the electronic configuration d^7 are in an octahedral environment. The $^4T_1$ dodecet in the high-spin case splits in the presence of SOC into the lowest lying doublet with effective spin 1/2 and higher lying levels with effective spin 3/2 and 5/2. The change of the occupation with temperature is observable in the temperature dependence of the inverse susceptibility (see Fig. 4.18) which shows a deviation from the linear behavior and a point of inflection at around 70 K. At this temperature the excited state with effective spin 3/2 becomes increasingly populated. At low temperatures $Na_2BaCo(PO_4)_2$ can be treated as spin-1/2 system because the lowest-lying doublet is accessed only. The model from Griffith [119] describes the effective magnetic moment in dependence of the temperature for d^7 high-spin octahedral complexes [119]. The SOC constant is the only free parameter in the model and fitting the model to the data yields the SOC constant 785(8) K. The SOC constant is in good agreement with the literature value of around 766 K [16]. The model describes the data accurately and is given in Fig. 4.18.

Hence, the susceptibility at low temperatures is governed by the effective spin-1/2 system only and is given in Fig. 4.19 for both field directions, $H \perp c$ and $H \parallel c$. No phase transition is visible down to 400 mK. The Curie-Weiss fits in Figs. 4.19(a) and 4.19(c) between 5 and 20 K describe the data accurately. The choice of the temperature range is a trade-off. The temperature must be high

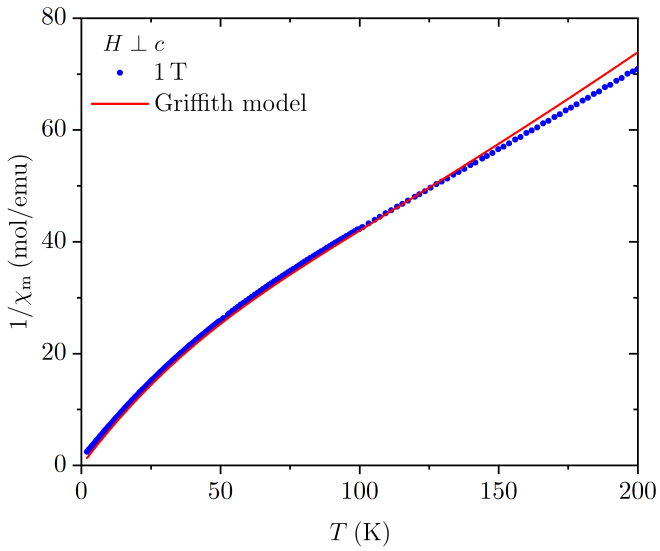

Figure 4.18.: The inverse magnetic susceptibility data of $Na_2BaCo(PO_4)_2$ measured at 1 T show an inflection point at around 70 K. The data are accurately described by the Griffith model given in Ref. [119].

enough to enter the paramagnetic state but low enough to stay in the regime where the system can be described with the effective spin-1/2. The fits yield the Curie-Weiss temperature $\theta_{CW} = -2.52(2)$ K, the Landé factor $g = 4.80(1)$, the Van-Vleck contribution $\chi_0 = 9.9(3) \cdot 10^{-3}$ emu/mol for $H \parallel c$ and $\theta_{CW} = -1.66(2)$ K, $g = 4.16(1)$, $\chi_0 = 8.4(2) \cdot 10^{-3}$ emu/mol for $H \perp c$. The Curie-Weiss temperatures and g values are in very good accordance with the values reported in the literature [16, 114, 117, 118]. With $\theta_{CW} = 1.5J/k_B$ for nn TLAFs $J_z/k_B = 1.68(1)$ K and $J_{xy}/k_B = 1.11(2)$ K. The g anisotropy is 13%, which is in agreement to the g anisotropy of 12% obtained from $M(H)$ measurements. $M(H)$ and the g anisotropy will be discussed and compared to $Na_2SrCo(PO_4)_2$ in Subsec. 4.4.4.

The broad hump visible in the magnetic susceptibility [see Figs. 4.19(b) and (d)] is indicative for short-range magnetic order typical of low-dimensional systems or frustrated antiferromagnets [122]. The susceptibility of spin-1/2 TLAFs can be fitted with a Padé approximated high-temperature series expansion [120, 121]. The fits describe the data accurately and are given in Figs. 4.19(b) and (d). g and the exchange coupling J are the free parameters and by fitting the data below 20 K collected at 0.1 T $J_z/k_B = 1.40(2)$ K and $g = 4.87(2)$ for $H \parallel c$ and $J_{xy}/k_B = 1.05(1)$ K and $g = 4.27(1)$ for $H \perp c$ are obtained. The g values, J_z, and J_{xy} are in good accordance to the values determined from the Curie-Weiss fits. The accuracy of the model, which assumes only Heisenberg nn interactions, shows that J_{xy} and J_z are the leading interactions and the off-diagonal anisotropy can be assumed to be small. Also extensive numerical calculations reported in Ref. [117] show that off-diagonal anisotropy is negligible.

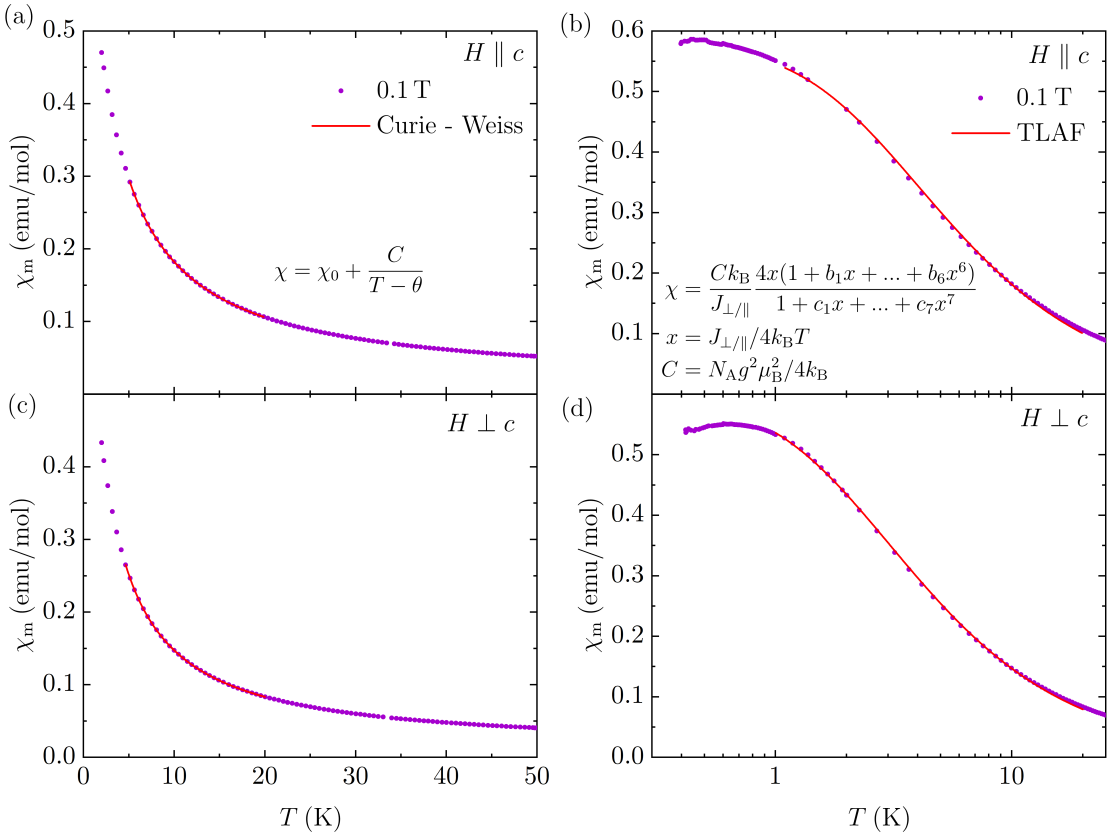

Figure 4.19.: Magnetic susceptibility of $Na_2BaCo(PO_4)_2$ for the magnetic field parallel to c (top row) and for the magnetic field perpendicular to c (bottom row). No phase transition down to 400 mK is visible. [(a) and (c)] Susceptibility up to 50 K and Curie-Weiss fits between 5 and 20 K. [(b) and (d)] Short-range magnetic order manifests itself in the broad hump which is described accurately with the high-temperature series expansion for TLAFs given in Refs. [120, 121].

4.3.4. Heat Capacity

The total heat capacity in zero magnetic field between 1 and 20 K is shown in Fig. 4.20(a). To extract the phonon contribution the data in an intermediate temperature range were fitted with $B \cdot T^3 + A/T^2$. The first term accounts for the phonon contribution and the second term is the lowest-order term in the high-temperature series expansion for the magnetic heat capacity [123]. The fit is shown in Fig. 4.20(a) and the two parameters $B = 6.6(1) \cdot 10^{-4}\,\mathrm{J/(K^4 \cdot mol)}$ and $A = 4.3(2)\,\mathrm{J \cdot K/mol}$ were obtained. With $A = (9/16) \cdot R \cdot (J/k_B)^2$ for nn TLAFs $J/k_B = 0.96(2)$ K results, which fits well to the average value $J_{av}/k_B = (2J_{xy} + J_z)/3k_B = 1.17(2)$ K and 1.30(2) K obtained in Subsec. 4.3.3 from the TLAF fit and the Curie-Weiss temperature, respectively.

The magnetic heat capacity after subtraction of the phonon contribution is given in Fig. 4.20(b). The data below 400 mK were collected in a dilution fridge by Noah

Winterhalter-Stocker. The specific heat of TLAFs were calculated in the theory paper Ref. [124] for the cases of the simple nn, the nnn, and the distorted TLAF. The best match with the measured data was obtained by using the model of the simple nn TLAF. The modeled heat capacity for a TLAF with the exchange interaction $J/k_B = 1.28\,\mathrm{K}$ is superimposed on the data in Fig. 4.20(b). The exchange coupling fits well to the average values obtained from the magnetization measurements. Additionally, the height was corrected by a factor of 0.95. This takes account of the weighing error which is with 5% reasonable for the small sample sizes.

Clearly visible is a magnetic phase transition at 147(2) mK in form of a sharp peak. The transition temperature is in good accordance to the value reported in Ref. [114]. The data presented here also challenges the picture of a QSL candidate and contradicts the findings of Refs. [4, 113] reporting the absence of long-range magnetic order down to 50 mK.

Interesting fact is that the magnetic heat capacity in zero field levels out at around $0.68\,\mathrm{J/(K \cdot mol)}$ for the lowest temperatures. The magnetic heat capacity necessarily has to approach zero for $T \to 0$. A nuclear Schottky contribution to the heat capacity with the relation $1/T^2$ of the high-temperature tail fails to explain the deviating behavior. Since the extrapolation of the data to zero is not clearly possible the integration to obtain the entropy is unfeasible. Yet, the flat course of the graph suggests a non-trivial behavior of the heat capacity and maybe another anomaly at a temperature not accessible with the dilution fridge. This idea of a second transition comes from further measurements in low magnetic fields parallel to c. The

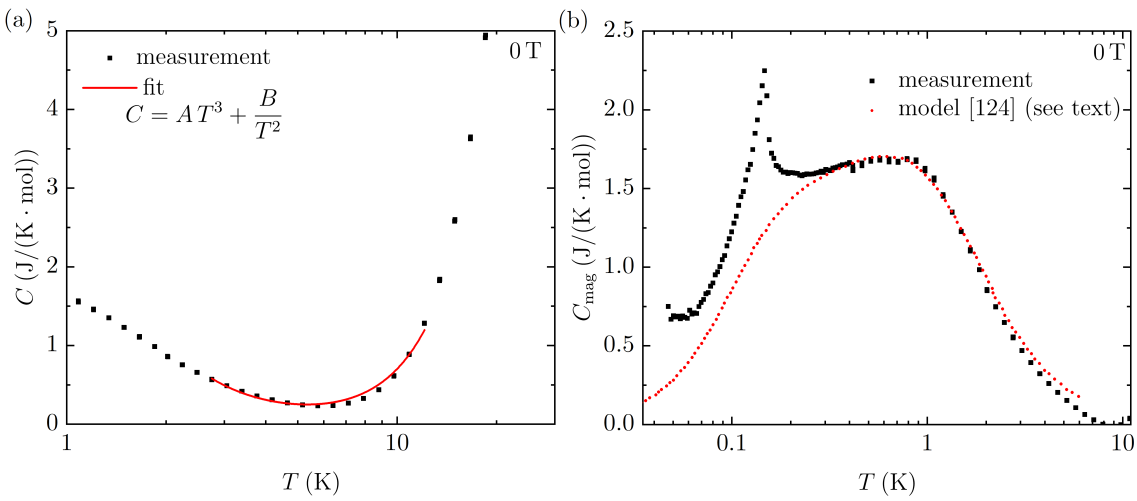

Figure 4.20.: Heat capacity of $Na_2BaCo(PO_4)_2$ in zero magnetic field. (a) The total heat capacity and fit including the phonon contribution ($\propto T^3$) and the high-temperature limit of the magnetic specific heat ($\propto 1/T^2$). (b) Magnetic part of the heat capacity after subtraction of the phonon contribution. A clear transition is visible at 147(2) mK. The red line depicts the heat capacity of a nn TLAF with the exchange interaction $J/k_B = 1.28\,\mathrm{K}$. The data below 400 mK were collected by Noah Winterhalter-Stocker.

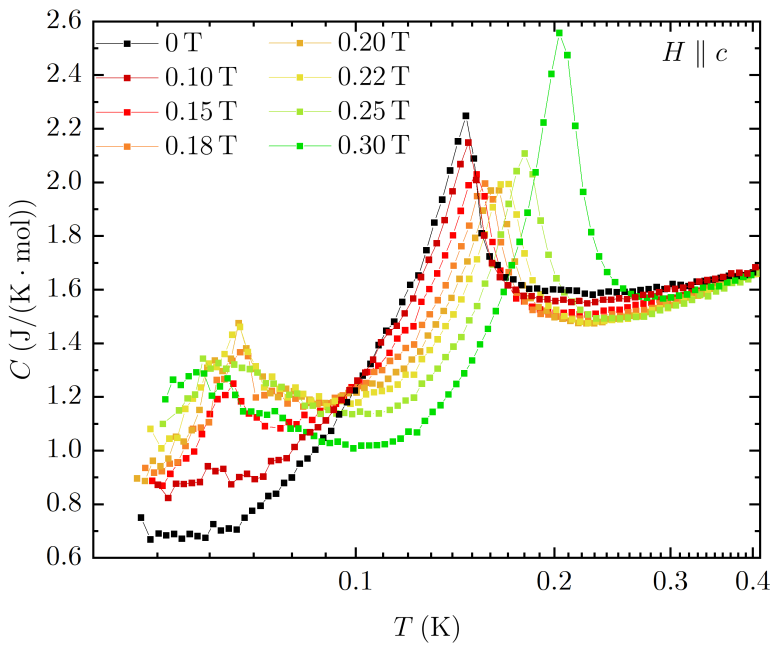

Figure 4.21.: Milli-Kelvin heat capacity of $Na_2BaCo(PO_4)_2$ in zero and low magnetic fields parallel to c. Within a small field pocket another phase transition can be observed at around 66 mK. Measurements by Noah Winterhalter-Stocker.

measurements at fields between 0 and 0.3 T are shown in Fig. 4.21. Within a small field pocket from 0.15 to 0.22 T a clear second phase transition at around 66 mK can be observed. This transition smears out if the field is increased further. The transition temperature shows a slight downward trend with decreasing field. For the magnetic fields above 0.18 T the transition temperature is 67 mK and is slightly reduced to 65 mK at 0.15 T. Similar to the zero-field data, the heat capacity shows no transition and stays constant for a small field of 0.10 T. To see if the decreasing trend of the transition temperature continues below 0.15 T further measurements between 0.1 and 0.15 T would be desirable.

4.3.5. Discussion

First, the structure of $Na_2BaCo(PO_4)_2$ is addressed. The CoO_6 octahedra are slightly distorted, which leads to the deviation of the O-Co-O angle from the ideal 90 °. At 10 K the two O-Co-O angles are 93.43(13) and 86.57(13) °. These trigonal distortions lead to the splitting of the isotropic value of $g = 4.33$ into g_{xy} and g_z with a small g anisotropy of 12%. The g anisotropy is further compared to $Na_2SrCo(PO_4)_2$ in Subsec. 4.4.4 and Sec. 4.5.

The $P\overline{3}m1$ structure reported in the literature was revised to $P\overline{3}$. The still enhanced value of the refined ADP of Na and the distribution of the quadrupolar interaction observed in the ^{23}Na spectrum are clear indications of intrinsic struc-

tural dynamics. It is conceivable that structural dynamics in form of rotations of the Co octahedra are present. The octahedral rotations change the geometry of the cage containing the Na ion and explain the in-plane displacements of Na away from the 3-fold symmetry axis observed experimentally. The O1 atoms have the same x, y coordinates as the Na atoms (see Fig. 4.13) which pull on O1 leading to enhanced displacements of O1 as well. Larger displacements are connected to larger rotation angles possible at higher temperatures. Below 50 K the Na displacements freeze as indicated by the ADPs of Na and O1 which become constant below 50 K and that is connected to a spread of the relative rotation angles of the octahedra. The randomness of the frozen rotations may lead to different exchange paths and a distribution of the exchange couplings.

Structural disorder can influence the properties tremendously. One famous example is the rare earth triangular lattice compound $YbMgGaO_4$. The $T^{2/3}$ dependence of the heat capacity and the excitation continuum observed in inelastic scattering point towards a QSL ground state. However, the thermal conductivity lacks any magnetic contribution as would be expected for itinerant spinons. Supposedly, site disorder in $YbMgGaO_4$ creates a disordered magnetic sublattice and the QSL behavior is only mimicked [125–130]. It was also shown for the triangular-lattice Heisenberg model that defects can destroy long-range magnetic order and instead a glassy state emerges [131].

Back to $Na_2BaCo(PO_4)_2$, the debate described in the introduction of this section if a QSL-like state above T_N exists, is also triggered by contradictory experimental results. The heat capacity in Ref. [4] and Ref. [114] starts to deviate from each other around 1 K. The thermal conductivity is crucially different in Ref. [114] and Ref. [116]. This can be possibly traced back to differences in the samples. Imaginable are unequal amounts of disorder in the structure due to differences in the synthesis or due to different cooling rates causing individual freezing of the structural dynamics. Different degrees of structural randomness could also explain the discrepancy between Ref. [114] and Ref. [113] reporting the formation of long-range magnetic order at 148 mK and a dynamically fluctuating ground state down to 80 mK, respectively. This thesis needs of course further proof and it is essential to characterize the structural disorder carefully and connect it to the measured results to understand its impact on the properties.

Concerning the discussion if $Na_2BaCo(PO_4)_2$ can be described with an easy-axis XXZ model [117, 118] or if additional interactions like Kitaev interactions are present [16], the analysis of the thermodynamic properties herein clearly points towards an easy-axis TLAF described by the XXZ model. The broad hump visible in the magnetic susceptibility can be fitted with a TLAF model including Heisenberg interactions only. Fitting the direction dependent susceptibility yields a slight easy-axis anisotropy $J_z/J_{xy} = 1.33(4)$, which is consistent with the ratio $J_z/J_{xy} = 1.51(4)$ obtained from the Curie-Weiss fits. The theoretically and experimentally determined anisotropy parameter reported in the literature is with $J_z/J_{xy} = 1.7$ slightly higher [117, 118]. Also the magnetic heat capacity is accurately described by a nn Heisenberg TLAF model [124]. The broad hump is typically observed for frustrated

systems forming short-range order with spin fluctuations.

The phase diagrams for magnetic fields parallel and perpendicular to c obtained from heat capacity, thermal expansion, magnetostriction and magnetocaloric measurements will be subject in the dissertation of Noah Winterhalter-Stocker. It should only be noted here, that the overall phase diagrams agree with the published ones [118] and are consistent with the theoretical phase diagrams for XXZ model TLAFs. Additional field-induced phases were detected for the magnetic field parallel to c (see Subsec. 4.3.4) and perpendicular c.

The model from Ref. [117] predicts a transition at 150 mK in zero magnetic field, which is experimentally confirmed. Interestingly, a second Berezinskii-Kosterlitz-Thoueless transition in zero magnetic field around 50 mK was predicted. So far, this transitions lacks experimental proof since the temperature lies below the temperatures accessed in previous measurements. Given the heat capacity data presented herein, a second phase transition would not be surprising although the transition is expected below 50 mK. Of course further measurements below 50 mK are indispensable to verify this conjecture.

4.4. $Na_2SrCo(PO_4)_2$

The balance of competing interactions is influenced by subtleties of the crystal structure which, in turn, command the quantum state of matter. Undistorted TLAFs, for example $Ba_3CoSb_2O_9$ with a high symmetry ($P6_3/mmc$), show a single plateau phase at one third of the saturation magnetization which corresponds to the up-up-down magnetic phase [132]. Cs_2CuBr_4 with the orthorhombic space group $Pnma$ in contrast has a distorted triangular lattice. The DM interactions allowed in this setting are suspected to be, together with a spatially anisotropic exchange, the reason for the stabilization of multiple plateau phases [133–136].

Also the non magnetic ions can affect the properties. To realize a magnetic 2D system in a bulk material, non-magnetic buffer layers separate the magnetic layers. The thickness of the non-magnetic layers sets the distance between the magnetic layers and dictates the 2D character of the system. The effect was investigated by increasing the non magnetic layer thickness between the Co layers from $Ba_3CoNb_2O_9$ to $Ba_8CoNb_6O_{24}$, which leads to an over 2.5 times larger interplanar Co-Co distance in the latter compound. As a consequence, the two successive phase transitions observed in $Ba_3CoNb_2O_9$ are suppressed in $Ba_8CoNb_6O_{24}$ and the heat capacity shows a single broad feature [137, 138].

In the following, a chemical sibling of $Na_2BaCo(PO_4)_2$, the new $Na_2SrCo(PO_4)_2$ compound is presented. Instead of increasing the number of non magnetic layers between the Co layers, the Ba ions are replaced by Sr ions. Substituting the Ba ions with the smaller Sr ions does not only lead to the expected smaller interplanar Co-Co distance but also has a decisive impact on the symmetry. In contrast to the trigonal symmetry of $Na_2BaCo(PO_4)_2$ at room temperature, the monoclinic symmetry of $Na_2SrCo(PO_4)_2$ is described with the space group $P2_1/a$. High resolution synchrotron XRPD reveals a trigonal high temperature phase for temperatures above 1025 K. The structure does not transform from $P2_1/a$ to the trigonal symmetry directly but passes through the intermediate monoclinic $C2/m$ phase which forms at 650 K. The triangular spin lattice is weakly deformed in the monoclinic case and the monoclinic symmetry allows small distortions of the CoO_6 octahedra beyond the trigonal deformations commonly found in the glaserite type structures. The symmetry lowering of the CoO_6 octahedra manifests itself in the enhanced g-tensor anisotropy for $Na_2SrCo(PO_4)_2$ ($g_z/g_{xy} = 1.6$) compared to $Na_2BaCo(PO_4)_2$ ($g_z/g_{xy} = 1.1$). Additionally, despite the same average coupling strength $J_{av}/k_B = (2J_{xy} + J_z)/3k_B \simeq 1.3$ K, a larger XXZ anisotropy of $J_z/J_{xy} = 2.1$ for $Na_2SrCo(PO_4)_2$ compared to $J_z/J_{xy} = 1.5$ for $Na_2BaCo(PO_4)_2$ was extracted from the magnetization data. The above listed differences lead to the over four times higher Néel temperature of 600 mK in $Na_2SrCo(PO_4)_2$ compared to 140 mK in $Na_2BaCo(PO_4)_2$ and a sizable uncompensated moment of $0.066(4)\mu_B$/f.u. in the plane was detected. In the following, the distortions of the crystal structure are captured and their impact on the observed thermodynamic properties is revealed by comparing the two Co compounds.

4.4.1. Room-temperature Crystal Structure

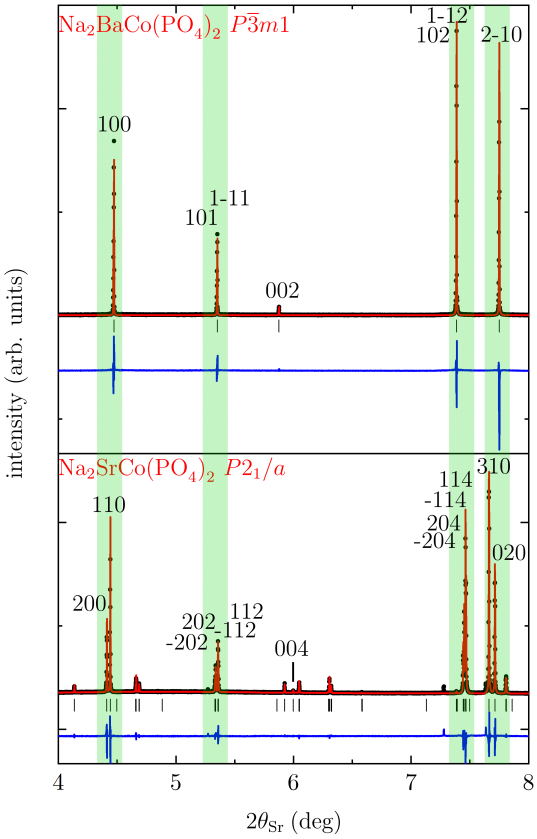

Figure 4.22.: Comparison of the Rietveld refinement for the synchrotron XRPD data of $Na_2BaCo(PO_4)_2$ and $Na_2SrCo(PO_4)_2$ at 300 K. The peak splitting in the case of $Na_2SrCo(PO_4)_2$ indicates the lower monoclinic symmetry in contrast to the trigonal symmetry of $Na_2BaCo(PO_4)_2$. For a better comparison of the two data sets the scattering angles for $Na_2BaCo(PO_4)_2$ were renormalized. The same graph was used in our publication [139], which is copyrighted by the American Physical Society.

Fig. 4.22 contrasts the synchrotron XRPD data for $Na_2BaCo(PO_4)_2$ and $Na_2SrCo(PO_4)_2$ collected at 300 K. From the peak splitting it becomes apparent that in contrast to $Na_2BaCo(PO_4)_2$, which crystallizes in a trigonal symmetry, $Na_2SrCo(PO_4)_2$ has a monoclinic symmetry. To create a structural model in the monoclinic setting, the basis vectors of the $Na_2BaCo(PO_4)_2$ structure were transformed as follows: $\vec{a}' = \vec{a} - \vec{b}$, $\vec{b}' = \vec{a} + \vec{b}$, and $\vec{c}' = 2\vec{c}$. The refined lattice parameters at 300 K for $Na_2SrCo(PO_4)_2$ are $a = 9.20152(2)$ Å, $b = 5.26593(1)$ Å, $c = 13.54116(2)$ Å, and $\beta = 90.06613(12)$ °.

From the extinction conditions the possible space groups can be narrowed down. A primitive space group is expected and the extinction rules point towards an a glide plane and a 2_1 screw axis $\parallel \vec{b}$ as present symmetry elements. Rietveld refinement proves the correctness of the space group $P2_1/a$ (No. 14). It is noted that the Co1 atom and not a spacer ions as in the case of $Na_2BaCo(PO_4)_2$ is located at the origin of the unit cell. An additional origin shift of (0 0 0.5) was needed to derive the structural model for $Na_2SrCo(PO_4)_2$ from the initial $Na_2BaCo(PO_4)_2$ structure.

In addition to the powder measurements, single crystal x-ray diffraction experiments performed by Jan Langmann confirm the structural model. The single crystal exhibited triple twinning first. A single domain crystal was obtained after cutting the sample. The reconstructed reciprocal space planes, the refined atom-

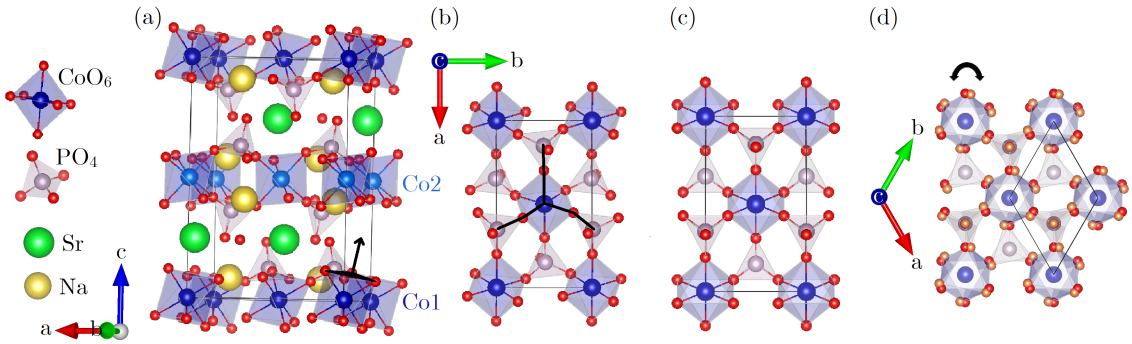

Figure 4.23.: Crystal structure of $Na_2SrCo(PO_4)_2$. (a) Unit cell of $Na_2SrCo(PO_4)_2$. The Co layers are stacked along c and separated by non magnetic layers. The tilting of the CoO_6 octahedra referred to in the text is sketched with the black arrow. (b) Top view perspective of the unit cell with the low-temperature monoclinic symmetry $P2_1/a$. The triangular lattice is formed by the CoO_6 octahedra. The Co-O-P bonds referred to in the text are indicated in black. (c) Triangular layer in the unit cell with the intermediate symmetry $C2/m$. (d) Triangular layer in the unit cell with the high-temperature symmetry $P\overline{3}m1$. For clarity, the Na^+ and Sr^{2+} ions were omitted in (b) to (d). The same graph was used in our publication [139], which is copyrighted by the American Physical Society.

ic coordinates and displacement parameters at room temperature are included in Appendix A. While completing this work the room-temperature monoclinic space group $P2_1/a$ was confirmed in Ref. [140] which further reports thermodynamic properties measured on polycrystalline samples down to 2 K.

Figs. 4.23(a) and (b) depict the unit cell of $Na_2SrCo(PO_4)_2$. As in $Na_2BaCo(PO_4)_2$ a planar triangular lattice is formed by CoO_6 octahedra. The CoO_6 octahedra are connected in-plane by PO_4 tetrahedra. The voids are filled with Na^+ ions. The magnetic Co layers are stacked along the crystallographic c axis and are separated by the non magnetic spacer ions. The buffer layer determines the distance between the magnetic layers. As expected, the smaller Sr^{2+} ions lead to the smaller interplanar Co-Co distance of 6.77 Å compared to 7.01 Å in $Na_2BaCo(PO_4)_2$.

After the description of the similarities, the differences responsible for the lower monoclinic symmetry of $Na_2SrCo(PO_4)_2$ will be addressed next. The cooperative tilting of the CoO_6 octahedra and PO_4 tetrahedra is one of the main reasons for the symmetry lowering. Additionally, in the $P2_1/a$ crystal structure distortions of the CoO_6 octahedra are allowed. The distortions lower the local symmetry of the Co^{2+} ion from S_6 in $P\overline{3}$ $Na_2BaCo(PO_4)_2$ to C_i in $Na_2SrCo(PO_4)_2$. The symmetry of the PO_4 tetrahedra is reduced from C_3 to C_1. The trigonal distortions can be quantified through the deviation of the O-Co-O angle from 90 °. The deviation is 6.0(3)% and 7.9(3)% for the $Co1O_6$ and $Co2O_6$ octahedra, respectively. $Na_2BaCo(PO_4)_2$ shows a lower trigonal distortion of 4.8(2)%. Distortions beyond trigonal are absent in $Na_2BaCo(PO_4)_2$ but cause three different Co-O lengths in $Na_2SrCo(PO_4)_2$. This distortion is captured by the largest deviation from one of the the Co-O distances

to the mean length of the three Co-O distances. The distortions amount to 1.5(7)% in the $Co1O_6$ octahedra and to 2.2(7)% in the $Co2O_6$ octahedra. Both tilting and distortion are different in adjacent layers and lead to a doubled unit cell along c.

Also the geometry of the triangular lattice is different in the two compounds. Whereas in $Na_2BaCo(PO_4)_2$ the triangular lattice is composed of equilateral triangles, the triangles forming the triangular lattice in $Na_2SrCo(PO_4)_2$ are isosceles. One of the Co-Co distance is around 0.7% shorter with regard to the two other Co-Co distances of equal length.

4.4.2. Structural Phase Transitions

Several aspects point towards a structural phase transition at higher temperatures. As chemical sibling of $Na_2BaCo(PO_4)_2$, the trigonal symmetry may be restored at higher temperatures in $Na_2SrCo(PO_4)_2$. The monoclinic to trigonal phase transition was already reported for various glaserite-type compounds [141–145]. An additional hint towards a structural phase transition is the triple twinning observed in the single crystal x-ray diffraction. During the synthesis $Na_2SrCo(PO_4)_2$ crystallizes in a higher symmetry at higher temperatures and when the sample is cooled down the structure transforms into monoclinic.

To detect structural phase transitions, temperature dependent synchrotron XRPD measurements were performed between 10 and 1025 K [146, 147]. The temperature dependent lattice parameters are given in Figs. 4.24(a) and (c). The data will be discussed from low to high temperatures. At 200 K a first small anomaly is visible in the monoclinic angle β. However, at this temperature an anomaly is seen neither in the a, b, c lattice parameters nor in the susceptibility (Fig. 4.27) nor in Fisher's heat capacity [inset of Fig. 4.24(a)]. In this temperature region the sample environment was changed from the He cryostat to the N_2 cryostream, which probably causes the measurement artifact.

At 650 K a, b, and β exhibit significant anomalies and a structural phase transition can be identified. The comparison of the synchrotron XRPD data collected below the transition at 500 K and above the transition at 800 K is given in Fig. 4.24(b). The symmetry remains monoclinic. The disappearing reflections are labeled in black. The unit cell of the new phase should be C centered as apparent from the new extinction condition $h + k = 2n$. Since the volume of the unit cell does not show a discontinuity at 650 K [inset of Fig. 4.24(c)] the transition is of second order. Hence, the group-subgroup relation should hold and the space group $C2/m$ is a potential description of the structure with the highest possible symmetry. Indeed, Rietveld refinement shows that the structural model describes the data above 650 K accurately. The Rietveld refinement for the exemplarily chosen data at 800 K and the refined atomic parameters are given in Appendix A. The top view perspective of the unit cell is illustrated in Fig. 4.23(c). In $P2_1/a$ the CoO_6 octahedra within one layer show the same absolute tilting angle but the translational symmetry element (0.5 0.5 0) is not allowed because the b components of the tilting vector have opposite sign. However, in $C2/m$ the unit cell is C-centered. The b component of the

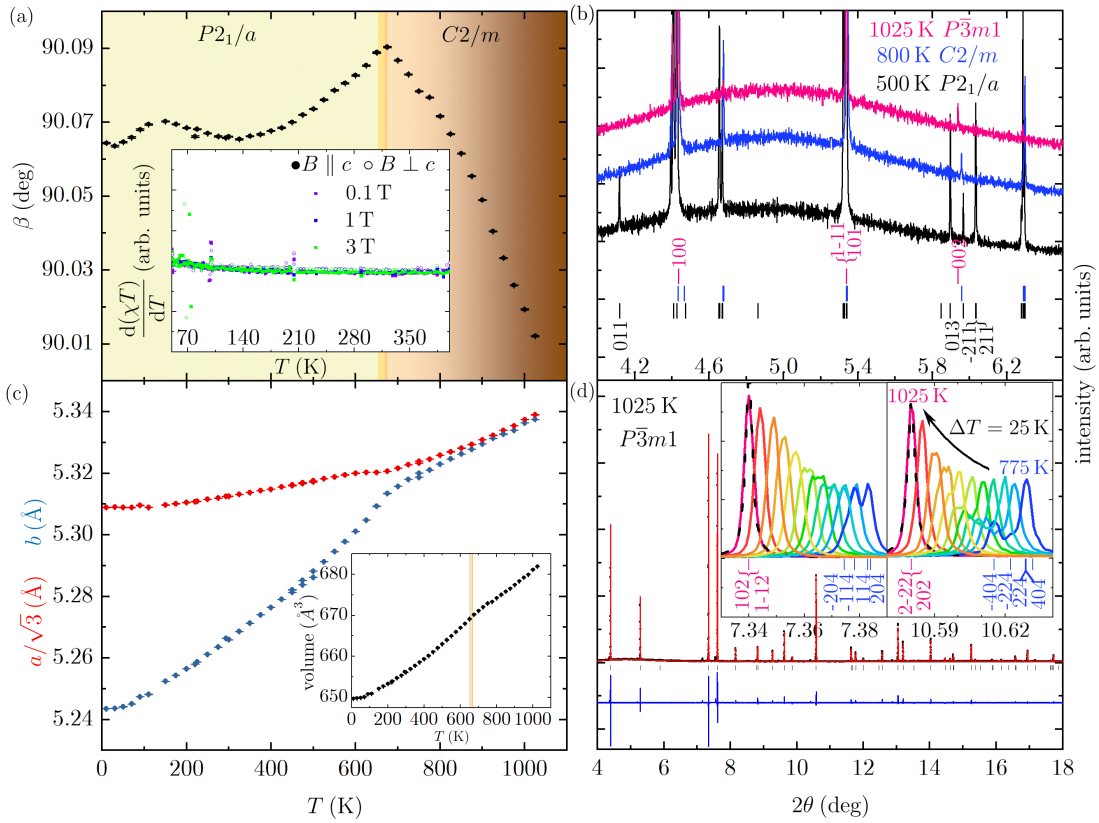

Figure 4.24.: Temperature dependence of the crystal structure of $Na_2SrCo(PO_4)_2$. (a) Monoclinic angle β as function of temperature. The inset shows Fisher's heat capacity $d(\chi T)/dT$. The weak anomaly of β at 200 K is seen neither in Fisher's heat capacity nor in the thermodynamic measurement data and can be assigned to a measurement artifact. The first structural phase transition from $P2_1/a$ to $C2/m$ manifests itself in the anomaly at around 650 K. The gradual structural transition into a trigonal phase is not fully completed at 1025 K and is indicated by the color gradient. (b) Exemplarily chosen synchrotron PXRD data of each structural phase are contrasted. The symmetry changes are evident from the peak merging. The reflections which disappear during the symmetry change from $P2_1/a$ to $C2/m$ are labeled in black. The remaining reflections in the case of $P\bar{3}m1$ are labeled in red. For a better comparison the scattering angles were rescaled to those of the measurement at 500 K. (c) The refined lattice parameters $a/\sqrt(3)$ and b in dependence of the temperature are given in red and blue, respectively. The phase transition at around 650 K from $P2_1/a$ to $C2/m$ is observed in both parameters as kink. Above 650 K $a/\sqrt(3)$ and b gradually converge and thus indicate the smooth transition into a trigonal structure. The monotonous increase of the volume of the unit cell with increasing temperature is given in the inset. (d) The synchrotron PXRD data collected at 1025 K can already be described with the trigonal space group $P\bar{3}m1$. The gradual merging of the split peaks with increasing temperature is given in the insets. The same graph was used in our publication [139], which is copyrighted by the American Physical Society.

tiling vector is zero which confines the tilting to the ac plane and all the octahedra tilt the same way. The unit cell is still doubled in the c direction. The structural phase transition from $P2_1/a$ to $C2/m$ is reversible upon cooling.

At the beginning of this subsection aspects pointing towards a trigonal symmetry at higher temperatures were listed. The space group $C2/m$ was reported as intermediate structure in the $P2_1/a$ to $P\bar{3}m1$ transition series in the glaserite-type compound $Na_2SrMg(PO_4)_2$ [148]. Indeed, upon increasing the temperature further, the lattice parameters $a/\sqrt{(3)}$ and b converge and the monoclinic angle β approaches 90 ° as illustrated in Figs. 4.24(a) and (c). This indicates a transition into a trigonal phase. The transition sequence is illustrated in Fig. 4.24(b). From $C2/m$ to $P\bar{3}m1$ many split peaks merge and the remaining reflections for $P\bar{3}m1$ are labeled in red. For selected peaks the merging with temperature is shown in the inset of Fig. 4.24(d). The peaks merge with increasing temperature and at 1000 K the peak splitting cannot be resolved anymore. The restrictions $a/\sqrt{(3)}$ equals b and β equals 90 ° are imposed by symmetry. Since β equals 90.0122(2) ° and has not reached 90 ° at 1025 K the transition may not be complete. However, the space group $P\bar{3}m1$ can already be used as structural model if the residual broadening is taken into account during the refinement. Considering an increased reflection width, the diffraction data can be described accurately [see Fig. 4.24(d)]. The residue value for the trigonal refinement $R_p = 9.36\%$ is only slightly higher than the residue value of the refinement for the same data set in the monoclinic structure ($R_p = 8.59\%$). Same holds for the Lorentzian parameter of the peak-shape function LY. For the refinement in the trigonal space group LY is 0.0412(2) ° and for the refinement in the monoclinic space group LY is 0.0352(2) °. At 1025 K $Na_2SrCo(PO_4)_2$ is at the threshold of the transition to a trigonal structure but the transition is not yet completed. Unfortunately, measurements at higher temperatures could not be performed due to technical reasons. The atomic parameters obtained through the refinement with the trigonal space group $P\bar{3}m1$ are listed in Appendix A.

Fig. 4.23(d) illustrates the $P\bar{3}m1$ unit cell. In contrast to the monoclinic structures at lower temperatures, the trigonal structure is undistorted and in the trigonal case the polyhedra are not tilted. Fig. 4.23(d) indicates the ferrorotations of the CoO_6 octahedra which can be easily introduced in the trigonal structure. The average structure recorded by the x rays is the $P\bar{3}m1$ structure.

In the following, the evolution of the distortions and tilting with temperature will be analyzed. The distortion of the triangular lattice is captured through the ratio of the nn Co-Co distances. This ratio of the short (d') and long (d) Co-Co distance with temperature is given in Fig. 4.25(a). The difference between d' and d increases upon cooling. At the phase transition to $C2/m$ at 650 K the slope changes. The ratio approaches 1.0 but does not reach 1.0, which would be imposed by the trigonal symmetry. The triangles are nearly equilateral but the trigonal symmetry is still forbidden due to the distortions.

The tilting of the CoO_6 octahedra which is referred to now is indicated with a black arrow in Fig. 4.23(a). Here, the tilting angle is defined as the angle between the crystallographic c axis and the vector perpendicular to the indicated face of the

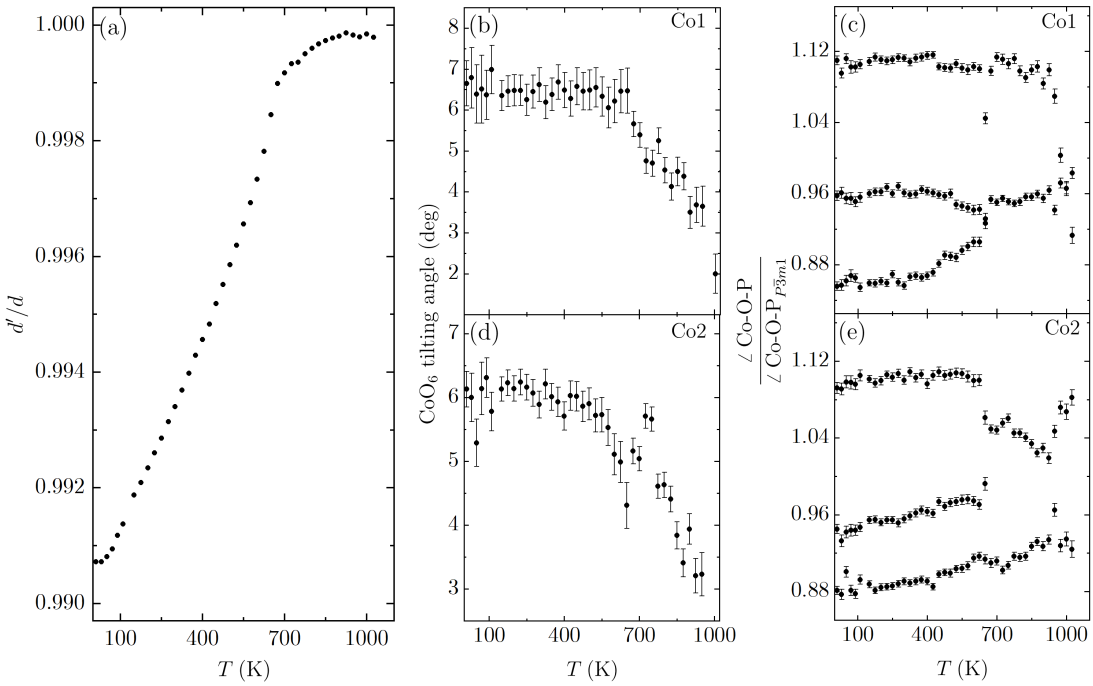

Figure 4.25.: Distortion and tilting in $Na_2SrCo(PO_4)_2$. (a) The deformation of the triangular lattice is captured by the ratio of the short (d') to the long (d) Co-Co distances. The deformation is larger the lower the temperature. The error bars are smaller than the symbol size. [(b) and (d)] The tilting angles of the $Co1O_6$ and $Co2O_6$ octahedra stay nearly constant in the $P2_1/a$ symmetry and start to decrease at the phase transition to $C2/m$. [(c) and (e)] Three different Co-O-P angles are present in each layer in the case of the lowest symmetry $P2_1/a$. Two of those angles in each layer merge at the phase transition to $C2/m$. The trigonal symmetry restricts the angles to be equal and the angle in the trigonal case was used for normalization. The same graph was used in our publication [139], which is copyrighted by the American Physical Society.

octahedron. The temperature dependence is given in Figs. 4.25(b) and 4.25(d). In both Co layers, the tilting angle is the highest in the $P2_1/a$ space group and stays nearly constant in the temperature window of the $P2_1/a$ structure. The phase transition to the $C2/m$ structure is visible as drop of the tilting angle at around 650 K. The angle keeps decreasing and at 1000 K reaches half of the starting value of 3 °. The tilting angle would vanish if the undistorted $P\overline{3}m1$ phase were reached.

The detailed analysis of the orientation of the polyhedra is essential not only in regard of a complete structural characterization but also in regard of the magnetic properties. Because there is no direct Co-O-Co link the magnetic exchange is mediated through the Co-O-P units which are delineated in Fig. 4.23(b). The Co-O-P bond angles are influenced by the tilting of the CoO_6 octahedra and PO_4 tetrahedra. The evolution of the Co-O-P bond angles with temperature is given in Figs. 4.25(c) and 4.25(e). Without tilting as in the $P\overline{3}m1$ case, all the angles are identical. The angle obtained from the refinement for the data at 1025 K in the space group $P\overline{3}m1$ is used for normalization. In contrast to only one value in the $P\overline{3}m1$ case, three different angles are present in the $P2_1/a$ structure which lead to different superexchange paths. Again, at the lowest temperature the values deviate the most from the reference value. The spread of the angles decreases if the temperature is increased. The first phase transition is indicated by the convergence of two angles in each Co layer and one is left with two different angles in both layers in the $C2/m$ structure. These two angles would finally merge at the phase transition to $P\overline{3}m1$.

4.4.3. Heat Capacity

The total heat capacity in dependence of the temperature is given in Fig. 4.26(a). To obtain the magnetic heat capacity the phonon contribution has to be extracted. Therefore, the zero-field data were fitted between 2.5 to 10 K to the expression $B \cdot T^3 + A/T^2$. Due to the light weight of the single crystal the extraction of the specific heat from the relaxation curves becomes difficult above 6 K and is not possible anymore above 10 K. Anyway, the data collected above 10 K would not be suited for fitting because the phonon contribution would start to deviate from Debye's T^3 law, which makes up the first term of the fit function. The second part is the lowest-order term in the high-temperature series expansion for the magnetic specific heat [123]. The fit parameters are $B = 2.6(2) \cdot 10^{-4}\,\mathrm{J/(K^4 \cdot mol)}$ and $A = 8.3(1)\,\mathrm{J \cdot K/mol}$. For nn TLAFs $A = (9/16) \cdot R \cdot (J/k_\mathrm{B})^2$ holds and thus $J/k_\mathrm{B} = 1.33(1)\,\mathrm{K}$ is obtained. This value is in good accordance to those determined in Subsec. 4.4.4.

The magnetic specific heat obtained by subtracting the phonon contribution from the total heat capacity in different magnetic fields is given in Fig. 4.26(b). Long-range magnetic order in zero magnetic field is observed in form of a sharp peak at around $T_N \simeq 600\,\mathrm{mK}$. T_N initially stays constant upon increasing the magnetic field but at 0.4 T T_N decreases to 520 mK. Further increase of the magnetic field leads to a suppression of the transition below 0.4 K or a complete vanishing of magnetic order.

Besides the sharp transition a broad hump is centered around 1 K up to 1 T. This

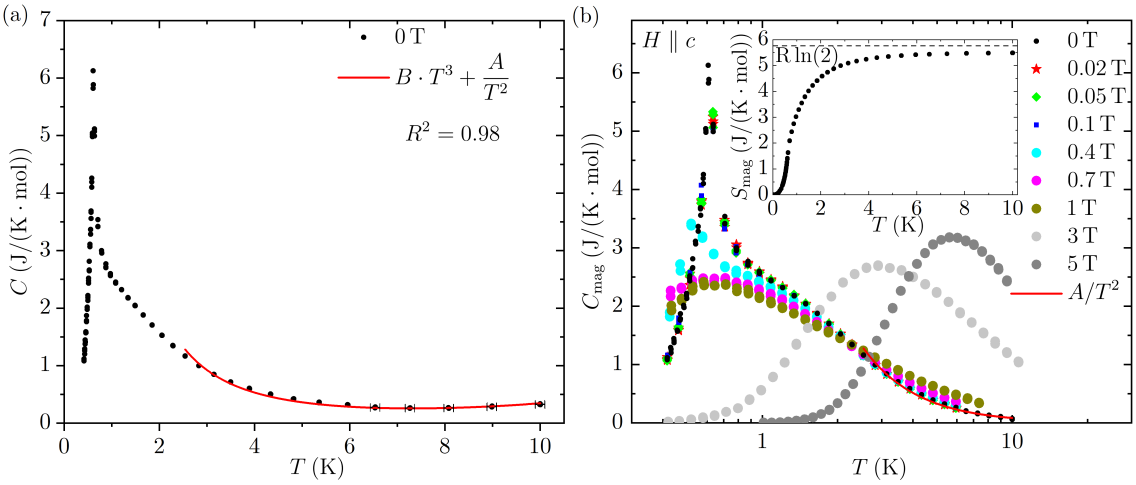

Figure 4.26.: Temperature dependent specific heat of $Na_2SrCo(PO_4)_2$. (a) Total specific heat at 0 T. The fit shown in red includes the phonon contribution and the lowest-order term in the high-temperature series expansion for the magnetic heat capacity. (b) Magnetic heat capacity at different magnetic fields parallel to c. The λ-type peak indicates long-range magnetic order at 600 mK in low magnetic fields. The superimposed broad Schottky-like anomaly is caused by short-range magnetic order. Above 1 T the broad maximum shifts to higher temperatures with increasing magnetic field. The fit of the zero-field data with the high-temperature series expansion is shown in red. The zero-field magnetic entropy given in the inset approaches R ln(2) as expected for an effective spin-1/2 system. The same graph was used in our publication [139], which is copyrighted by the American Physical Society.

broad feature is caused by short-range magnetic order above T_N and commonly observed in low-dimensional and frustrated antiferromagnets. Above 1 T the maximum shifts to higher temperatures with increasing field. This trend resembles the behavior of a Schottky anomaly, which suggests that above 1 T the spin system is fully polarized and a field-induced gap opens. This fits to the saturation field of around 2 T observed in the magnetization data Fig. 4.29.

To obtain the magnetic entropy by integrating the specific heat divided by temperature, the zero field data first have to be extrapolated to 0 K. To this end, a gapless antiferromagnet which follows the proportionality $C \propto T^3$ was assumed. The inset of Fig. 4.26 shows the magnetic entropy. As expected for a spin-1/2 system the entropy value approaches R ln(2). Due to the light weight of the single crystal the weighing error leads to the small deviation of 5%. The asymptotic limit proofs that $Na_2SrCo(PO_4)_2$ carries spin-1/2 magnetic moments below 10 K, similar to $Na_2BaCo(PO_4)_2$. This is further supported by magnetization measurements presented in the next subsection.

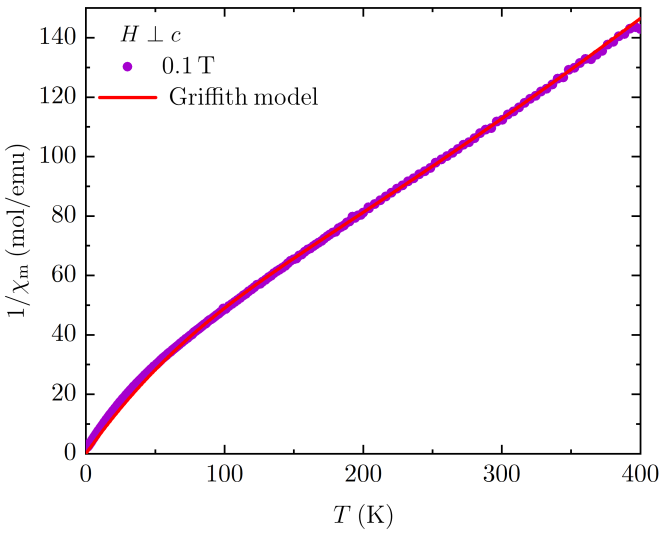

Figure 4.27.: The inverse magnetic susceptibility data of $Na_2SrCo(PO_4)_2$ measured at 0.1 T show an inflection point at around 70 K. The data are accurately described by the Griffith model given in Ref. [119]. The same graph was used in our publication [139], which is copyrighted by the American Physical Society.

4.4.4. Magnetization

Analogous to $Na_2BaCo(PO_4)_2$, the temperature dependence of the inverse magnetic susceptibility given in Fig. 4.27 shows an inflection point at around 70 K. As already discussed in Subsec. 4.3.3, in the case of a d^7 electronic configuration in octahedral coordination SOC leads to a lowest Kramers level with effective spin-1/2 and higher-lying levels with effective spin-3/2 and 5/2. Around 70 K the excited states get significantly populated but at low temperatures the system behaves like an effective spin-1/2 system. This is already known from the magnetic specific heat. The inverse susceptibility can be described accurately with the model from Griffith for d^7 high-spin octahedral complexes as well [119]. For $Na_2SrCo(PO_4)_2$ the obtained SOC constant of 1377(11) K is nearly 2 times larger than in Ref. [16]. In the model from Griffith an ideal octahedral symmetry is assumed, which means the SOC only leads to the splitting of the Co^{2+} multiplet. For $Na_2BaCo(PO_4)_2$ with only trigonal distortions this assumption is still reasonable but for $Na_2SrCo(PO_4)_2$ the model runs into its limits because crystal-field splitting of the t_{2g} levels caused by trigonal distortions plus distortions of the octahedra beyond the trigonal symmetry is not accounted for in the simplified model.

In the following it is focused on the pure spin-1/2 system free of the influence of the excited states which can be assumed below 20 K. The Curie-Weiss fits, $\chi = \chi_0 + C/(T-\theta)$, for both field directions, $H \perp c$ and $H \parallel c$, between 5 and 20 K are given in Figs. 4.28(b) and 4.28(e). The fits yield the Curie-Weiss temperature $\theta_{CW} = -3.07(3)$ K, the Landé factor $g = 5.8(3)$, $\chi_0 = 7.8(5)\cdot 10^{-3}$ emu/mol for $H \parallel c$ and $\theta_{CW} = -1.44(3)$ K, $g = 3.7(2)$, $\chi_0 = 8.5(3)\cdot 10^{-3}$ emu/mol for $H \perp c$. With χ_0

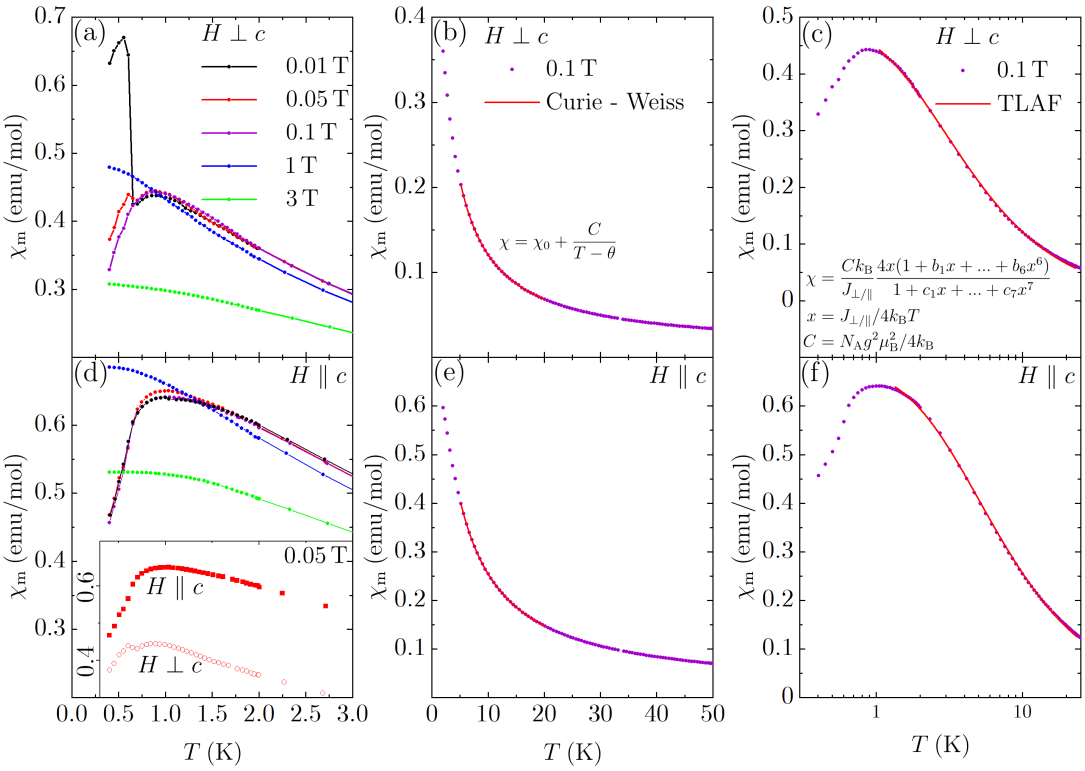

Figure 4.28.: Magnetic susceptibility of $Na_2SrCo(PO_4)_2$ for the magnetic field perpendicular to c (top row) and for the magnetic field parallel to c (bottom row). [(a) and (d)] The susceptibility shows an antiferromagnetic transition at 600 mK for magnetic fields up to 0.1 T. The inset compares the susceptibility at 0.05 T for both field directions and the faster drop of the susceptibility for the field parallel to c indicates c as easy axis. The sharp increase below T_N for $H \perp c$ up to 0.05 T arises from small uncompensated moments in the ab plane. [(b) and (e)] Susceptibility up to 50 K and Curie-Weiss fits between 5 and 20 K. [(c) and (f)] The broad hump is due to short-range magnetic order and can be described accurately with a high-temperature series expansion for TLAFs given in Refs. [120, 121]. The same graph was used in our publication [139], which is copyrighted by the American Physical Society.

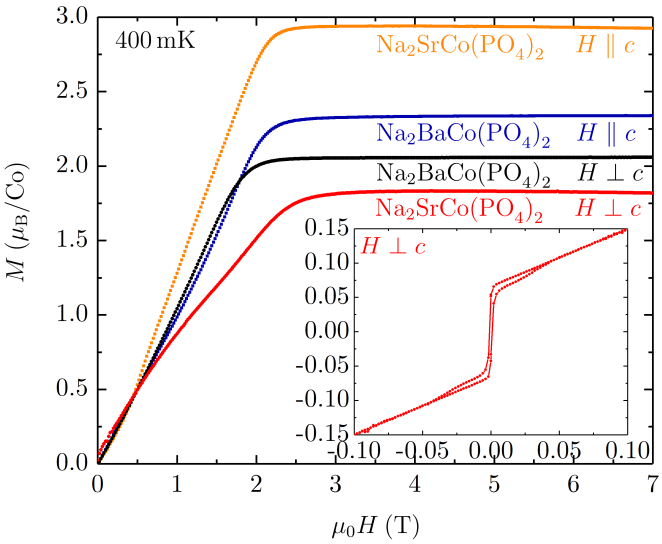

Figure 4.29.: $M(H)$ for $Na_2BaCo(PO_4)_2$ and $Na_2SrCo(PO_4)_2$ at 400 mK for $H \parallel c$ and $H \perp c$. The g anisotropy is three times larger in $Na_2SrCo(PO_4)_2$. The uncompensated moment in the ab plane causes the small hysteresis for $H \perp c$ given in the inset. The same graph was used in our publication [139], which is copyrighted by the American Physical Society.

the Van-Vleck contribution is taken into account. For nn TLAFs $\theta_{CW} = 1.5J/k_B$ holds, which lead to $J_z/k_B = 2.05(3)$ K and $J_{xy}/k_B = 0.96(2)$ K. The average value is $J_{av}/k_B = (2J_{xy} + J_z)/3k_B = 1.32(3)$ K and in perfect accordance with the value obtained from the heat capacity data. From the substantial difference of the g values the anisotropy is found to be around 37%. From the saturation magnetization $M_s = g\mu_B J$, at 0.4 K $g = 5.9(3)$ for $H \parallel c$ and $g = 3.7(2)$ for $H \perp c$ were determined leading to a similar value of the anisotropy. In contrast, with $g = 4.7(3)$ for $H \parallel c$ and $g = 4.1(2)$ for $H \perp c$ determined from the saturation magnetization, $Na_2BaCo(PO_4)_2$ shows a much smaller anisotropy of 12% (see Fig. 4.29). The isotropic value of $g = 4.33$ would be expected for an effective spin-1/2 within an undistorted CoO_6 octahedron. Distortions of the octahedra lead to a difference between g_z and g_{xy}. The small deviations from the isotropic value in $Na_2BaCo(PO_4)_2$ can be traced back to the trigonal distortions of only 3.8% at 10 K. The larger g anisotropy in $Na_2SrCo(PO_4)_2$ is on the one hand due to the larger trigonal distortions of around 5.4% ($Co1O_6$) and 8.8% ($Co2O_6$) and on the other hand due to the distortions beyond trigonal of around 2.6% ($Co1O_6$) and 2.9% ($Co2O_6$) at 10 K.

The temperature dependent susceptibility shows that $Na_2SrCo(PO_4)_2$ orders antiferromagnetically at 600 mK [see Fig. 4.28(a) and (d)]. The transition was already observed in the heat capacity data. The transition is still observed at 0.1 T and is no longer visible at 1 T, in agreement with the heat-capacity data. At the lowest fields measured the behavior below the transition temperature is strongly dependent on the direction of the applied magnetic field. For $H \parallel c$ the susceptibility decreases,

whereas for $H \perp c$ the susceptibility increases abruptly. A direct comparison of the susceptibility for the two different field directions is given in the inset of Fig. 4.28(d). The behavior is that of an easy-axis antiferromagnet. If the field is applied along the easy axis the susceptibility drops and if the field is applied perpendicular to the easy axis the susceptibility stays independent of temperature. Together with $g_z > g_{xy}$ and the stronger exchange couplings for $H \parallel c$, c can be identified as easy axis. While the spin component along c is fully compensated, the abrupt increase in the susceptibility for $H \perp c$ indicates an uncompensated spin component in the ab plane. An example for this kind of behavior can be found in Refs. [149, 150]. The uncompensated moment should manifest itself in form of a hysteresis in $M(H)$. Indeed, a hysteretic behavior was measured and is given in the inset of Fig. 4.29. From the saturation magnetization the in-plane moment $\mu_{Co^{2+}} = 0.066(4)\mu_B$/f.u. was determined. This corresponds to 3.5% of the out-of-plane saturated moment measured for $B \perp c$. In XXZ TLAFs with a large easy-axis anisotropy the Y-type order is expected [151]. The easy-axis anisotropy and the small uncompensated moment in the ab plane is compatible with the Y-type order if the Y-type spin pattern is turned toward the ab plane. Yet, for the exact determination of the spin structure neutron diffraction experiments are needed.

Nonlinearities are discernible in $M(H)$ collected at 400 mK for both field directions of the magnetic field. These may indicate field induced phases, similar to the uud phase observed through the magnetization plateau at one third of the saturation magnetization in other TLAFs. To resolve possible intermediate phases, measurements at lower temperatures would be necessary but go beyond the scope of this work.

As for $Na_2BaCo(PO_4)_2$ (Subsec. 4.3.3) a broad hump due to short-range magnetic order is seen in the magnetic susceptibility [see Figs. 4.28(c) and (f)]. In analogy to $Na_2BaCo(PO_4)_2$, the susceptibility was fitted with the Padé approximated high-temperature series expansion for spin-1/2 TLAFs described in Refs. [120, 121]. The fit parameters g and the exchange coupling J are obtained to $J_z/k_B = 1.76(1)$ K and $g = 5.9(2)$ for $H \parallel c$ and $J_{xy}/k_B = 1.04(1)$ K and $g = 3.9(1)$ for $H \perp c$ by fitting to the data below 25 K collected at 0.1 T. The g values are in good accordance to those determined from the Curie-Weiss fits and from the $M(H)$ data. J_z and J_{xy} match the values obtained from the Curie-Weiss fits and the average $J_{av}/k_B = 1.28(1)$ K fit to the value determined from the heat capacity. The fits describe the data accurately and are given in Figs. 4.28(c) and (f). The model does not take off-diagonal anisotropy into account and similar to $Na_2BaCo(PO_4)_2$, the off-diagonal anisotropy is expected to be small.

4.5. Comparison of $Na_2BaCo(PO_4)_2$ and $Na_2SrCo(PO_4)_2$

Strong differences of the physical properties are sometimes linked to fine details of the crystal structure. First, the structural differences of $Na_2BaCo(PO_4)_2$ and $Na_2SrCo(PO_4)_2$ will be compared before conclusions can be drawn concerning the particular properties. The most obvious and not surprising aspect is the decreased Co-Co interlayer distance in $Na_2SrCo(PO_4)_2$ compared to $Na_2BaCo(PO_4)_2$ due to the smaller atomic radii of Sr^{2+} compared to Ba^{2+}. The over 3% smaller Co-Co interlayer distance at 10 K in $Na_2SrCo(PO_4)_2$ should lead to an increased interlayer coupling. Additionally, the spacer ions have a remarkable effect on the symmetry and lower the symmetry from trigonal in $Na_2BaCo(PO_4)_2$ to monoclinic in $Na_2SrCo(PO_4)_2$. To understand the origin of the different structural characteristics the environments of the spacer ions will be compared. To this end, the bond valence sum (BVS) was calculated. The valence of the alkaline-earth metal is obtained by summing over the valence of the individual bonds to the surrounding O^{2-} ions which depends on the bond length. Ref. [152] lists the needed empirical constants. The resulting BVS is given in Table 4.3 together with the average bond length and the effective coordination. The latter is the mean coordination which is obtained similar to the BVS by summing over the surrounding atoms with a weight depending on the Sr-O distance. The smaller Sr ions are coordinated by only nine O ions whereas the Ba ions are coordinated by ten O ions. Hence, the average bond length has to be smaller in the SrO polyhedra to preserve the oxidation state of +2 of the central ion. This in turn results in the tilt and distortion of the octahedra and leads to the lower symmetry. At higher temperatures, the average bond length is increased and the ten-fold coordination allows the formation of the undistorted structure.

The deviations from the ideal octahedral symmetry in $Na_2SrCo(PO_4)_2$ explain why the Griffith model overestimates the SOC constant. The Griffith model for d^7 high-spin octahedral complexes presented in Subsecs. 4.3.3 and 4.4.4 and Figs. 4.18 and 4.27 yields a reasonable SOC constant for $Na_2BaCo(PO_4)_2$ but the SOC con-

Table 4.3.: Comparison of the SrO and BaO polyhedra in $Na_2SrCo(PO_4)_2$ and $Na_2BaCo(PO_4)_2$. The table is adapted from Ref. [139].

	BVS	effective coordination	average bond length (Å)
$Na_2SrCo(PO_4)_2$ 300 K, $P2_1/a$	2.033	9.0	2.7255
$Na_2SrCo(PO_4)_2$ 1025 K, $P\bar{3}m1$	1.678	9.8	2.8932
$Na_2BaCo(PO_4)_2$ 300 K, $P\bar{3}m1$	2.398	10.5	2.9141

Table 4.4.: Comparison of Néel temperature T_N and average exchange coupling strength J_{av}/k_B for different spin-1/2 TLAFs. For the Co and Cu compounds the average exchange was calculated with $J_{av}/k_B = (2J_{xy} + J_z)/3k_B$ and $J_{av}/k_B = (J + 2J')/3k_B$, respectively. The table is adapted from Ref. [139].

	T_N (K)	J_{av}/k_B (K)	$k_B T_N/J_{av}$
$Na_2BaCo(PO_4)_2$	0.14	1.3	0.11
$Ba_3CoSb_2O_9$ [153]	3.8	19.19	0.20
Cs_2CuBr_4 [154, 155]	1.4	9.0	0.16
Cs_2CuCl_4 [156]	0.62	2.42	0.26
$Na_2SrCo(PO_4)_2$	0.60	1.32	0.45

stant obtained for $Na_2SrCo(PO_4)_2$ is too large by a factor of around two. Griffith assumes in his model an ideal octahedral symmetry and distortions leading to crystal field splittings are not taken into account. Therefore, the model is suited to describe the susceptibility data of $Na_2BaCo(PO_4)_2$ but reaches its limits for $Na_2SrCo(PO_4)_2$.

The occurrence of uncompensated moments in the *ab* plane in $Na_2SrCo(PO_4)_2$ can also be traced back to the symmetry lowering. This weak ferromagnetism in antiferromagnets typically stems from DM interactions which are controlled by the bond inversion symmetry. A necessary condition for DM interactions to occur is the absence of bond inversion symmetry. In $Na_2BaCo(PO_4)_2$ every Co-Co bond has an inversion center, hence, DM interactions are not allowed. In contrast, the lower symmetry in $Na_2SrCo(PO_4)_2$ removes the inversion symmetry for two of the three Co-Co bonds and DM interactions become possible. With DM interactions present in the system the tilting of the spins relative to each other is energetically favorable and non-collinear spin arrangements accompanied with uncompensated moments may emerge.

The larger g-tensor anisotropy is another ramification of the symmetry lowering. In general, g is a tensor but reduces to a single value in the isotropic case. For the undistorted CoO_6 octahedron $g = 4.33$. Distortions destroy the isotropy, which leads to the splitting of the parallel and perpendicular components of the g tensor [157]. Besides the increase of the g-tensor anisotropy, the XXZ anisotropy is enhanced. From the Curie-Weiss temperatures the anisotropy parameters were calculated. The anisotropy parameter of $Na_2SrCo(PO_4)_2$ is $\Delta = J_z/J_{xy} = 2.05(3)\,\mathrm{K}/0.96(2)\,\mathrm{K} = 2.14(8)$, whereas $Na_2BaCo(PO_4)_2$ shows a lower value of $\Delta = J_z/J_{xy} = 1.68(1)\,\mathrm{K}/1.11(2)\,\mathrm{K} = 1.51(4)$. The latter value is in good accordance with the caluculated value from Ref. [117].

The Néel temperature in relation to the average exchange coupling $k_B T_N/J_{av}$ is listed in table 4.4 for $Na_2BaCo(PO_4)_2$, $Na_2SrCo(PO_4)_2$, and other spin-1/2 TLAFs. In comparison to other compounds which usually show values around 0.2, the ratio for $Na_2BaCo(PO_4)_2$ is halved and the ratio for $Na_2SrCo(PO_4)_2$ is doubled. Even though the exchange couplings are very similar in the two compounds, the Néel tem-

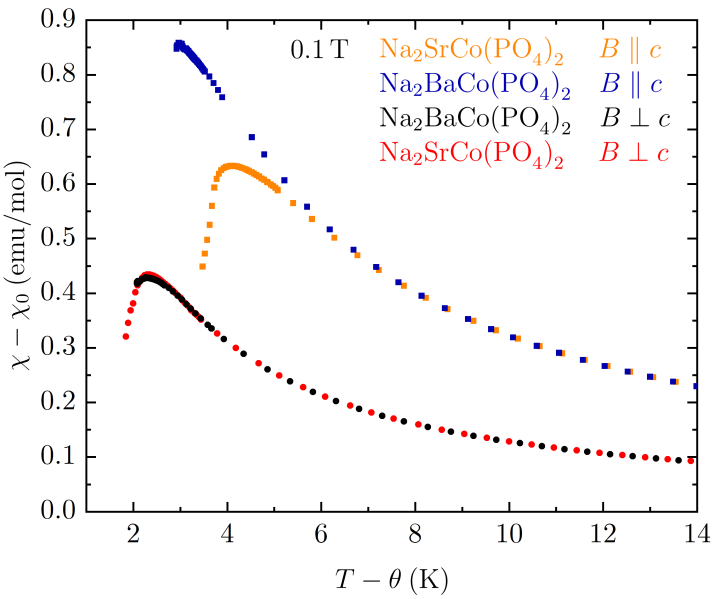

Figure 4.30.: Comparison of the magnetic susceptibilities of $Na_2SrCo(PO_4)_2$ and $Na_2BaCo(PO_4)_2$. The data were collected at 0.1 T for both field directions and rescaled to match the paramagnetic regimes. The susceptibilities clearly start to deviate at low temperatures. The same graph was used in our publication [139], which is copyrighted by the American Physical Society.

perature is larger in $Na_2SrCo(PO_4)_2$ by a factor of over four. Three combined effects, already described above, can explain this difference. First contribution leading to the larger T_N is the stronger interlayer coupling in $Na_2SrCo(PO_4)_2$. Second effect is the deformation of the triangular spin lattice in $Na_2SrCo(PO_4)_2$, as compared to the triangular lattice with equilateral triangles in $Na_2BaCo(PO_4)_2$. Third, quantum fluctuations are weakened by the enhanced XXZ anisotropy. The 120 ° Y-type order is compatible with the easy-axis anisotropy if one of the spins is oriented along the c axis [151]. With increasing J_z/J_{xy} this order becomes more stable. In summary, the small monoclinic distortions have a significant effect on the Néel temperature of TLAFs and for $Na_2SrCo(PO_4)_2$ the ratio $k_B T_N/J_{av}$ is higher than in other TLAFs. In comparison the ratio is lower in $Na_2BaCo(PO_4)_2$. A possible explanation would be that, contrary to $Na_2SrCo(PO_4)_2$, the structural distortions in $Na_2BaCo(PO_4)_2$ presented in Subsec. 4.3.1 reduce T_N. The structural dynamics freeze at lower temperatures and thus introduce randomness of the magnetic interactions.

The magnetic susceptibilities of $Na_2BaCo(PO_4)_2$ and $Na_2SrCo(PO_4)_2$ are directly compared in Fig. 4.30. The data were rescaled to match the paramagnetic regime. The deviations between the two compounds become prominent at low temperatures and are the largest for $H \parallel c$. This indicates a stronger easy-axis anisotropy in $Na_2SrCo(PO_4)_2$ and suggests that the spins are primarily aligned along c in the magnetically ordered state.

5. Summary and Outlook

5.1. Na_2RuO_3

For this compound a few questions remain open. First, a short overview of the findings is given. The open tasks are addressed afterwards.

In a two step approach powder samples of Na_2RuO_3 were obtained by reducing the precursor compound Na_2RuO_4. Na_2RuO_3 could not be synthesized directly. Na_2RuO_3 crystallizes in a monoclinic symmetry. The Ru ions form a honeycomb lattice and the honeycomb layers separated by Na layers are stacked along the crystallographic c axis. Due to the weakly coupled slabs the structure is prone to stacking faults leading to broad asymmetric features in the XRPD pattern. The XRPD pattern was simulated assuming 30% of stacking faults.

No phase transition was observed in the heat capacity and magnetic susceptibility down to 2 K. Moreover, no indications for the presence of local magnetic moments could be detected. The magnetic susceptibility was modeled considering a Van Vleck contribution. The analysis points towards a non-magnetic $J = 0$ ground state. In the case of a $J = 0$ ground state excitations to the higher lying $J = 1$ and $J = 2$ levels should be spectroscopically observable. IRIXS measurements (by Hakuto Suzuki and Bernhard Keimer) indeed revealed four transitions up to 1 eV. The transition energies are comparable to those of the $J = 0$ compound Ca_2RuO_4. The results presented herein clearly point towards the $J = 0$ ground state but not towards an antiferromagnet or a correlated metal as presented before in the literature.

Single crystals could not be synthesized so far but are highly desirable. Polarization dependent IRIXS measurements could provide information about the nature of the transitions and underpin the $J = 0$ scenario. The compound can then be investigated with regard to excitonic magnetism. But the synthesis of single crystals proved to be difficult. Because of thermal decomposition single crystals can not be obtained by simply melting the powder. Moreover, the two step process is not a suitable synthesis method for single crystals. With the defects in form of stacking faults it is not clear if single crystals of sufficient quality could form.

The stacking faults introduce randomness in the system. Spin-glass behavior was not observed, probably because no local magnetic moments are present in this material, but the influence of the stacking faults on the properties needs to be investigated. So far, the amount of stacking faults could not be controlled during the synthesis. The samples synthesized in the framework of this work and the samples reported in the literature all show similar amounts of stacking faults since the same synthesis method was used. Samples with less stacking faults would be necessary to determine the space group ($C2/c$ or $C2/m$) unambiguously.

5.2. Na_3RuO_4

In contrast to Na_2RuO_3 a consistent microscopic scenario could be developed for Na_3RuO_4. Na_3RuO_4 crystallizes in the monoclinic space group $C2/m$. Tetramers composed of two isosceles Ru triangles are arranged on a triangular lattice and triangular features are represented on two different length scales. The two phase transitions observed in the heat capacity at 26 and 29 K were both shown to have magnetic character using elastic neutron scattering. No structural phase transition between 1.5 and 300 K was detected. Magnetic refinement for the data collected at 10 K showed that the tetramers are nearly antiferromagnetic. The magnetic moments of Ru1 and Ru2 are 2.23(3) and 3.04(3)μ_B, respectively. Frustration between the tetramers leads to an incommensurate magnetic order. The propagation vector $\vec{k} = (0.2415(2), 0, 0.3127(2))$ describes the magnetic structure. The propagation vector could be reproduced by the exchange couplings calculated via $ab - initio$ DFT+U (by Alexander A. Tsirlin) and further optimized (by Elias Papke) to better match the experimental propagation vector. If the tetramers are considered as single sites parallels can be drawn to the anisotropic TLAF.

It remains to be shown if the magnetic structure is a helix, expected for an isotropic system, or a spin density wave, expected for an anisotropic system, or a combination of both types. Determination of the anisotropy through direction dependent magnetization measurements on single crystals and scattering experiments with polarized neutrons could shine light on this open question. Furthermore, the magnetic structure forms by passing through two phase transitions. The data collected at temperatures between the two phase transitions were not suited for a refinement and thus it could not be determined if a spin reorientation or the appearance of the second component of the magnetic moment causes the second magnetic transition below T_N.

5.3. $Na_2BaCo(PO_4)_2$

Synchrotron XRPD measurements showed that the published space group $P\bar{3}m1$ had to be revised. In the newly found space group symmetry $P\bar{3}$ the Co octahedra are ferrorotated. No structural phase transition was detected down to 10 K. At 10 K the collective rotation angle is around 9.4(2) °. The slightly enlarged ADPs for Na at every temperature indicate Na in-plane displacements. ^{23}Na NMR (by Ivo Heinmaa and Raivo Stern) confirmed the intrinsic disorder and proved the shift of the Na atoms away from the 3-fold rotation axis. At around 50 K the enlarged ADPs of Na and one of the O atoms become constant indicating the freezing of the structural dynamics.

At low temperatures $Na_2BaCo(PO_4)_2$ can be treated as spin-1/2 system. Heat capacity and magnetic susceptibility could be described accurately with the nn XXZ model for TLAFs. This confirms but also contradicts different reports found in the literature. The transition at 148 mK (measured by Noah Winterhalter-Stocker) clearly excludes $Na_2BaCo(PO_4)_2$ as possible QSL candidate. Heat capacity data revealed a second phase transition at around 66 mK in a small field pocket for small magnetic fields. The behavior of the magnetic heat capacity in zero magnetic field at the lowest temperatures of the measurements hints towards another phase transition.

A possible second phase transition still needs to be confirmed as well as the kind of magnetic structure which was not determined unambiguously so far. Together with the detailed construction of the $H-T$ phase diagrams in both field directions the results can be analyzed with regard to XXZ TLAFs. The thermodynamic properties are subject of active experimental and theoretical research. No attention is given to the structural intrinsic disorder. The presence of disorder was shown in the framework of this work while the exact mechanism of the disorder could not be determined unambiguously. Random rotations of the Co octahedra accompanied by the Na in-plane displacements are conceivable. Whatever kind of disorder is present in the structure, the freezing of the structural dynamics introduces structural randomness and simultaneously randomness of the superexchange paths. The structural randomness may explain the reduced Néel temperature in proportion to the average exchange coupling in comparison to other spin-1/2 TLAFs. Affecting the magnetic properties the details of the crystal structure must be carefully recorded for every sample. Sample dependencies may explain the conflicting results found in the literature.

5.4. $Na_2SrCo(PO_4)_2$ and its Comparison to $Na_2BaCo(PO_4)_2$

Less examined in the literature is $Na_2SrCo(PO_4)_2$. $Na_2SrCo(PO_4)_2$ is formally obtained by exchanging the non-magnetic Ba ions in $Na_2BaCo(PO_4)_2$ with Sr ions. By comparing the two compounds the structural differences can be related to the differences of the properties.

The interlayer ion exchange has a tremendous effect on the symmetry which is lowered to monoclinic $P2_1/a$ in $Na_2SrCo(PO_4)_2$. This results in cooperative tilting of the CoO_6 octahedra and PO_4 tetrahedra, distortions of the CoO_6 octahedra beyond trigonal, and a triangular lattice composed of isosceles triangles instead of equilateral ones. The differences are caused by the smaller atomic radius of the Sr ion. The smaller Sr ions are coordinated by less O ions and to preserve the oxidation state the average Sr-O bond length has to decrease causing the distortions. The average bond length increases at higher temperatures and the trigonal phase is restored at temperatures above 1025 K. An intermediate phase with $C2/m$ symmetry forms at around 650 K. The symmetry lowering entails the lifting of the bond inversion symmetry for some of the Co-Co bonds and DM interactions are allowed.

Direction dependent magnetization measurements showed an antiferromagnetic transition at 600 mK with c as easy axis. DM interactions lead to a small uncompensated moment in the ab plane. As well as in the case of $Na_2BaCo(PO_4)_2$ the heat capacity and magnetization data of $Na_2SrCo(PO_4)_2$ could be explained with the XXZ model for TLAFs. The larger distortions of the CoO_6 octahedra increase the g anisotropy and the XXZ anisotropy. $g_z/g_{xy} = 1.6$ and $J_z/J_{xy} = 2.1$ in $Na_2SrCo(PO_4)_2$ compared to $g_z/g_{xy} = 1.1$ and $J_z/J_{xy} = 1.5$ in $Na_2BaCo(PO_4)_2$. Together with the reduced frustration due to the distortion of the triangular lattice and the increased interlayer coupling the higher anisotropies lead to the four times higher Néel temperature in $Na_2SrCo(PO_4)_2$.

The comparison of $Na_2BaCo(PO_4)_2$ and $Na_2SrCo(PO_4)_2$ illustrates the importance of the detailed investigation of the crystal structure. Consequently, the exact characterization of the structural dynamics in $Na_2BaCo(PO_4)_2$ is indispensable.

A. Appendix

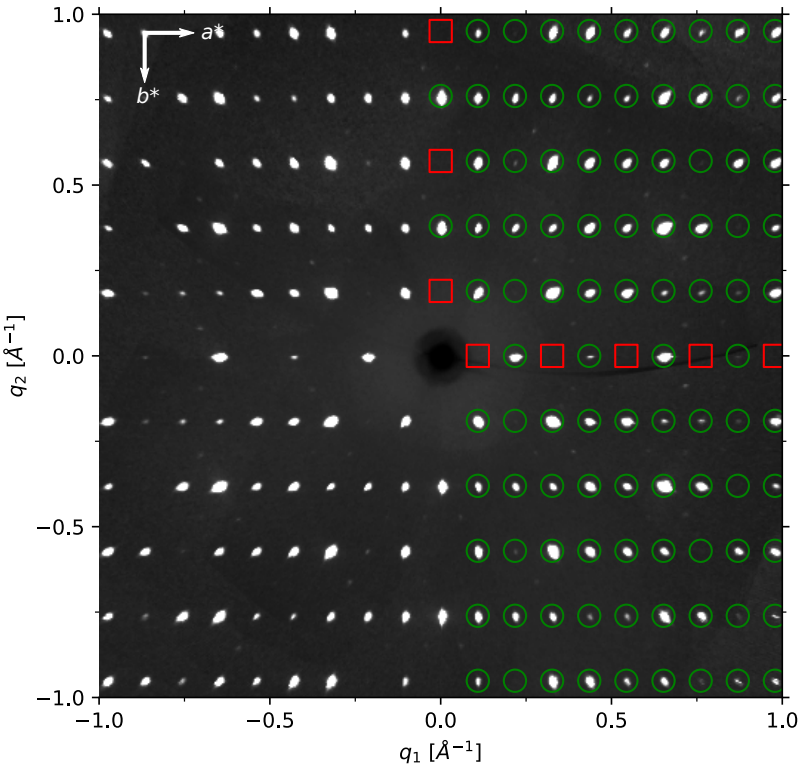

Figure A.1.: Single-crystal x-ray diffraction data collected at room temperature and reconstruction of the $(hk0)$ plane. The allowed reflections are indicated with green circles and the extinct reflections are indicated with red squares. Measurement and refinement by Jan Langmann. The same figure was used in the Supplement of our publication [139], which is copyrighted by the American Physical Society.

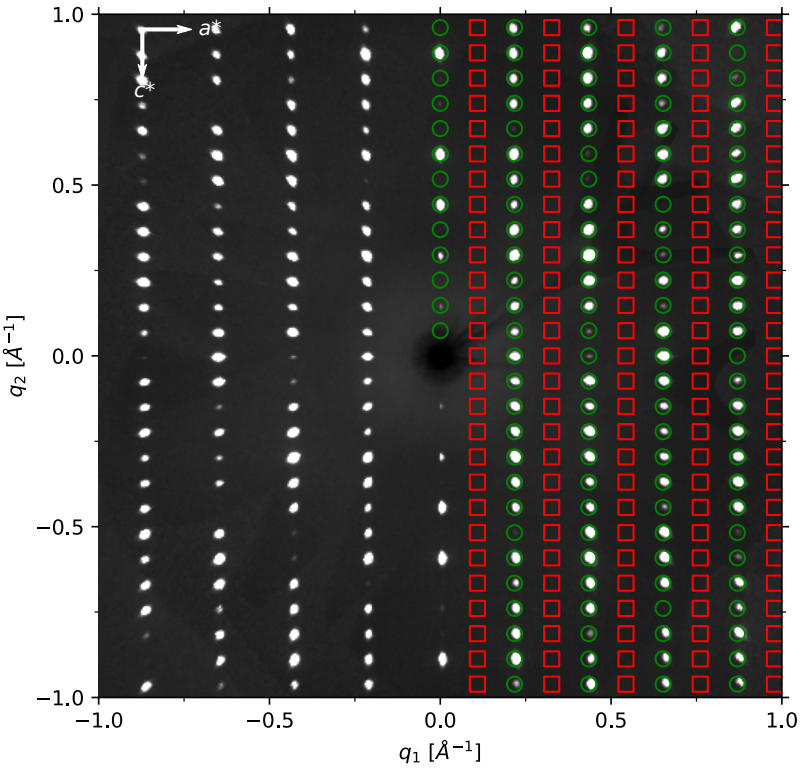

Figure A.2.: Single-crystal x-ray diffraction data collected at room temperature and reconstruction of the $(h0l)$ plane. The allowed reflections are indicated with green circles and the extinct reflections are indicated with red squares. Measurement and refinement by Jan Langmann. The same figure was used in the Supplement of our publication [139], which is copyrighted by the American Physical Society.

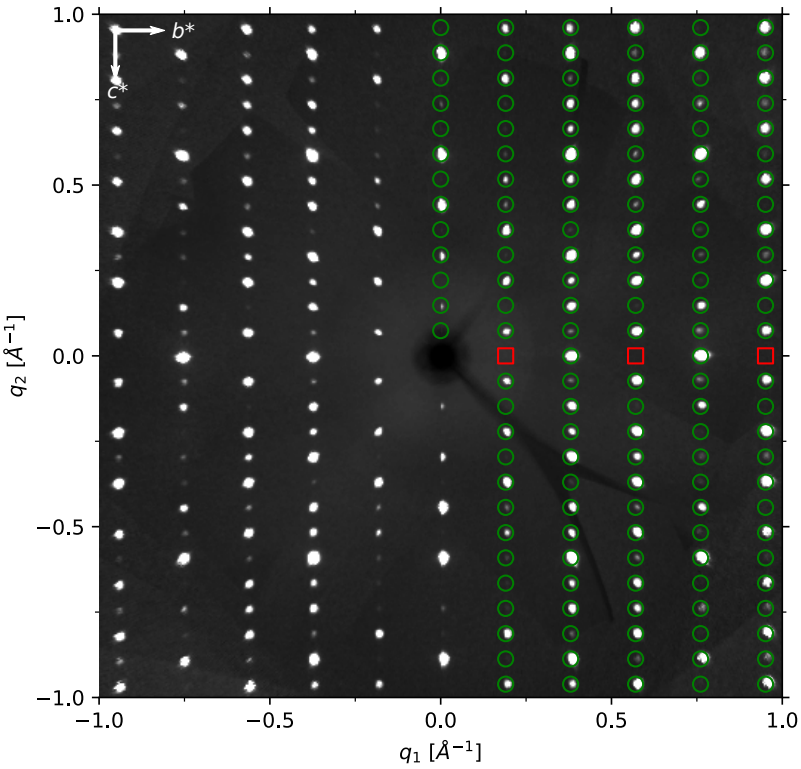

Figure A.3.: Single-crystal x-ray diffraction data collected at room temperature and reconstruction of the $(0kl)$ plane. The allowed reflections are indicated with green circles and the extinct reflections are indicated with red squares. Measurement and refinement by Jan Langmann. The same figure was used in the Supplement of our publication [139], which is copyrighted by the American Physical Society.

Table A.1.: Atomic coordinates and mean-square atomic displacement parameters obtained from refinement with the space group $P2_1/a$. The single-crystal x-ray diffraction data were collected at room temperature and refined by Jan Langmann. The same table was used in the Supplement of our publication [139], which is copyrighted by the American Physical Society.

	fractional atomic coordinates			$\boldsymbol{U}_{\mathbf{eq}}$
atom	x	y	z	[Å^2]
O1	0.70178(9)	0.50090(16)	0.92242(6)	0.01196(15)
O2	0.15411(8)	0.00542(15)	0.38602(6)	0.01000(14)
O3	0.95015(8)	0.30437(14)	0.91005(5)	0.01049(13)
O4	0.41815(7)	0.72734(13)	0.88467(5)	0.00926(12)
O5	0.39957(8)	0.80737(15)	0.41800(6)	0.01240(14)
O6	0.87226(8)	0.21962(15)	0.41167(6)	0.01233(14)
O7	0.82353(10)	0.45621(15)	0.75819(6)	0.01199(16)
O8	0.35195(10)	0.02691(16)	0.25681(6)	0.01270(16)
P1	0.84842(3)	0.50923(4)	0.867019(18)	0.00515(5)
P2	0.31923(3)	0.02805(4)	0.366565(18)	0.00533(5)
Na1	0.81911(7)	0.48619(11)	0.08944(4)	0.01392(12)
Na2	0.34876(7)	0.01638(11)	0.58943(4)	0.01403(12)
Co1	0	0	0	0.00612(4)
Co2	0.5	0.5	0.5	0.00621(4)
Sr1	0.035333(9)	0.042901(17)	0.750259(5)	0.00883(3)

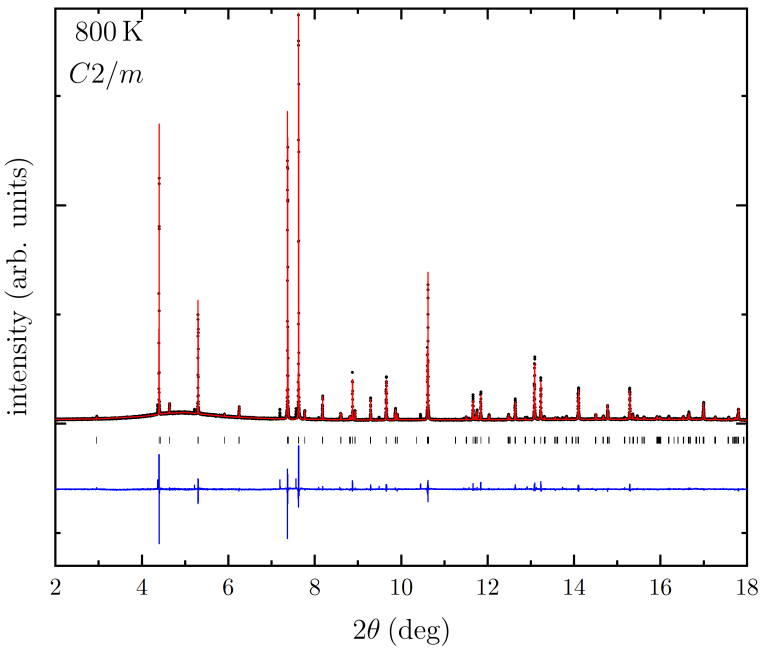

Figure A.4.: Rietveld refinement with the space group $C2/m$. The synchrotron XRPD data were collected at 800 K. The same figure was used in the Supplement of our publication [139], which is copyrighted by the American Physical Society.

Table A.2.: Atomic coordinates and mean-square atomic displacement parameters obtained from refinement with the space group $C2/m$. The synchrotron XRPD data were collected at 800 K. The cell parameters are $a = 9.22467(2)$ Å, $b = 5.32301(1)$ Å, $c = 13.73148(3)$ Å, and $\beta = 90.0717(2)\,°$. The same table was used in the Supplement of our publication [139], which is copyrighted by the American Physical Society.

	fractional atomic coordinates			$\boldsymbol{U}_{\mathbf{eq}}$
atom	x	y	z	[Å^2]
O1	0.6960(10)	0.5	0.9204(7)	0.034(3)
O2	0.1619(8)	0	0.3915(5)	0.009(3)
O3	0.9350(6)	0.278(1)	0.8994(5)	0.025(2)
O4	0.4037(7)	0.773(1)	0.4121(5)	0.035(2)
O5	0.8257(8)	0.5	0.7562(8)	0.026(4)
O6	0.3480(8)	0	0.2582(8)	0.034(4)
P1	0.8435(4)	0.5	0.8675(4)	0.012(1)
P2	0.3277(4)	0	0.3671(4)	0.013(1)
Na1	0.8283(6)	0.5	0.0882(5)	0.033(2)
Na2	0.3525(6)	0	0.5927(5)	0.040(2)
Co1	0	0	0	0.0198(8)
Co2	0.5	0.5	0.5	0.0187(9)
Sr1	0.0212(1)	0	0.7498(2)	0.0257(3)

Table A.3.: Atomic coordinates and mean-square atomic displacement parameters obtained from refinement with the space group $P\overline{3}m1$. The synchrotron XRPD data were collected at 1025 K. The cell parameters are $a = 5.338296(8)$ Å and $c = 6.90823(1)$ Å. The same table was used in the Supplement of our publication [139], which is copyrighted by the American Physical Society.

	fractional atomic coordinates			$\boldsymbol{U}_{\mathbf{eq}}$
atom	x	y	z	[Å^2]
O1	0.1798(3)	0.8202(3)	0.3084(4)	0.0356(10)
O2	1/3	2/3	0.0169(9)	0.040(2)
P1	1/3	2/3	0.2349(4)	0.0144(5)
Na1	1/3	2/3	0.6794(5)	0.044(1)
Co1	0	0	0.5	0.0225(6)
Sr1	0	0	0	0.0310(5)

Bibliography

1. Hemme, H. Die Mathematik der Bienenwabe. *Spektrum* **6,** 12 (1994).
2. Zhu, Z., Maksimov, P. A., White, S. R. & Chernyshev, A. L. Topography of Spin Liquids on a Triangular Lattice. *Phys. Rev. Lett.* **120,** 207203 (2018).
3. Zhu, Z. & White, S. R. Spin liquid phase of the $S = \frac{1}{2} J_1 - J_2$ Heisenberg model on the triangular lattice. *Phys. Rev. B* **92,** 041105(R) (2015).
4. Zhong, R., Guo, S., Xu, G., Xu, Z. & Cava, R. J. Strong quantum fluctuations in a quantum spin liquid candidate with a Co-based triangular lattice. *Proc. Natl. Acad. Sci. U.S.A.* **116,** 14505–14510 (2019).
5. Mittemeijer, E. J. *Fundamentals of Materials Science* 103–122. ISBN: 978-3-642-10499-2 (Springer, Berlin, Heidelberg, 2010).
6. Wills, A. Magnetic structures and their determination using group theory. *J. Phys. IV France* **11,** 133–158 (2001).
7. Cracknell, A. P. *Angewandte Gruppentheorie - Einführung und Originaltexte* ISBN: 3528060840 (Friedr. Vieweg + Sohn GmbH Verlag, Braunschweig, 1971).
8. Joshi, A. W. *Elements of Group Theory for Physicists* ISBN: 0 85226 443 7 (Wiley Eastern Limited, 1978).
9. Tsirlin, A. A. *Lecture: Understanding Correlated Materials* University of Augsburg, 2019.
10. Kittel, C. *Einführung in die Festkörperphysik, Kapitel 2* 33–49. ISBN: 3-486-27219-5 (Oldenbourg Verlag, München, Wien, 2022).
11. Sivia, D. S. *Elementary Scattering Theory - For X-ray and Neutron Users* 74. ISBN: 978-0-19-922868-3 (Oxford University Press, 2011).
12. Blundell, S. *Magnetism in Condensed Matter* 47. ISBN: 978 0 19 8505914 4 (Oxford University Press, 2001).
13. Blundell, S. *Magnetism in Condensed Matter* 210. ISBN: 978 0 19 8505914 4 (Oxford University Press, 2001).
14. Blundell, S. *Magnetism in Condensed Matter* 32. ISBN: 978 0 19 8505914 4 (Oxford University Press, 2001).
15. Kotani, M. On the Magnetic Moment of Complex Ions. (I). *J. Phys. Soc. Japan* **4,** 293–297 (1949).
16. Wellm, C. *et al.* Frustration enhanced by Kitaev exchange in a $\tilde{j}_{\text{eff}} = \frac{1}{2}$ triangular antiferromagnet. *Phys. Rev. B* **104,** L100420 (2021).

17. Kézsmárki, I. *Lecture: Symmetry Concepts* University of Augsburg, 2021.
18. Van Vleck, J. H. *The Theory of Electric and Magnetic Susceptibilities* 134 (Clarendon Press, Oxford, 1932).
19. Van Vleck, J. H. Nobel Lecture: Quantum Mechanics the Key to understand Magnetism (1977).
20. Blundell, S. *Magnetism in Condensed Matter* 23–30. ISBN: 978 0 19 8505914 4 (Oxford University Press, 2001).
21. Krug von Nidda, H.-A. *Lecture: Magnetism* University of Augsburg, 2018.
22. Fazekas, P. *Lecture Notes on Electron Correlation and Magnetism* 57–59. ISBN: 978-9814-02-2474-5 (World Scientific Publishing Co. Pte. Ltd, 1999).
23. Schmidt, K. P. & Trebst, S. Topologische Spinflüssigkeiten. *Physik Journal* **14,** 39–44 (2015).
24. Anderson, P. Resonating valence bonds: A new kind of insulator? *Mater. Res. Bull.* **8,** 153–160 (1973).
25. Huse, D. A. & Elser, V. Simple Variational Wave Functions for Two-Dimensional Heisenberg Spin-1/2 Antiferromagnets. *Phys. Rev. Lett.* **60,** 2531–2534 (1988).
26. Capriotti, L., Trumper, A. E. & Sorella, S. Long-Range Néel Order in the Triangular Heisenberg Model. *Phys. Rev. Lett.* **82,** 3899–3902 (1999).
27. Yamamoto, D., Marmorini, G. & Danshita, I. Quantum Phase Diagram of the Triangular-Lattice XXZ Model in a Magnetic Field. *Phys. Rev. Lett.* **112,** 127203 (2014).
28. Maksimov, P. A., Zhu, Z., White, S. R. & Chernyshev, A. L. Anisotropic-Exchange Magnets on a Triangular Lattice: Spin Waves, Accidental Degeneracies, and Dual Spin Liquids. *Phys. Rev. X* **9,** 021017 (2019).
29. Iqbal, Y., Hu, W.-J., Thomale, R., Poilblanc, D. & Becca, F. Spin liquid nature in the Heisenberg $J_1 - J_2$ triangular antiferromagnet. *Phys. Rev. B* **93,** 144411 (2016).
30. Iaconis, J., Liu, C., Halász, G. B. & Balents, L. Spin Liquid versus Spin Orbit Coupling on the Triangular Lattice. *SciPost Phys.* **4,** 003 (2018).
31. Luo, Q., Hu, S., Xi, B., Zhao, J. & Wang, X. Ground-state phase diagram of an anisotropic spin-$\frac{1}{2}$ model on the triangular lattice. *Phys. Rev. B* **95,** 165110 (2017).
32. Zhang, M. *et al.* Projected entangled pair states study of anisotropic-exchange magnets on the triangular lattice. *Phys. Rev. B* **105,** 024411 (2022).
33. Nakatsuji, S., Ikeda, S.-i. & Maeno, Y. Ca_2RuO_4: New Mott Insulators of Layered Ruthenate. *J. Phys. Soc. Jpn* **66,** 1868–1871 (1997).

34. Kim, B. J. *et al.* Novel $J_{\text{eff}} = 1/2$ Mott State Induced by Relativistic Spin-Orbit Coupling in Sr_2IrO_4. *Phys. Rev. Lett.* **101,** 076402 (2008).
35. Singh, Y. & Gegenwart, P. Antiferromagnetic Mott insulating state in single crystals of the honeycomb lattice material Na_2IrO_3. *Phys. Rev. B* **82,** 064412 (2010).
36. Kitaev, A. Anyons in an exactly solved model and beyond. *Ann. Phys.* **321.** January Special comment, 2–111 (2006).
37. Jackeli, G. & Khaliullin, G. Mott Insulators in the Strong Spin-Orbit Coupling Limit: From Heisenberg to a Quantum Compass and Kitaev Models. *Phys. Rev. Lett.* **102,** 017205 (2009).
38. Kim, H.-S., Shankar V., V., Catuneanu, A. & Kee, H.-Y. Kitaev magnetism in honeycomb $RuCl_3$ with intermediate spin-orbit coupling. *Phys. Rev. B* **91,** 241110 (2015).
39. Takagi, H., Takayama, T., Jackeli, G., Khaliullin, G. & Nagler, S. E. Concept and realization of Kitaev quantum spin liquids. *Nat. Rev. Phys.* **1,** 264–280 (2019).
40. Khaliullin, G. Excitonic Magnetism in Van Vleck–type d^4 Mott Insulators. *Phys. Rev. Lett.* **111,** 197201 (2013).
41. Takayama, T., Chaloupka, J., Smerald, A., Khaliullin, G. & Takagi, H. Spin-Orbit-Entangled Electronic Phases in $4d$ and $5d$ Transition-Metal Compounds. *J. Phys. Soc. Jpn* **90,** 062001 (2021).
42. Souliou, S.-M. *et al.* Raman Scattering from Higgs Mode Oscillations in the Two-Dimensional Antiferromagnet Ca_2RuO_4. *Phys. Rev. Lett.* **119,** 067201 (2017).
43. Jain, A. *et al.* Higgs mode and its decay in a two-dimensional antiferromagnet. *Nat. Phys.* **13,** 633–637 (2017).
44. Gretarsson, H. *et al.* Observation of spin-orbit excitations and Hund's multiplets in Ca_2RuO_4. *Phys. Rev. B* **100,** 045123 (2019).
45. Chaloupka, J. & Khaliullin, G. Highly frustrated magnetism in relativistic d^4 Mott insulators: Bosonic analog of the Kitaev honeycomb model. *Phys. Rev. B* **100,** 224413 (2019).
46. Miura, Y., Yasui, Y., Sato, M., Igawa, N. & Kakurai, K. New-Type Phase Transition of Li_2RuO_3 with Honeycomb Structure. *J. Phys. Soc. Jpn* **76,** 033705 (2007).
47. Mogare, K. M., Friese, K., Klein, W. & Jansen, M. Syntheses and Crystal Structures of Two Sodium Ruthenates: Na_2RuO_4 and Na_2RuO_3. *Z. anorg. allg. Chem.* **630,** 547–552 (2004).
48. Mortemard de Boisse, B. *et al.* Intermediate honeycomb ordering to trigger oxygen redox chemistry in layered battery electrode. *Nat. Commun.* **7,** 11397 (2016).

49. Wang, J. C. *et al.* Lattice-tuned magnetism of Ru^{4+} ($4d^4$) ions in single crystals of the layered honeycomb ruthenates Li_2RuO_3 and Na_2RuO_3. *Phys. Rev. B* **90,** 161110 (2014).
50. Gapontsev, V. V. *et al.* Spectral and magnetic properties of Na_2RuO_3. *J. Phys. Condens. Matter* **29,** 405804 (2017).
51. Veiga, L. S. I. *et al.* Correlated electron metal properties of the honeycomb ruthenate Na_2RuO_3. *Phys. Rev. Mater.* **4,** 094202 (2020).
52. Shikano, M. *et al.* Synthesis and Characterization of a Magnetic Semiconductor Na_2RuO_4 Containing One-Dimensional Chains of Ru^{6+}. *Inorg. Chem.* **43,** 5–7 (2004).
53. Dulac, J. F. Synthesis and crystallographic structure of a new ternary compound Li_2RuO_3. *C. R. Acad. Sci. Paris Ser. B* **270,** 223 (1970).
54. Kimber, S. A. J. *et al.* Interlayer tuning of electronic and magnetic properties in honeycomb ordered $Ag_3LiRu_2O_6$. *J. Mater. Chem.* **20,** 8021–8025 (2010).
55. Regan, K., Huang, Q. & Cava, R. Isolated spin 3/2 plaquettes in Na_3RuO_4. *J. Solid State Chem.* **178,** 2104–2108 (2005).
56. Petříček, V., Dušek, M. & Palatinus, L. Crystallographic Computing System JANA2006: General features. *Zeitschrift für Kristallographie - Crystalline Materials* **229,** 345–352 (2014).
57. Toby, B. H. & Von Dreele, R. B. GSAS-II: the genesis of a modern open-source all purpose crystallography software package. *J. Appl. Crystallogr.* **46,** 544–549 (2013).
58. Treacy, M. M. J., Newsam, J. M. & Deem, M. W. A general recursion method for calculating diffracted intensities from crystals containing planar faults. *Proc. R. Soc. Lond.* **A 433,** 499–520 (1991).
59. Bette, S. *et al.* Solution of the heavily stacking faulted crystal structure of the honeycomb iridate $H_3LiIr_2O_6$. *Dalton Trans.* **46,** 15216–15227 (2017).
60. Rodríguez-Carvajal, J. Recent advances in magnetic structure determination by neutron powder diffraction. *Physica B Condens. Matter* **192,** 55–69 (1993).
61. *ILL web, Instruments list* `https://www.ill.eu/users/instruments/instruments-list`. accessed: 2023-03-08.
62. Günther, H. *NMR spectroscopy - Basic principles, concepts, and applications in chemistry* 2nd ed., 11. ISBN: 0-471-95199-4 (John Wiley & Sons Ltd, England, 1995).
63. Brus, J., Abbrent, S., Kobera, L., Urbanova, M. & Cuba, P. in *Annual Reports on NMR Spectroscopy* (ed Webb, G. A.) 79–147 (Academic Press, 2016).
64. Hahn, E. L. Free nuclear induction. *Phys. Today* **6,** 4 (1953).
65. Bert, F. Local probes of magnetism, NMR and μSR: A short introduction. *Collection SFN* **13,** 03001 (2014).

66. Polenova, T., Gupta, R. & Goldbourt, A. Magic Angle Spinning NMR Spectroscopy: A Versatile Technique for Structural and Dynamic Analysis of Solid-Phase Systems. *Anal. Chem.* **87,** 5458–5469 (2015).

67. Hahn, E. L. Nuclear Induction Due to Free Larmor Precession. *Phys. Rev.* **77,** 297–298 (1950).

68. Bloch, F. Nuclear Induction. *Phys. Rev.* **70,** 460–474 (1946).

69. Gretarsson, H. *et al.* IRIXS: a resonant inelastic X-ray scattering instrument dedicated to X-rays in the intermediate energy range. *J. Synchrotron Radiat.* **27,** 538–544 (2020).

70. Biasin, E. *et al.* Revealing the bonding of solvated Ru complexes with valence-to-core resonant inelastic X-ray scattering. *Chem. Sci.* **12,** 3713–3725 (2021).

71. Higley, D. J. *et al.* Stimulated resonant inelastic X-ray scattering in a solid. *Commun. Phys.* **5** (2022).

72. Hans Landolt, R. B. *Zahlenwerte und Funktionen aus Physik, Chemie, Astronomie, Geophysik und Technik / Bd. 4a* 182–190 (Springer, Berlin, Heidelberg, New York, 1967).

73. Alvesalo, T. A., Berglund, P. M., Islander, S. T., Pickett, G. R. & Zimmermann, W. Specific Heat of Liquid He^3/He^4 Mixtures near the Junction of the λ and Phase-Separation Curves. I. *Phys. Rev. A* **4,** 2354–2368 (1971).

74. Edwards, D. O., Brewer, D. F., Seligman, P., Skertic, M. & Yaqub, M. Solubility of He^3 in Liquid He^4 at 0°K. *Phys. Rev. Lett.* **15,** 773–775 (1965).

75. Ifft, E. M., Edwards, D. O., Sarwinski, R. E. & Skertic, M. M. Solubility Curve and Molar Density of Dilute He^3-He^4 Mixtures. *Phys. Rev. Lett.* **19,** 831–833 (1967).

76. Enss, C. & Hunklinger, S. *Low-Temperature Physics, Chapter 5* ISBN: 978-3-540-23164-6 (Springer, Berlin, Heidelberg, New York, 2005).

77. *Magnetic Property Measurement System - MPMS3 User's Manual, Chapter 4-2 14th ed* 2014.

78. Fagaly, R. L. Superconducting quantum interference device instruments and applications. *Rev. Sci. Instrum.* **77,** 101101 (2006).

79. Hunklinger, S. *Festkörperphysik, Kapitel 6* 4th ed., 216. ISBN: 978-3-486-75558-9 (De Gruyter, München, 2014).

80. Enss, C. & Hunklinger, S. *Low-Temperature Physics, Chapter 8* ISBN: 978-3-540-23164-6 (Springer, Berlin, Heidelberg, New York, 2005).

81. Kittel, C. *Einführung in die Festkörperphysik, Kapitel 5* 134 (Oldenbourg Verlag, München, Wien, 2022).

82. Helton, J. S. *et al.* Spin Dynamics of the Spin-1/2 Kagome Lattice Antiferromagnet $ZnCu_3(OH)_6Cl_2$. *Phys. Rev. Lett.* **98,** 107204 (2007).

83. Ran, Y., Hermele, M., Lee, P. A. & Wen, X.-G. Projected-Wave-Function Study of the Spin-1/2 Heisenberg Model on the Kagomé Lattice. *Phys. Rev. Lett.* **98,** 117205 (2007).

84. *Physical Property Measurement System - Heat Capacity Option User's Manual, Chapter 4 26th ed* 2015.

85. Hwang, J. S., Lin, K. J. & Tien, C. Measurement of heat capacity by fitting the whole temperature response of a heat-pulse calorimeter. *Rev. Sci. Instrum.* **68,** 94–101 (1997).

86. *Quantum Design USA, Webinar - Heat Capacity Option* accessed: 2023-03-08. https://www.youtube.com/watch?v=Yi1e3kEgcso.

87. Fang, Z., Nagaosa, N. & Terakura, K. Orbital-dependent phase control in $Ca_{2-x}Sr_xRuO_4$ ($0 <\sim x <\sim 0.5$). *Phys. Rev. B* **69,** 045116 (2004).

88. Liebsch, A. & Ishida, H. Subband Filling and Mott Transition in $Ca_{2-x}Sr_xRuO_4$. *Phys. Rev. Lett.* **98,** 216403 (2007).

89. Gorelov, E. *et al.* Nature of the Mott Transition in Ca_2RuO_4. *Phys. Rev. Lett.* **104,** 226401 (2010).

90. Liu, G.-Q. Spin-orbit coupling induced Mott transition in $Ca_{2-x}Sr_xRuO_4$ ($0 \leq x \leq 0.2$)). *Phys. Rev. B* **84,** 235136 (2011).

91. Fatuzzo, C. G. *et al.* Spin-orbit-induced orbital excitations in Sr_2RuO_4 and Ca_2RuO_4: A resonant inelastic x-ray scattering study. *Phys. Rev. B* **91,** 155104 (2015).

92. Takahashi, H. *et al.* Nonmagnetic $J = 0$ State and Spin-Orbit Excitations in K_2RuCl_6. *Phys. Rev. Lett.* **127,** 227201 (2021).

93. Momma, K. & Izumi, F. VESTA3 for three-dimensional visualization of crystal, volumetric and morphology data. *J. Appl. Crystallogr.* **44,** 1272–1276 (2011).

94. Warren, B. E. X-Ray Diffraction in Random Layer Lattices. *Phys. Rev.* **59,** 693–698 (1941).

95. O'Malley, M. J., Verweij, H. & Woodward, P. M. Structure and properties of ordered Li_2IrO_3 and Li_2PtO_3. *J. Solid State Chem.* **181,** 1803–1809 (2008).

96. Bréger, J. *et al.* High-resolution X-ray diffraction, DIFFaX, NMR and first principles study of disorder in the Li_2MnO_3-$Li[Ni_{1/2}Mn_{1/2}]O_2$ solid solution. *J. Solid State Chem.* **178,** 2575–2585 (2005).

97. Casas-Cabanas, M. *et al.* Microstructural characterisation of battery materials using powder diffraction data: DIFFaX, FAULTS and SH-FullProf approaches. *J. Power Sources* **174,** 414–420 (2007).

98. Cao, H. B. *et al.* Low-temperature crystal and magnetic structure of $\alpha-RuCl_3$. *Phys. Rev. B* **93,** 134423 (2016).

99. Widmann, S. *et al.* Thermodynamic evidence of fractionalized excitations in $\alpha - RuCl_3$. *Phys. Rev. B* **99,** 094415 (2019).

100. Schönemann, R. *et al.* Thermal and magnetoelastic properties of $\alpha - RuCl_3$ in the field-induced low-temperature states. *Phys. Rev. B* **102,** 214432 (2020).

101. Lu, H., Chamorro, J. R., Wan, C. & McQueen, T. M. Universal Single-Ion Physics in Spin-Orbit-Coupled d^5 and d^4 Ions. *Inorg. Chem.* **57,** 14443–14449 (2018).

102. Earnshaw, A., Figgis, B. N., Lewis, J. & Peacock, R. D. 601. The Magnetic Properties of Some d^4-Complexes. *J. Chem. Soc.,* 3132–3138 (1961).

103. Tamai, A. *et al.* High-Resolution Photoemission on Sr_2RuO_4 Reveals Correlation-Enhanced Effective Spin-Orbit Coupling and Dominantly Local Self-Energies. *Phys. Rev. X* **9,** 021048 (2019).

104. Yatsuzuka, H., Haraguchi, Y., Matsuo, A., Kindo, K. & Katori, H. A. Spin-glass transition in the spin-orbit-entangled $J_{eff} = 0$ Mott insulating double-perovskite ruthenate. *Sci. Rep.* **12,** 2429 (2022).

105. Choi, S. K. *et al.* Spin Waves and Revised Crystal Structure of Honeycomb Iridate Na_2IrO_3. *Phys. Rev. Lett.* **108,** 127204 (2012).

106. Chalker, J. T. *Geometrically Frustrated Antiferromagnets: Statistical Mechanics and Dynamics* (eds Lacroix, C., Mendels, P. & Mila, F.) 3–22. ISBN: 978-3-642-10589-0 (Springer, Berlin, Heidelberg, 2011).

107. Haraldsen, J. T. *et al.* Spin-lozenge thermodynamics and magnetic excitations in Na_3RuO_4. *J. Phys. Condens.* **21,** 506003 (2009).

108. Bain, G. A. & Berry, J. F. Diamagnetic Corrections and Pascal's Constants. *J. Chem. Educ.* **85,** 532 (2008).

109. Drillon, M., Darriet, J. & Georges, R. Etude des proprietes thermodynamiques d'un groupement tetranucleaire: Application au compose Na_3RuO_4. *J. Phys. Chem. Solids.* **38,** 411–418 (1977).

110. Roisnel, T. & Rodríquez-Carvajal, J. *WinPLOTR: a windows tool for powder diffraction pattern analysis* in *Materials Science Forum* **378** (2000), 118–123.

111. Rodriguez, E. E. *et al.* Noncollinear spin-density-wave antiferromagnetism in FeAs. *Phys. Rev. B* **83,** 134438 (2011).

112. Papke, E. Origin of incommensurability in the magnetic structure of Na_3RuO_4. *Bachelor thesis,* University of Augsburg, Exprimental Physics VI (2022).

113. Lee, S. *et al.* Temporal and field evolution of spin excitations in the disorder-free triangular antiferromagnet $Na_2BaCo(PO_4)_2$. *Phys. Rev. B* **103,** 024413 (Jan. 2021).

114. Li, N. *et al.* Possible itinerant excitations and quantum spin state transitions in the effective spin-1/2 triangular-lattice antiferromagnet $Na_2BaCo(PO_4)_2$. *Nature Comm.* **11,** 4216 (Aug. 2020).

115. Chan, R. Theoretical Study of Quantum Spin Liquid Candidate $Na_2BaCo(PO_4)_2$. accessed: 2023-03-08. https://cem.osu.edu/files/2022/05/ChanRebeccaPaper.pdf (2021).

116. Huang, Y. Y. *et al.* Thermal conductivity of triangular-lattice antiferromagnet $Na_2BaCo(PO_4)_2$: Absence of itinerant fermionic excitations. https://arxiv.org/abs/2206.08866 (2022).

117. Gao, Y. *et al.* Spin supersolidity in nearly ideal easy-axis triangular quantum antiferromagnet $Na_2BaCo(PO_4)_2$. https://arxiv.org/abs/2202.05242 (2022).

118. Sheng, J. *et al.* Two-dimensional quantum universality in the spin-1/2 triangular-lattice quantum antiferromagnet $Na_2BaCo(PO_4)_2$. *PNAS* **119,** e2211193119 (2022).

119. Griffith, J. S. Octahedral complexes. Part 1.-Magnetic susceptibilities in the first transition series. *Trans. Faraday Soc.* **54,** 1109–1116 (1958).

120. Elstner, N., Singh, R. R. P. & Young, A. P. Finite temperature properties of the spin-1/2 Heisenberg antiferromagnet on the triangular lattice. *Phys. Rev. Lett.* **71,** 1629–1632 (1993).

121. Tamura, M. & Kato, R. Magnetic susceptibility of β'-[Pd(dmit)$_2$] salts (dmit = 1, 3-dithiol-2-thione-4, 5-dithiolate, C_3S_5): evidence for frustration in spin-1/2 Heisenberg antiferromagnets on a triangular lattice. *J. Phys.: Condens. Matter* **14,** L729–L734 (2002).

122. Ranjith, K. M. *et al.* Anisotropic field-induced ordering in the triangular-lattice quantum spin liquid $NaYbSe_2$. *Phys. Rev. B* **100,** 224417 (2019).

123. Johnston, D. C. *et al.* Thermodynamics of spin S=1/2 antiferromagnetic uniform and alternating-exchange Heisenberg chains. *Phys. Rev. B* **61,** 9558–9606 (2000).

124. Gonzalez, M. G., Bernu, B., Pierre, L. & Messio, L. Ground-state and thermodynamic properties of the spin-$\frac{1}{2}$ Heisenberg model on the anisotropic triangular lattice. *SciPost Phys.* **12,** 112 (2022).

125. Li, Y. *et al.* Rare-Earth Triangular Lattice Spin Liquid: A Single-Crystal Study of $YbMgGaO_4$. *Phys. Rev. Lett.* **115,** 167203 (2015).

126. Li, Y. *et al.* Gapless quantum spin liquid ground state in the two-dimensional spin-1/2 triangular antiferromagnet $YbMgGaO_4$. *Sci. Rep.* **5,** 16419 (2015).

127. Shen, Y. *et al.* Evidence for a spinon Fermi surface in a triangular-lattice quantum-spin-liquid candidate. *Nature* **540,** 559–562 (2016).

128. Li, Y. *et al.* Muon Spin Relaxation Evidence for the U(1) Quantum Spin-Liquid Ground State in the Triangular Antiferromagnet $YbMgGaO_4$. *Phys. Rev. Lett.* **117,** 097201 (2016).

129. Xu, Y. *et al.* Absence of Magnetic Thermal Conductivity in the Quantum Spin-Liquid Candidate $YbMgGaO_4$. *Phys. Rev. Lett.* **117,** 267202 (2016).

130. Li, Y. *et al.* Crystalline Electric-Field Randomness in the Triangular Lattice Spin-Liquid $YbMgGaO_4$. *Phys. Rev. Lett.* **118,** 107202 (2017).

131. Dey, S., Andrade, E. C. & Vojta, M. Destruction of long-range order in non-collinear two-dimensional antiferromagnets by random-bond disorder. *Phys. Rev. B* **101,** 020411 (2020).

132. Susuki, T. *et al.* Magnetization Process and Collective Excitations in the $S = 1/2$ Triangular-Lattice Heisenberg Antiferromagnet $Ba_3CoSb_2O_9$. *Phys. Rev. Lett.* **110,** 267201 (2013).

133. Ono, T. *et al.* Magnetization plateau in the frustrated quantum spin system Cs_2CuBr_4. *Phys. Rev. B* **67,** 104431 (2003).

134. Fortune, N. A. *et al.* Cascade of Magnetic-Field-Induced Quantum Phase Transitions in a Spin-$\frac{1}{2}$ Triangular-Lattice Antiferromagnet. *Phys. Rev. Lett.* **102,** 257201 (2009).

135. Alicea, J., Chubukov, A. V. & Starykh, O. A. Quantum Stabilization of the 1/3-Magnetization Plateau in Cs_2CuBr_4. *Phys. Rev. Lett.* **102,** 137201 (2009).

136. Mao, Z. *et al.* Strain-induced magnetic moment enhancement in frustrated antiferromagnet Cs_2CuBr_4. *J. Phys. Condens. Matter* **32,** 365801 (2020).

137. Rawl, R. *et al.* $Ba_8CoNb_6O_{24}$: A spin-$\frac{1}{2}$ triangular-lattice Heisenberg antiferromagnet in the two-dimensional limit. *Phys. Rev. B* **95,** 060412(R) (Feb. 2017).

138. Cui, Y. *et al.* Mermin-Wagner physics, (H, T) phase diagram, and candidate quantum spin-liquid phase in the spin-$\frac{1}{2}$ triangular-lattice antiferromagnet $Ba_8CoNb_6O_{24}$. *Phys. Rev. Mater.* **2,** 044403 (2018).

139. Bader, V. P., Langmann, J., Gegenwart, P. & Tsirlin, A. A. Deformation of the triangular spin-$\frac{1}{2}$ lattice in $Na_2SrCo(PO_4)_2$. *Phys. Rev. B* **106,** 054415 (2022).

140. Zhang, C. *et al.* Doping-induced structural transformation in the spin-1/2 triangular-lattice antiferromagnet $Na_2Ba_{1-x}Sr_xCo(PO_4)_2$. *J. Alloys Compd.* **905,** 164147 (2022).

141. Sanjeewa, L. D. *et al.* Investigation of a Structural Phase Transition and Magnetic Structure of $Na_2BaFe(VO_4)_2$: A Triangular Magnetic Lattice with a Ferromagnetic Ground State. *Inorg. Chem.* **56,** 14842–14849 (2017).

142. Sanjeewa, L. D., Garlea, V. O., McGuire, M. A., McMillen, C. D. & Kolis, J. W. Magnetic Ground State Crossover in a Series of Glaserite Systems with Triangular Magnetic Lattices. *Inorg. Chem.* **58,** 2813–2821 (2019).

143. Reuß, A. *et al.* Screw-Type Motion and Its Impact on Cooperativity in $BaNa_2Fe[VO_4]_2$. *Inorg. Chem.* **57,** 6300–6308 (2018).

144. Sanjeewa, L. D., McMillen, C. D., Willett, D., Chumanov, G. & Kolis, J. W. Hydrothermal synthesis of single crystals of transition metal vanadates in the glaserite phase. *J. Solid State Chem.* **236,** 61–68 (2016).

145. Tapp, J. *et al.* From magnetic order to spin-liquid ground states on the $S = \frac{3}{2}$ triangular lattice. *Phys. Rev. B* **96,** 064404 (2017).

146. Bader, V. P., Fitch, A. & Tsirlin, A. A. High-resolution x-ray diffraction on the triangular antiferromagnet $Na_2SrCo(PO_4)_2$. *European Synchrotron Radiation Facility (ESRF),* https://doi.esrf.fr/10.15151/ESRF-DC-885525061 (2022).

147. Bader, V. P., Grendal, O. G. & Tsirlin, A. A. High-resolution x-ray diffraction on the triangular antiferromagnet $Na_2SrCo(PO_4)_2$. *European Synchrotron Radiation Facility (ESRF),* https://doi.esrf.fr/10.15151/ESRF-DC-885525164 (2022).

148. Boukhris, A., Hidouri, M., Glorieux, B. & Amara, M. B. Correlation between structure and photoluminescence of the europium doped glaserite-type phosphate $Na_2SrMg(PO_4)_2$. *Mater. Chem. Phys.* **137,** 26–33 (2012).

149. Gitgeatpong, G. *et al.* Magnetic structure and Dzyaloshinskii-Moriya interaction in the $S = \frac{1}{2}$ helical-honeycomb antiferromagnet α-$Cu_2V_2O_7$. *Phys. Rev. B* **92,** 024423 (2015).

150. Gitgeatpong, G. *et al.* High-field magnetization and magnetic phase diagram of α-$Cu_2V_2O_7$. *Phys. Rev. B* **95,** 245119 (2017).

151. Yamamoto, D., Marmorini, G., Tabata, M., Sakakura, K. & Danshita, I. Magnetism driven by the interplay of fluctuations and frustration in the easy-axis triangular XXZ model with transverse fields. *Phys. Rev. B* **100,** 140410(R) (2019).

152. Brown, I. D. & Altermatt, D. Bond-valence parameters obtained from a systematic analysis of the Inorganic Crystal Structure Database. *Acta Crystallogr. Sect. B* **41,** 244–247 (1985).

153. Kamiya, Y. *et al.* The nature of spin excitations in the one-third magnetization plateau phase of $Ba_3CoSb_2O_9$. *Nature Comm.* **9,** 2666 (2018).

154. Ono, T. *et al.* Field-Induced Phase Transitions Driven by Quantum Fluctuation in S = 1/2 Anisotropic Triangular Antiferromagnet Cs_2CuBr_4. *Progr. Theor. Phys.* **159,** 217–221 (2005).

155. Zvyagin, S. A. *et al.* Direct Determination of Exchange Parameters in Cs_2CuBr_4 and Cs_2CuCl_4: High-Field Electron-Spin-Resonance Studies. *Phys. Rev. Lett.* **112,** 077206 (2014).

156. Coldea, R., Tennant, D. A., Tsvelik, A. M. & Tylczynski, Z. Experimental Realization of a 2D Fractional Quantum Spin Liquid. *Phys. Rev. Lett.* **86,** 1335–1338 (2001).

157. Abragam, A. & Bleaney, B. *Electron Paramagnetic Resonance of Transition Ions* ISBN: 978-0-19-965152-8 (Oxford University Press, 1970).